Dissertation zur Erlangung des Doktorgrades
der Fakultät für Chemie und Pharmazie
der Ludwig-Maximilians-Universität München

Characterization of Two-Pore Channel 2 in Neovascular Age-Related Macular Degeneration

Yanfen Li
aus
Jiaozuo, Henan, China

2021

Erklärung

Diese Dissertation wurde im Sinne von § 7 der Promotionsordnung vom 28.November 2011 von Herrn Prof. Dr. Stylianos Michalakis betreut.

Eidesstattliche Versicherung

Diese Dissertation wurde eigenständig und ohne unerlaubte Hilfe erarbeitet.

München, den 06.05.2021 _____

(Yanfen Li)

Dissertation eingereicht am: 06.05.2021

1. Gutachter: Prof. Dr. Stylianos Michalakis

2. Gutachter: Prof. Dr. Martin Biel

Mündliche Prüfung am: 18.06.2021

Table of Contents

1 Introduction [1]

1.1 Age-Related Macular Degeneration

Sight is probably the most valued sense among the general population and vision impairment severely impacts on the daily life of affected patients. Daylight vision is mainly conferred by a 6-mm part of the central retina of the human eye, referred to as macula [2], which contains a large amount of densely packed cone photoreceptor cells. Damage of the macula may result in the loss of high acuity and color vision.

Age-related macular degeneration (AMD) is the progressive damage of the macula and the major cause of blindness among people over 55 years of age, particularly in western countries[3, 4]. The population older than 65 years is the fast-growing proportion in society and, thus, the estimated prevalence of the AMD is expected to be close to 300 million worldwide by 2040, posing a significant global economic and clinical burden [4]. The current therapeutic approaches to treat AMD are limited and fail to preserve vision in patients on the long run. For this reason it is indispensable to decipher the underlying pathological mechanism of AMD and find safe and effective treatment options for this disease.

1.1.1 Normal Retinal structure

The vertebrate retina is a specialized sensory tissue lining the back of our eyes. It consists of different neuronal and non-neuronal cell types, which are involved in the detection, initial processing and subsequent transmission of light-encoded information to the brain via a complex neural circuitry. In the retina there are five major types of neurons morphologically and functionally arranged in alternating layers: photoreceptors, bipolar cells, horizontal cells, amacrine cells, and ganglion cells (Figure 1). The cell bodies of neurons are distributed in the outer nuclear, inner nuclear, and ganglion cell layers, while the elongated cell processes and synapses are located in the inner and outer plexiform layers. When light hits the retina from the vitreal side, it needs to pass through the semi-transparent tissue to reach the innermost layer where the photoreceptor outer segments reside. Light-sensitive photoreceptors, subdivided into rods and cones, can absorb light and change membrane potential during phototransduction, which causes changes in the release of neurotransmitter glutamate. Subsequently, bipolar cells that are in contact with photoreceptors in the outer plexiform layer, take up glutamate and further propagate the signal to the downstream ganglion cells, whose axons form the optic nerve that relays the signal to thalamic nuclei. The photoreceptor to bipolar to ganglion cell pathway is the main signal transmission path to the brain. Horizontal and amacrine cells are spread laterally in the apical or basal inner nuclear layer, respectively, and are responsible for excitatory and inhibitory finetuning. The former send feedback signals

between photoreceptors and regulate the synaptic transmission between photoreceptors and bipolar cells. The latter have distinct functions due to their structural diversity. Amacrine cells not only control the output from bipolar cells to ganglion cells but also modulate ganglion cell responses either at the postsynaptic terminals of bipolar cells or at the presynaptic dendrites of ganglion cells. Following the multi-layered processing of the retinal signals, the ganglion cells are the last output cells, which transmit visual stimuli to the brain in the form of action potentials. The optic nerve formed by axons transmits retinal information to the visual target areas in the brain.

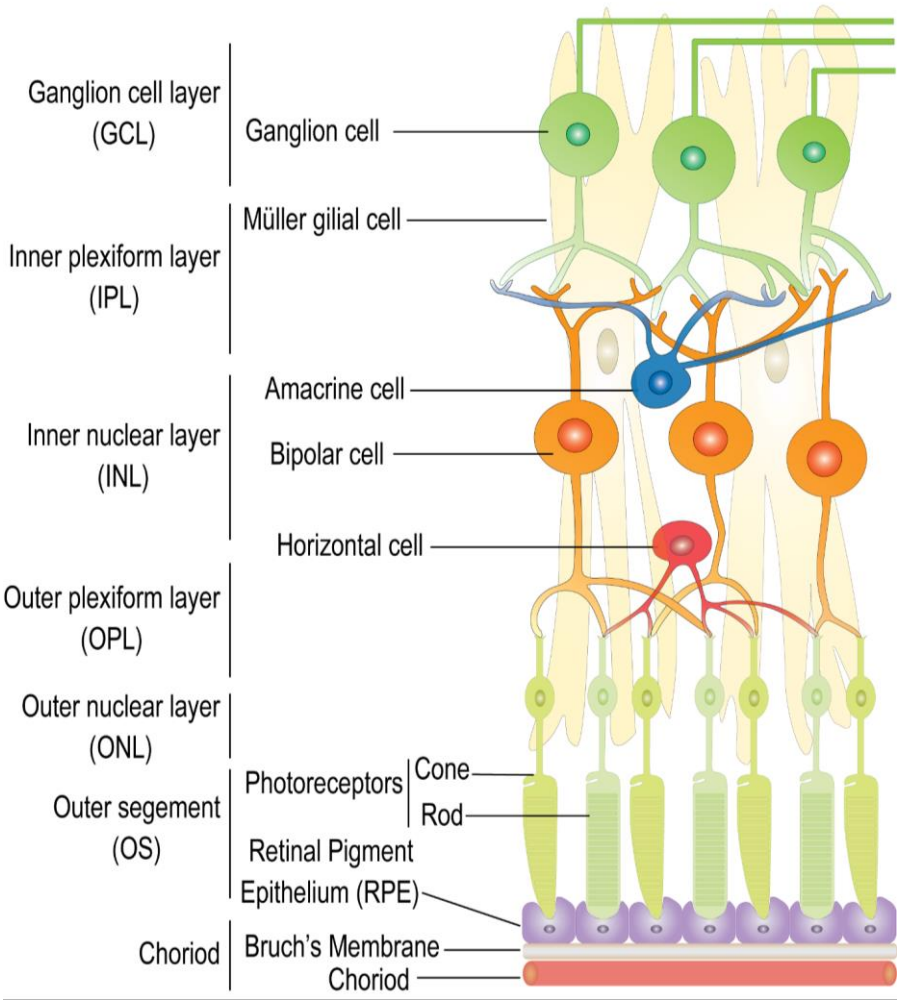

Figure 1 Schematic drawing of the cellular components of the retina.

Another important non-neuronal cell type in the retina is Müller glia which are radially oriented and almost span across the entire retina. Müller glia cells maintain the structural and functional stability of retinal cells and regulate the extracellular environment. Specifically, these cells remove cell debris, regulate neurotransmitters, regulate ion homeostasis and mechanically supportthe neural retina. Apart from the Müller glia, retinal pigment epithelium (RPE) is another major non-neuronal cell type in the retina. RPE is a well-organized monolayer of hexagonal

cells underneath the photoreceptors and atop a specialized basement membrane, referred to as Bruch's membrane. RPE forms the outer blood-retinal barrier which isolates the inner retina from the circulating blood. This renders the posterior eye an immune-privileged space. Due to its specific location, RPE plays a role in multiple functions, such as supplying nutrients to photoreceptors, regulating ion homeostasis, and transporting metabolic products. RPE cells also phagocytose cell debris and the apical tips of photoreceptor outer segments which regenerate throughout the cell's lifetime. The vascular layer, also known as the choroid, is adjacent to Bruch's membrane. It supplies oxygen and nourishment to the outer retina for maintaining the high oxygen consumption of photoreceptors. Collectively, these components of the retina work in parallel, and in combination to establish the anatomical structures and sophisticated functions of the eye.

1.1.2 Pathophysiology of AMD

The retinal structures associated with AMD development are photoreceptors, RPE, Bruch's membrane, and choroid. Sufficient metabolic exchanges take place in these interdependent structures in normal eyes. With age, dysfunctional and atrophied RPE results in insufficient phagocytosis and degradation of damaged cellular components. Consequently, the undegraded materials called drusen deposit in Bruch's membrane, which is the hallmark of dry AMD (also referred to as nonexudative AMD) (Figure 2). Although the early stage of dry AMD is asymptomatic, it may further develop to the advanced form of dry AMD (also known as geographic atrophy). In geographic atrophy (GA), there is progressive degeneration of RPE and loss of photoreceptors. This irreversible degeneration can subsequently lead to visual impairment and deteriorate into the worst late-stage. The late-stage form of AMD, also known as the wet form, is characterized by abnormal blood vessel growth (choroidal neovascularization) originated from invading choroid vessels leaking into the outer retina area through the ruptured Bruch's membrane. Furthermore, resident microglia and choroidal macrophages accumulate in the subretinal space, which exacerbates photoreceptor degeneration as well as neovascularization (Figure 2). These dysregulated immune responses and severe impairment of retinal structure leads to precipitous visual loss in patients affected by wet AMD.

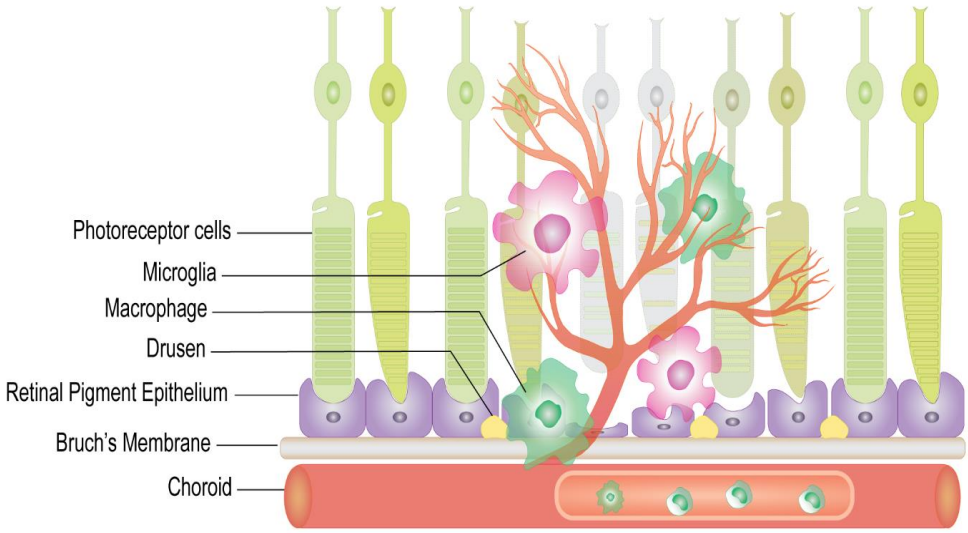

Figure 2 Diagram illustrating the AMD pathogenesis.

1.1.3 Risk Factors Associated with AMD

Considerable epidemiological investigations have pointed out various factors related to the development of AMD. Apart from advanced age, which is the most important risk factor for AMD [5, 6], smoking is also highly associated with the prevalence of AMD [7, 8]. Cigarette smoking, regarded as an inducer of oxidative stress, is implicated in reducing the level of serum antioxidants. This increase in oxidative stress has severe consequences for both the retina and RPE due to their high metabolic demands and massive consumption of oxygen [9]. In addition, some epidemiological research has also found an association between AMD and other comorbidities, including cardiovascular disease [10, 11], diabetes [12, 13], hypertension [14-16], chronic kidney disease [17, 18], and hyperthyroidism [19, 20]. Other environmental risk factors, such as alcohol consumption [21], light exposure [22-24], and diet [25], also have a potential effect on the development of AMD. Beyond the environmental factors, multiple genetic variants also show significant association with AMD [26]: (*1*) genes involved in oxidative stress, e.g., mitochondrial superoxide dismutase 2 (SOD2) [27], mitochondrial MTND2 [28]; (*2*) genes associated with lipid metabolism, e.g., lipoprotein lipase precursor (LPL) [29], apolipoprotein E (APOE) [30] and hepatic lipase (LIPC) [29]; (*3*) complement genes [31-33]; (*4*) gene encoding a serine protease, known as high-temperature requirement factor A 1 (HTRA1) [34]. Together, AMD is a multifactorial disorder. A better understanding of its pathological mechanism and potential interactions between environment and genetic factor will help to develop novel effective treatments.

1.1.4 Inflammation in AMD

Despite the multifaceted etiology of AMD, various lines of evidence highlight that dysregulated immune response plays a key role in AMD pathogenesis. The main role of the immune system is to identify and eliminate exogenous and endogenous insults, such as infection, foreign antigens, and tissue damage. This can evoke a robust inflammatory response. Short-term inflammation is highly beneficial, as it initiates tissue recovery and ensures the integrity of tissue structure and functionalities. However, long-term inflammation can be harmful. Sustained low-level inflammation is associated with the development of multiple chronic diseases, such as cancer, diabetes, and autoimmune diseases.

Immune privilege

The eye has been referred to as a site of immune privilege. This property is crucial for tissues with poor renewal and regenerative capability, such as the brain and retina, to avoid exposure to external and internal insults. The immunosuppressive capacity is achieved by various mechanisms, including the blood-retinal barrier, endogenous immunosuppressive factors, and deficient intraocular lymphatics [35, 36]. The blood-retinal barrier is composed of two key components: retinal vascular endothelial cells, which are joined by tight junctions, and the retinal pigment epithelium. The barriers serve to segregate the retina from foreign pathogens, minimize contact with the systemic immune system and avoid inflammatory disturbance. When barriers are disrupted by pathogens, the retina adopts a strategy to suppress immune response by induction of retinal immunologic tolerances to antigens and repression of immune cell activation. Moreover, retinal cells, like RPE cells, can express and secrete a range of immunomodulatory proteins that consequently modulate the intraocular innate and adaptive inflammatory activity [37]. Nevertheless, this property may result in the inadequate development of self-tolerance to retinal antigens, augment the susceptibility of the retina to autoimmune damage [38], and even trigger autoimmune retinopathies [39].

Retinal microglia and macrophages

Similar to macrophages in tissue and microglia in the central nervous system, retinal microglia are resident immune cells in the retina that respond to pathogenic insults and maintain homeostasis. Retinal microglia are involved in the clearance of dying neurons [40] and the regulation of synaptogenesis during retinal development [41]. This further contributes to the maintenance of synaptic structure and functional homeostasis in the adult retina. In healthy retina, microglia typically reside in the inner part of the retina, with their ramified processes concentrated in the inner plexiform layer (IPL) and the outer plexiform layer (OPL) [42, 43]. When responding to inflammatory stimuli, retinal microglia react rapidly and enter an active

state by transforming from a ramified morphology to an ameboid form and migrate to the outer retina and subretinal space. During aging, the regular distribution of retinal microglia is disrupted and an increased microglia accumulation can be found in the subretinal area. Moreover, microglia undergo morphological and functional changes with aging, including the reduction of ramifications and declined dynamic movement [44]. These alterations are also associated with the pathogenesis of AMD. Microglia with mild activation are found in the outer retina and subretinal space in eyes with AMD and appear to deteriorate choroidal neovascularization [45, 46].

Macrophages, another major subset of retinal immune cells, normally reside within the choroid. However, they can invade the subretinal space when the blood-retinal barrier is compromised. Increasing evidence indicates the presence of perivascular macrophages in areas of drusen and choroidal neovascular lesions in AMD eyes [47, 48]. Microglia, together with invading macrophages, are the major source of pro-angiogenic factors such as vascular endothelial growth factor (VEGFA) [49], indicating that these immune cells are involved in the development of AMD. However, some studies suggest a protective capacity of microglia and macrophages in some animal models, such as chemokine CCL2 deficient mice [50-52]. Therefore, the role of microglia and macrophages in AMD progression is clearly multifaceted and seems to depend on a variety of retina-intrinsic and extrinsic factors.

Macrophages and microglia are heterogeneous and exhibit high phenotypic plasticity, which may explain why these immune cells can play dual roles in either preventing or promoting AMD pathogenesis. Based on their polarization status, macrophages can be subdivided into classically activated macrophages (M1 macrophages) and alternatively activated macrophages (M2 macrophages) [53, 54] (Figure 3). M1 macrophages, driven by helper T cell type 1 (Th1), are activated by microbial products or cytokines including bacterial lipopolysaccharides (LPS) or interferon-γ (IFN-γ) in response to infection. It is reported that M1 macrophages have a general proinflammatory effect and secrete numerous chemokines such as Interleukin-1 (IL-1), IL-6, reactive nitrogen, tumor necrosis factor-α (TNF-α), and oxygen derivatives. In contrast, M2 macrophages, induced by type 2 helper T cells (Th2), are considered to exert anti-inflammatory and pro-angiogenic effects in tissue repair and neovascularization. When stimulated by IL-4 or IL-13 [55], M2 macrophages can generate an array of (M2) cytokines including resistin-like-α (Fizz1), CD206, chitinase-like 3 (Ym1), IL-10, and Arginase1 (Arg1) [53].

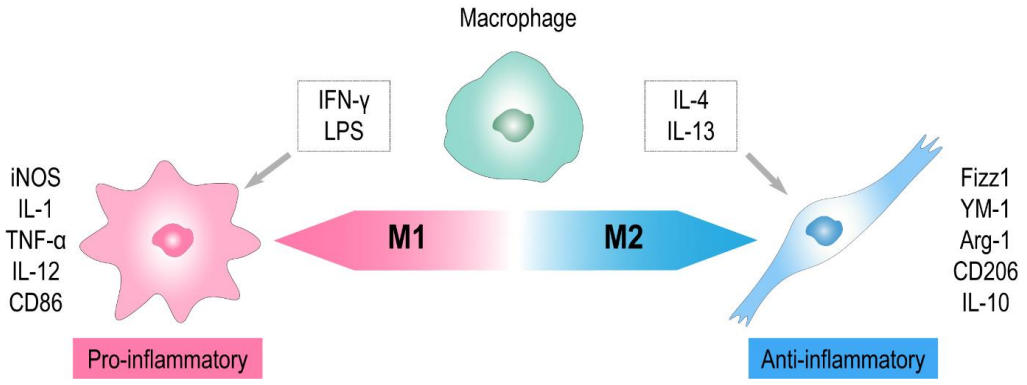

Figure 3 M1 and M2 polarized macrophages and their major cytokines.

Proinflammatory M1 macrophages are activated by interferon-γ and LPS, whereas anti-inflammatory M2 macrophages are stimulated with IL-4 and IL-13. IFN-γ: interferon- γ, LPS: lipopolysaccharide, IL: interleukin, iNOS: inducible nitric oxide synthase, TNF-α: tumor necrosis factor-α, CD: cluster of differentiation, Fizz1: found in inflammatory zone, YM1: chitinase-like 3, Arg-1: Arginase 1.

It has been reported that both M1 and M2 macrophages are present in the aged human retina [56]. M2 macrophages were shown to accumulate in wet AMD, whereas M1 macrophages have greater activity in dry AMD [56]. In the well-established preclinical laser-induced choroidal neovascularization (CNV) model, a dynamic activation pattern of M1 and M2 macrophages can be observed after laser injury: an early shift towards M1 is followed by a delayed-but-sustained shift toward M2 [57]. This activation pattern is in line with the assumption that M1 macrophages are associated with the early stage of AMD to respond to inflammation, whereas M2 macrophages are involved in the middle and advanced stages to promote angiogenesis [57]. In addition, it has been demonstrated that M2 macrophages injected into mouse eyes exacerbated the CNV growth, whereas M1 macrophages repressed it [58]. However, the temporal transition between M1 and M2 states of macrophages, as well as their function in AMD pathophysiology, remain to be elucidated.

Complement system

In addition to microglia and macrophages, a substantial amount of evidence points to a significant contribution of the complement regulatory system to the onset and progression of AMD. In 2005, genome-wide association studies (GWAS) demonstrated that some common variants in genes coding for complement components are significantly associated with AMD development [59]. The Y402H (Tyr402His) variant of the complement factor H (CFH) has been identified to account for the heritability of AMD [60]. CFH is the best-known regulator to inhibit the alternative complement cascade, whereas CFH polymorphism H402 suppresses its inhibitory function by reducing its binding affinity to massive constituents of the injured retina [61, 62]. Therefore, these functional alterations may trigger a greater degree of complement

activation and inflammatory responses following retinal injury. Subsequent studies have also revealed that other complement-related genes are likely to increase AMD susceptibility, including genes for complement component 3 (C3), complement component 2 (C2), and complement factor I (CFI) [31-33].

The complement system is an innate component of the immune system that is responsible for opsonizing pathogens, removing foreign particles and apoptotic cells, recruiting and activating immune cells, and modulating antibody production [63-65]. Current studies suggest that the complement system can be activated through three distinct pathways: classical, mannose-binding lectin (MBL), and alternative pathway (Figure 4). Each pathway involves different molecules for initiating the cascade but converges to a common terminal pathway that generates a pore-forming complex in the pathogen's membrane, the membrane attack complex (MAC). Typically, the classical pathway is initiated by the binding of circulating C1q either directly to the pathogen surface, or onto the antibody-antigen complex [66]. This will then trigger the cleavage of C4 into functional active forms, C4a and C4b. C4b, in turn, cleaves C2 and forms the C4bC2b complex which is the classical pathway of C3 convertase. In the lectin pathway, MBL binds to carbohydrate motifs (including mannose) on the surface of pathogens that activates the MBL-associated serine proteases (MASPs) [67], cleaving C2 and C4, ultimately generating the C3 convertase. Distinct from the classical and lection pathway, the alternative pathway is generally activated by the spontaneous hydrolysis of C3 to the C3(H_2O). The C3(H_2O) can recruit factor B and D, facilitating the further C3 cleavage and the formation of C3 convertase. All three complement activation cascades converge in the formation of the convertase. The C3 convertase is capable of cleaving C3 to produce a large amount of C3a and C3b, which is the key amplification step of the cascade. C3a molecules represent the mediator of inflammation, while C3b which acts as opsonins, is the main effector of the complement system. They can covalently attach to the pathogen surface and destruct it by phagocytes. C3b also associates with C3 convertase to generate a C5 convertase that further cleaves C5 to C5a (an anaphylatoxin) and C5b. The C5b binds to C6 and subsequently promotes the assembly of C7, C8, and up to 16 molecules of C9 to form a C5b-9 membrane attack complex (MAC) [68]. Finally, MAC creates pores in the cell membranes of pathogens that can lyse the targeted cells. In addition to the complement components, a system of soluble regulatory proteins, such as decay acceleration factor (DAF, CD55) [69], CD59 [70] and CFH [71], can also modulate the activation of the complement system, either by spontaneously activating complement components or by preventing the binding of activated complement components to target cells.

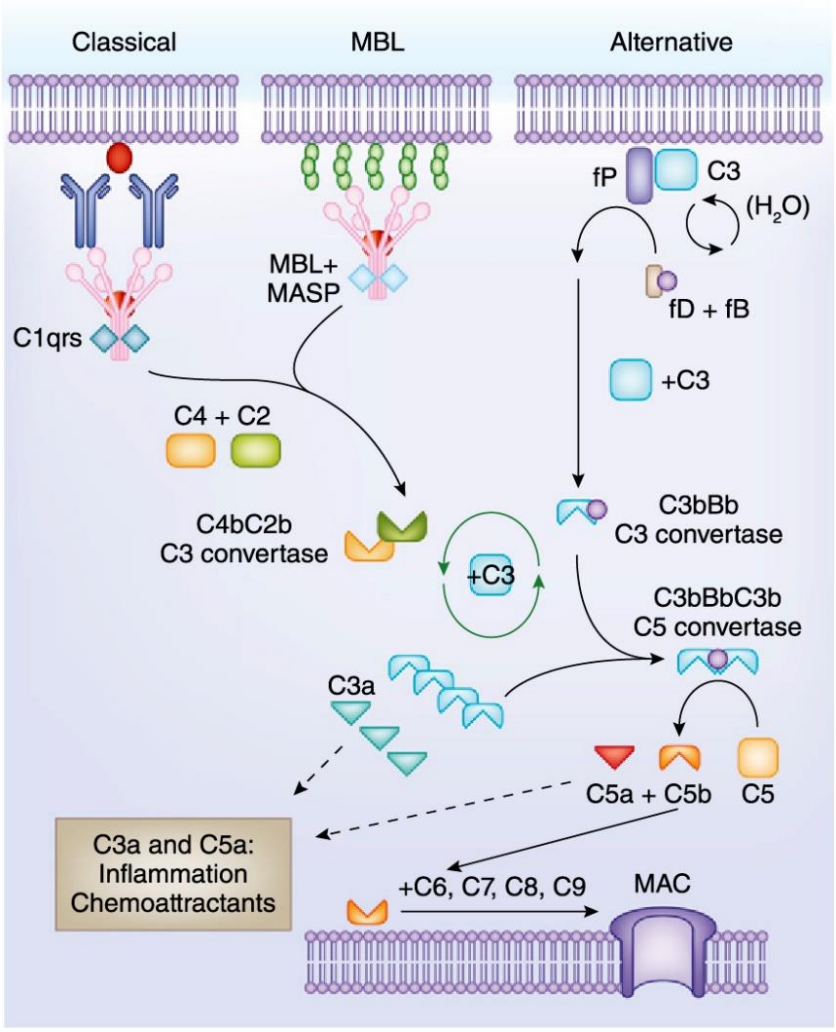

Figure 4 Overview of the complement cascade [72].

The complement system can be activated through three pathways: classical, mannose-binding lectin (MBL), and alternative pathway. All three complement activation cascades converge in the formation of the C3 convertase which cleaves C3 to C3a and C3b. C3b associates with C3 convertase to generate a C5 convertase that cleaves C5 to C5a and C5b. The C5b binds to C6 and subsequently promoting the assembly of C7, C8, and up to 16 molecules of C9 to form C5b-9 membrane attack complex (MAC). The MAC creates a pore in the cell membranes of pathogens that can lyse the targeted cells.

The complement system is a major immune effector in the retina that responds to ocular microenvironmental stimulations. Under normal physiological conditions, there are relatively low amounts of complement molecules and a high amount of complement regulators expressed by retinal cells, which modulate the activation of the complement system [73]. An upregulation of complement proteins is detected in aged eyes [74], suggesting an enhanced complement activation upon inflammatory insults. Emerging evidence has identified that complement activators C3 and C5, the membrane attack complex C5b-9 and complement regulatory proteins CFH are molecular constituents of drusen in AMD patients [62]. Moreover, it has been reported that selective inhibition of C3, C5a, or MAC formation could effectively

reduce choroidal neovascularization in the laser-induced CNV mouse model [75, 76], elucidating the essential role of complement activation in AMD development. Further investigation would be necessary to decipher how complement system influences or even regulates AMD progression.

1.1.5 Therapeutic interventions for AMD

Although multiple pathogenic factors are involved in AMD and their roles in the progression of the disease remain elusive, the increasing knowledge of the molecular mechanisms and pathophysiology of wet AMD has resulted in the development of some therapeutic strategies to treat key symptoms. So far the most effective and broadly used treatment for wet AMD is based on the inhibition of the angiogenic protein VEGFA. VEGFA can trigger neovascularization and increase vascular permeability. Numerous evidence implicates an increased VEGFA expression in the pathophysiology of AMD and it is well established that VEGFA drives the observed CNV formation [77, 78]. Current anti-VEGFA medications for intraocular administration are humanized monoclonal antibodies: Ranibizumab (Lucentis Genentech, Inc.) and Bevacizumab (Avastin®, Genentech, Inc.), which can bind all active forms of VEGFA to prevent its angiogenic activity. Another anti-VEGFA agent is Aflibercept (Eylea®, Regeneron Pharmaceuticals, Inc.), which acts as a soluble VEGFA decoy to block the effect of VEGFA on blood vessel growth. However, all VEGFA-targeted therapies are only symptomatic treatments, which can only delay the progression of vision loss. Moreover, a portion of patients does not respond to anti-VEGFA treatment. Importantly, patients need repeated intravitreal administration of the drugs that are not only costly but also results in side effects such as cataract, retinal detachment, and endophthalmitis. Therefore, a number of other approaches have been attempted, including radiation, surgery, and other pharmacological agents. Treatment combinations, novel customized or gene and cell therapies are currently explored, aiming to offer more effective interventions [79].

In addition to the approved VEGFA-targeted treatment, the genomic findings in AMD patients may facilitate the development of genetic-based therapies to treat the disease. Currently, several clinical trials using complement cascade inhibitors are underway for the treatment of AMD [80]. With a better understanding of genetic pathways and environmental contributions, it should be possible to provide improved therapeutic solutions for AMD patients in the future.

1.2 Interleukin-1β

1.2.1 Mechanisms of IL-1β production and processing

A collection of evidence supports the role of inflammatory cytokines produced by monocytes or macrophages in the pathobiology of AMD [81]. Interleukin-1β (IL-1β), a member of the Interleukin-1 (IL-1) family, is a multifunctional proinflammatory cytokine that participates in

acute and chronic inflammatory diseases. IL-1β is mainly expressed by immune cells, such as neutrophils, monocytes, macrophages, or dendritic cells [82], among which infiltrating macrophages and resident microglia are of relevance for retinal pathologies. Cells sense exogenous and endogenous pathogen- and damage-associated molecular patterns (PAMPs and DAMPs, respectively) via pathogen recognition receptors (PRRs) expressed on the cell membrane, such as Toll-like receptors (TLR) and NOD-like receptors (NLRs). When activated by their ligands, these receptors promote the nuclear translocation of transcriptional factors such as transcript factor nuclear factor (NF)-κB and induce subsequent production of inflammasome components and proinflammatory cytokines, including the pro-forms of IL-1β. IL-1β is synthesized as an inactive 33-kDa precursor protein (pro- IL-1β) and is cleaved into its active 17-kDa form by caspase-1 in the IL-1 signaling pathway [83, 84].

This conversion results from the activation of caspase-1 which is mediated by inflammasome. Inflammasomes are multimeric cytoplasmic complexes, classically consisting of a nucleotide-binding domain leucine-rich repeat (NLR) protein, an adaptor protein apoptosis-associated speck-like protein containing a CARD (ASC) domain, and an effector caspase-1 [85]. Among them, the best-characterized inflammasome is the NLRP3 inflammasome. NLRP3 can recognize a wide range of stimuli, including DAMPS, sterile activators, potassium influx, and the terminal complement component (MAC). Upon stimulation, pro-caspase-1 is recruited and binds to the complex through the ASC domain. Then the oligomerization and assembly of inflammasome complexes induce the activation of caspase-1, which in turn results in the cleavage of pro- IL-1β into biological active IL-1β form and subsequent release into extracellular space.

1.2.2 Mechanisms of IL-1β secretion

Unlike most cytokines, IL-1β lacks the N-terminal secretory signal sequence and thus does not follow the classical endoplasmic reticulum (ER)-Golgi secretory pathway. The precise mechanism of IL-1β release remains to be elucidated. In the last decades, several unconventional secretory models of IL-1β have been proposed, as more is understood about inflammasome cell biology (Figure 5). A secretory lysosome-dependent pathway for IL-1β secretion was described based on evidence that pro-IL-1β and caspase-1 are present in endolysosomal vesicles in LPS-activated human monocytes [86]. Moreover, it has been suggested that the secretion of IL-1β from monocytes was concomitant with the secretion of cathepsin D, a hydrolase in endolysosomal vesicles [87]. In this model, the modified secretory lysosomes are defined as carriers that drive IL-1β release via exocytosis. This process requires a trigger signal, like exogenous ATP, which acts on purinergic $P2X_7$ receptors and induces the efflux of K^+ from the cytosol and the subsequent Ca^{2+} influx [87]. Next, a portion of pro- IL-1β and caspase-1 translocates from the cytosol into secretory lysosomes, followed

by the cleavage and processing of IL-1β during lysosome trafficking. Consequently, lysosomes fuse with the plasma membrane, after which mature IL-1β is released into extracellular space.

Apart from the secretory lysosome pathway, some studies suggest that IL-1β could also be released from the shedding of plasma membrane microvesicles. MacKenzie *et al.* found bioactive IL-1β in isolated microvesicles from human monocyte THP-1 cells in response to $P2X_7$ receptor activation [88]. It was hypothesized that microvesicles were rapidly shed from the cell surface, resulting in the release of IL-1β [88]. Microvesicle shedding has also been suggested as an IL-1β secretory pathway in other cell types, such as human dendritic cells [89] and murine microglia [90].

Furthermore, another model of IL-1β release was explored by Qu *et al.* in 2007 [91]. They compared the contribution of distinct nonclassical secretion pathways in primary murine bone marrow-derived macrophages (BMDM) and proposed a novel model of IL-1β release which involved multivesicular bodies (MVBs) and exosomes. Following the stimulation of $P2X_7$ receptor, MVBs were formed by budding of the late endosome membrane. They contained exosomes which carried IL-1β, histocompatibility complex (MHC) class I and II molecules, and lysosomal marker proteins in immune cells [92]. The release of IL-1β-containing exosomes into the extracellular space depends on the transport of MVBs towards the plasma membrane and fusion with the membrane.

In addition to vesicle-mediated IL-1β secretory pathways, different studies also revealed that IL-1β could be exported in a non-vesicular pathway by passing directly across the plasma membrane via specialized membrane transporters [93]. Recently, evidence from autophagy-related research suggested a role of autophagy in IL-1β secretion [94]. Although different IL-1β secretory pathways, have been identified, their manifestation in different contexts and how each pathway is governed remains unanswered.

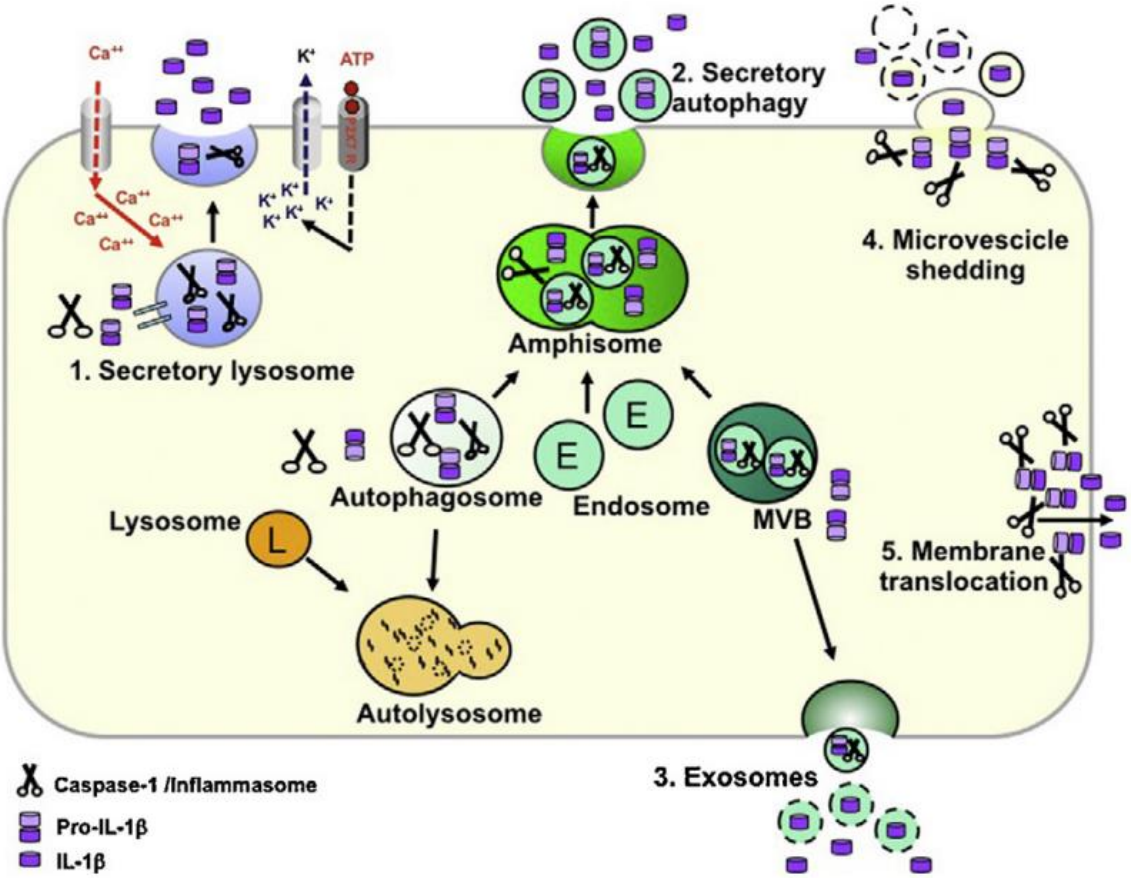

Figure 5 Unconventional pathways of IL-1β secretion [95]

(1) Secretory lysosomes involved in IL-1β secretion. (2) Autophagy mediates IL-1β secretion. (3) IL-1β secretion via MVB and exosomes. (4) Microvesicle shedding mediates IL-1β secretion. (5) Direct membrane translocation mediates IL-1β secretion.

1.2.3 NLRP3 inflammasome and IL-1β in AMD

While IL-1β is released into the extracellular space, its subsequent signaling is mediated by the IL-1 receptor to generate biologic responses. It has been reported that two IL-1 receptors exist on the cell surface; IL-1R1 that consists of an extracellular domain, an intracellular domain, and a transmembrane domain, as well as IL-1 type 2 receptor (IL-1R2) which is a decoy receptor. The binding of IL-1β to IL-1R1 also requires an accessory protein (IL-1RAcP) to increase the binding affinity and initiate downstream signal transduction pathways [96]. This trimeric receptor complex accompanied by IL-1 receptor-activated kinases (IRAKs) and myeloid differentiation primary response protein 88 (MyD88) triggers a dominant proinflammatory response, including the activation of transcription factors NFκB and AP-1 and the expression of proinflammatory cytokines such as IL-6, TNF-α, and nitric oxide (NO).

A considerable amount of studies has indicated that NLRP3 inflammasome and IL-1β related inflammatory pathways are implicated in AMD. It has been found that the upregulation of NLRP3 inflammasome was detected in RPE and adjacent drusen from human ocular tissue

sections of patients with geographic atrophy and neovascular AMD [97]. Consistent with this observation, IL-1β was shown to be markedly elevated in vitreous samples from patients with neovascular AMD [98]. In the aged VEGFA^{hyper} mice, which reproduce features of both nonexudative and neovascular AMD, NLRP3 inflammasome was activated, and targeting NLRP3 attenuated CNV formation [99]. Meanwhile, Lavslette *et al.* reported that IL-1β expression rapidly increased after laser injury and IL-1β inhibition significantly reduced the development of neovascularization in the laser-induced AMD mouse model [100]. Overall, these studies highlight that NLRP3 inflammasome and IL-1β play key roles both in the initiation and the progression of wet AMD. Further investigation on the NLRP3 inflammasome and IL-1β signaling pathway may, thus, lead to potential novel therapeutic strategies for AMD.

1.3 Endolysosomal Two-Pore Channels

1.3.1 Endolysosomal system

The endolysosomal system is composed of extremely dynamic and tightly organized membranous organelles in the endocytic pathway (Figure 6) that are primarily involved in the uptake of fluid, macromolecules, lipids, bacteria, viruses, receptor-bound ligands, and other compounds from the cell microenvironment for degradation or recycling of internalized material and plasma membrane components. With the first discovery of lysosomes using ultracentrifugation to isolate subcellular fractions [101], the understanding of the endocytic pathway has been improved and other endolysosomal compartments have been identified over the years. From the ultrastructural and functional point of view, endolysosomal organelles can be classified into early endosomes (EE), recycling endosomes (RE), late endosomes (LE), and lysosomes (Figure 6). During endolysosomal trafficking, the endocytic vesicles, budding from the plasma membrane, are instantly transported to EE which are distributed throughout the peripheral and perinuclear cytoplasm. They contain Rab5 and its effector early endosome antigen 1 (EEA1). EE, also referred to as RE, are the major sorting compartments where the majority of cargoes are recycled back to the cell surface, while other contents are destined for lysosomal degradation. The components circuiting to the degradative system are transported by multivesicular bodies (MVBs) from EE to LE. LE mature out of EE by exchanging Rab5 for Rab7 [102]. They accumulate and concentrate internalized contents that are delivered from EE. Furthermore, LE is also involved in the transportation of lysosomal enzymes from the *trans*-Golgi network (TGN) to lysosomes. A large number of lysosomal hydrolases are delivered from TGN to LE via transport vesicles. Endosome content degradation is finally achieved by LE fusion with lysosomes. LE and lysosomes exchange membrane components in a manner of transient (kiss-and-run) fusion [103]. Finally, hydrolase activities and

degradative processes take place in the lysosomal lumen that is the reservoir of hydrolase with a low acidic pH.

By coordinating the variety of processes, such as sorting, recycling, storing, and degrading, the endocytic pathway maintains cellular homeostasis and regulates numerous functions in different cell types. Apart from the primary function of degradation and recycling, a growing body of information provides new insights into the endolysosomal organelles. It has been reported that lysosomes also mediate a secretory pathway, known as lysosomal exocytosis, to repair the damaged plasma membrane and promote cellular clearances [104]. In addition, inward budding from the late endosomal membrane can generate exosomes, which are secreted into the extracellular space via fusion with the plasma membrane. Studies from recent years implicate exosomes in the regulation of immune responses and intercellular communication [105]. Moreover, the importance of the endolysosomal system is also highlighted in cell survival and cell death. Therefore, further comprehensive studies are required to decipher the functions and inter-organellar communication mediated by the endolysosomal system, particularly in the context of diseases.

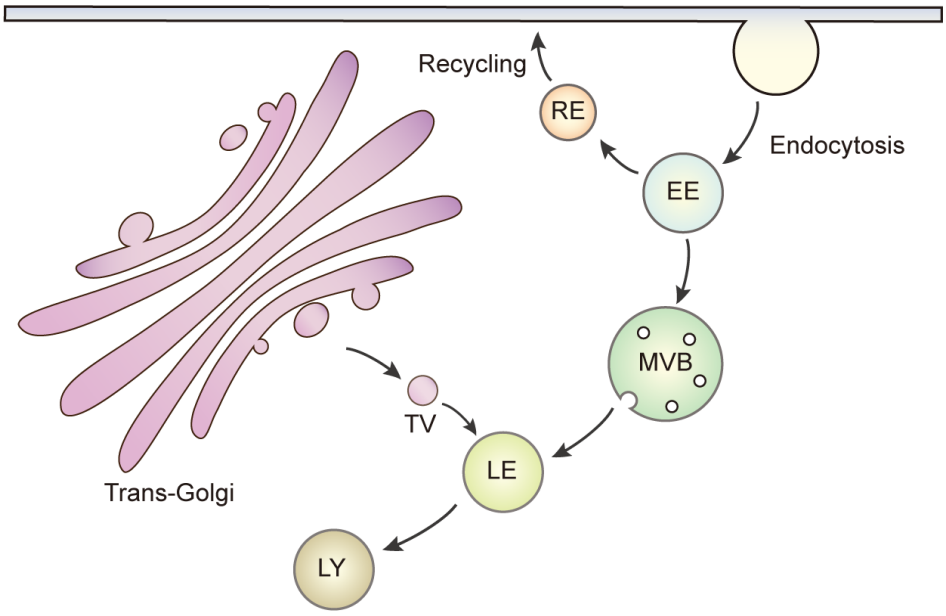

Figure 6 Schematic of endocytosis pathway.

The endocytic vesicles are budded from plasma membrane and fuse with early endosome (EE). Internalized components are sorted and recycled back to the plasma membrane via recycling endosomes (RE). Material destined for degradation was transported by multivesicular bodies (MVB) to late endosomes (LE). Lysosomal hydrolase was delivered from trans-Golgi network to late endosome via transport vesicles (TV). At last, late endosomes fuse with lysosomes (LY).

1.3.2 TPCs and their role in disease

Endolysosomal trafficking is mainly modulated by the ion channels located on the endosome membrane. Two pore channels (TPCs) are important eukaryotic ion channels, exclusively expressed in endolysosomal organelles of many tissues and cell types [106-108]. The primary structure of TPCs has been identified that comprises two repeats of a six-transmembrane pore-forming domain [109-111], which are homologous to four domain repeats of voltage-gated Ca^{2+} and Na^{+} channels (Ca_v and Na_v), as well as one domain repeat of transient receptor potential (TRP) channels (Figure 7) [112]. There are two functional isoforms of TPCs in human and most mammals, TPC1 and TPC2. These two isoforms have different patterns of subcellular distribution: TPC1 shows a wide range of localization in recycling endosomes, early and late endosomes, and lysosomes, while TPC2 predominantly resides in late endosomes and lysosomes [113]. Over the last few years, technical advancements allowed for the establishment of endolysosomal ion channel patch-clamp techniques which facilitated the investigation of TPC function and regulation. Numerous studies established that TPCs are non-selective cation channels permeable to Ca^{2+} [107, 114, 115]. It has been discovered that this Ca^{2+} permeability is mediated by the intracellular Ca^{2+}-mobilizing messenger nicotinic acid adenine dinucleotide phosphate (NAADP) [116]. Unlike the other two Ca^{2+}-mobilizing messengers, inositol 1,4,5-trisphosphate (IP_3) and cyclic adenosine diphosphate ribose (cADPR) that target the endo/sarcoplasmic reticulum (ER/SR), NAADP mainly targets the acidic Ca^{2+}-storing endosomes. Nevertheless, the NAADP-evoked local Ca^{2+} signal can further amplify Ca^{2+} release from ER/SR to generate global Ca^{2+} signals through Ca^{2+}-induced Ca^{2+} release (CICR) [117, 118]. Along this line, subsequent studies further demonstrated that TPC2 acts as an indirect downstream target of NAADP. Cells overexpressing TPCs showed a high affinity for NAADP and amplified Ca^{2+} release [108], while NAADP sensitivity was eliminated in TPC knockout cells [107]. However, the role of TPCs in NAADP-mediated Ca^{2+} release was challenged by recent findings that TPCs can also be permeable to Na^{+} and regulated by phosphatidylinositol 3,5-bisphosphate ($PI(3,5)P_2$) [119, 120]. Using whole-endolysosome patch-clamp recordings Wang *et al.* directly measured TPC-mediated Na^{+} flux in response to $PI(3,5)P_2$ [119]. Notably, it has been determined that TPC current, activated by $PI(3,5)P_2$, can be inhibited by mTOR kinase complexes [121].

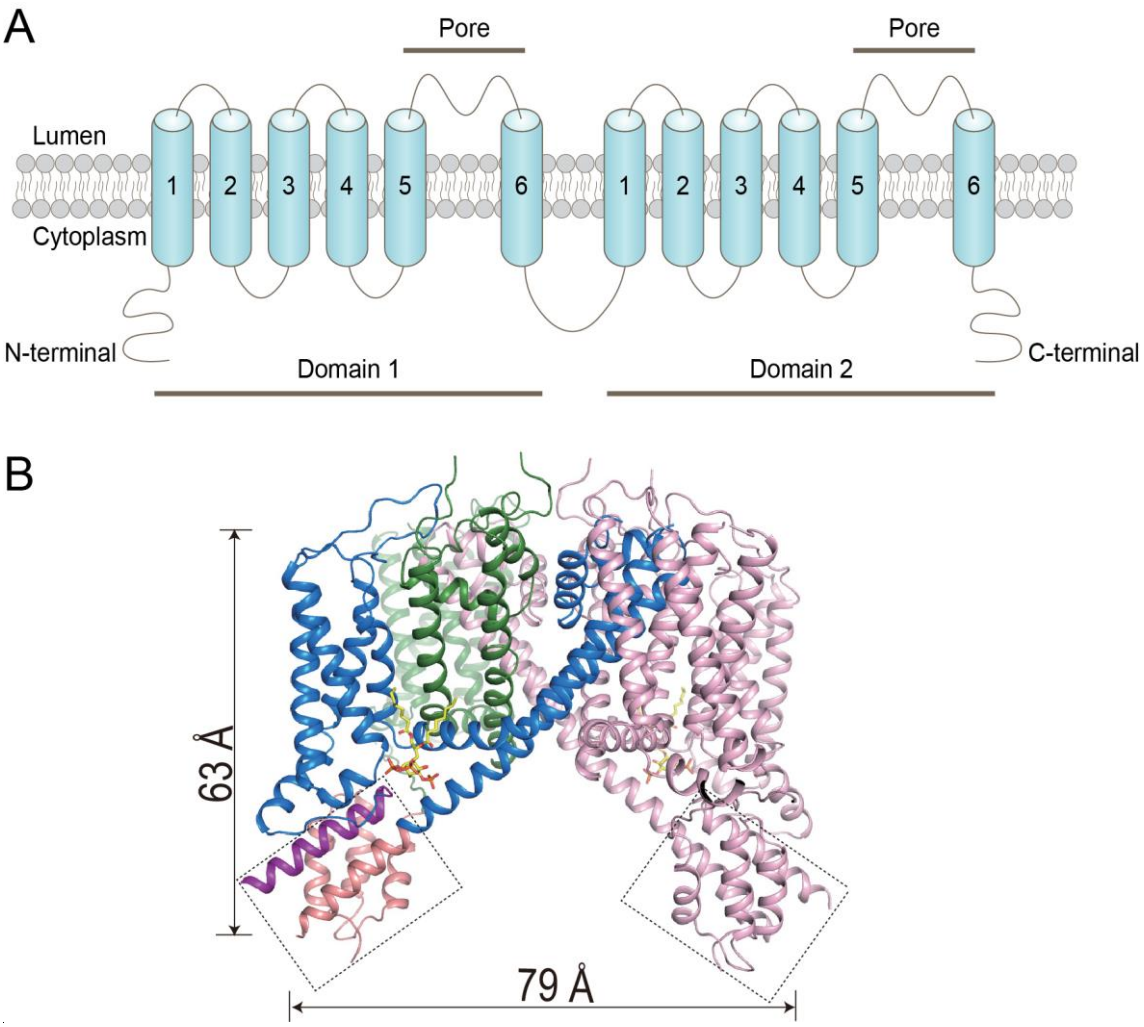

Figure 7 Schematic of TPCs channels topology and domain arrangement [111].

(A) TPCs are composed of two repeats of a six-transmembrane pore-forming domain with N- and C- terminal domains residing in the cytoplasm. (B) HsTPC2 Cryo-EM structure [111].

In line with their localization in the endolysosomal system and their function as cation channels, it was suggested that TPCs participate in the regulation of multiple endolysosomal trafficking pathways and are implicated in various pathological processes. The alteration of TPC expression can affect the size and subcellular localization of endolysosomal organelles [122]. Loss-of-function studies provided evidence that trafficking of various receptors and cargos such as LDL-cholesterol, EGF/EGFR, and PDGFR are impaired in the absence of TPC2 [113, 123]. Furthermore, TPCs have been implicated in the trafficking of bacterial toxins such as cholera toxin [122] and viruses such as the Ebola virus [124] or the Middle East Respiratory Syndrome coronavirus (MERS-CoV) [125]. It has also been found that TPC activity can affect cancer cell migration [126], autophagy [127], and human hair pigmentation [128]. In pathophysiological processes, TPCs appear to have a role in Parkinson's disease [129], diabetes [130], and cardiac dysfunction [131]. TPCs have also been implicated in immune

signaling processes, including mast cell degranulation [132] and exocytosis of lytic granules in CD8+ T lymphocytes [117]. There is also evidence for a role of TPC2 in signaling pathways that mediate VEGFA-induced angiogenesis [133]. With growing evidence linking physiological and pathophysiological processes to TPCs, suggest that the pharmacological targeting of these channels may be clinically beneficial. To this end, further investigation of the exact mechanism and possible novel functions of TPCs would be necessary to understand and treat endolysosome-related diseases.

2 Aim of the study

AMD is considered a multifaceted disease due to the complex interactions between environmental and genetic factors. Although there is extensive ongoing research in both the pathogenesis and therapy of AMD, the pathological mechanisms of this disease remain obscure. Two-pore channels (TPCs) has been shown to control blood vessel outgrowth that is the main feature of AMD. While their roles in pathological process of AMD remain unclear. To address this knowledge gap, this study is designed to explore whether TPCs play a role in the pathology of neovascular AMD.

The goal of first part of this study was to establish the laser-induced choroidal neovascularization (CNV) mouse model that represents the current gold standard preclinical model of AMD. Based on this model, the effect of TPC2 and TPC1 on leaky blood vessels and inflammatory response should be evaluated using genetic and pharmacological approaches. The levels of specific inflammatory cytokines would be measured in laser-damaged eyes from WT and TPCs knockout mice. Subsequently, further experiments should be performed in additional neoangiogenesis models to test whether TPCs directly contributes to blood vessel outgrowth.

Furthermore, molecular biology, biochemistry and electrophysiology experiments should be performed to determine TPCs expression and function in specific cell types including RPE, microglia and/or macrophages. Given that retinal microglia and infiltrating macrophages are key players in neovascular AMD, these cells should be characterized in more detail with regard to TPCs-mediated functions, in particular, by assessing their migration ability and cytokine release.

3 Material and Methods

3.1 Mice

Animal experiments were approved by the District Government of Upper Bavaria in accordance with the German Animal Welfare and Institutional guidelines. Animals were raised in 12-hour light-dark cycles with food (Ssniff; regular feed: R/M-H; breeding feed: M-Z Extrudat) and water. *Tpc2*$^{-/-}$ mice were generated as described [123] and breaded on mixed Sv129/C57BL/6J genetic background. For some experiments with TPC blocker, WT C57BL/6J mice were used.

3.2 Chemicals, solutions, and buffers

All chemicals used in this study had the quality of “ACS grade” or “for molecular biological use”. For all solutions high pure and deionized water was used (Millipore, Milli-Q Academic Ultra Pure Water Purification System). Additionally, all solutions and buffers were autoclaved (Sterilisator, Münchener Medizin Mechanik).

3.3 Laser-induced choroidal neovascularization (CNV) mice model

3.3.1 Laser photocoagulation

All animals used in this model were between 6 and 8 weeks of age and of female gender. Before injecting anesthesia, mice eyes were checked to exclude abnormal and deformed eyes. Only healthy and intact eyes were used for the experiment. Mice were weighed and anesthetized by intraperitoneally injecting with a mixture of ketamine (40 mg/kg body weight) and xylazine (20 mg/kg body weight). Pupils were dilated with tropicamide eye drops (Mydriadicum Stulln, Pharma Stulln GmbH). Mice were placed on a warm stage in order to avoid hypothermia caused by anesthesia. After waiting 2 min for tropicamide taking effect, hydroxypropyl methylcellulose (Methocel 2%; OmniVision GmbH) was applied to both eyes to keep eyes moist.

The retinal fundus was observed with an imaging camera on the Micron (Micron IV Retinal Imaging Microscope, Phoenix Research Laboratories). The Micron was turned on and firstly used to assess the extent of pupillary dilation. Once pupils were sufficiently dilated, laser procedure has proceeded. A warm stage where mice lay was adjusted to the appropriate position and distance in order to visualize major retinal vessels on the monitor screen. Mice eyes were slightly oriented and aligned to the objective lens of Micron. The optic disc should be positioned in the center of the whole fundus view. Then the lens was slowly moved toward the eyes until attaching the cornea. The further adjustment of focus and position was required to re-place the optic disc in the center and get clear and bright retinal major vessels in all

directions. This initial adjustment of focus is the key to successfully induce consistent CNV lesions.

Once accurate focus was obtained, laser photocoagulation was performed using the image-guided laser system (Phoenix Research Laboratories). The fundus and laser aiming beam could be viewed on the monitor screen. The following parameters of Argon laser pulse were used: laser wavelength, 532 nm; burn duration, 70 ms; energy, 280 mW for mixed-background *Tpc2*$^{-/-}$ and litter-matched WT mice and 230 mW for C57BL/6J mice. Four laser burns per eye were injected on both eyes in an equal distance with a double diameter of the optic disc from the optic disc border. Major vessels should be avoided to prevent bleeding. The success of the laser burn was implicated by the formation of a vaporization bubble around the laser-injected point immediately after laser photocoagulation. Unsuccessful laser burns or damages such as hemorrhages should be excluded for further evaluation. Finally, the injected eyes were treated with antibiotic ointment, Dexamytrex (Dr.Gerhard Mann GmbH). Mice were then kept on a warming plate at 37 °C until they recovered.

3.3.2 Fundus fluorescein angiography (FFA)

Angiographic analysis of CNV leakage was performed on day 7 and 14 post-laser coagulation. Mice were anesthetized and pupils were dilated as described above. Mice received a subcutaneous injection of fluorescein sodium solution (7.5 mg/kg, Alcon Deutschland GmbH) to visualize vessels. Fundus fluorescein angiography (FFA) was performed 5-10 min after the injection with the retinal imaging microscope (Phoenix Research Laboratories). The original and fluorescent fundus could be observed on the monitor screen. Excessive laser burns that also damaged other retinal layers and the lesions which fused with other lesions should be excluded for analysis. Leakage areas were quantified using ImageJ64 software (National Institutes of Health, USA). The leakage areas labeled with fluorescent dye were outlined with a freehand selection tool. The selected area was then measured and shown in pixel units.

3.4 Intravitreal injection

For the study of CNV model with TPC blockers, tetrandrine (Cat.T2695) was purchased from Sigma-Aldrich and reconstituted in dimethylsulfoxide (DMSO, Sigma-Aldrich) as a stock concentration of 5 mM. For experiments, the tetrandrine stock solution was diluted in phosphate-buffered saline (PBS) with a final concentration of 10 µM for *in vivo* model. Similarly, Ned-19 (Tocris, Cat.3954) was dissolved in DMSO with a stock concentration of 100 mM and subsequently diluted in PBS with a working concentration of 2 mM for *in vivo* study. DMSO solution with identical concentrations was prepared in the same manner and served as control. For intravitreal injection of TPC blockers, mice were anesthetized and pupils were dilated as described above. The injection was performed under the surgical microscope (OPMI 1 FR pro,

Zeiss). Mice were laid under the microscope and eyes were placed in an appropriate orientation. Eyeballs were exposed by pulling eyelids toward forehead using angled microforceps. TPC blockers or respective vehicles were filled in 10-µl glass syringe (Hamilton) mounted with a 34-gauge needle (World Precision Instrument). The needle was inserted at a 45° angle through the region of superior sclera into the vitreous. Using surgical microscope, the position of the needles within the eye was monitored to avoid touching the lens. 1 µl of 10 µM tetrandrine or 2 mM Ned-19 were intravitreally applied to right eyes. Left eyes were used for vehicle controls. After the injection, the needle was kept in the eye chamber for a few seconds in case of reflux of solution. Then laser photocoagulation was performed immediately after intravitreal injection.

Phosphate-buffered saline (PBS)

NaCl	137 mM
Na_2HPO_4 x $2H_2O$	8 mM
KH_2PO_4	1.76 mM
KCl	2.7 mM

Adjust pH to 7.4.

3.5 Choroidal sprouting assay

For choroidal sprouting culture, 21 to 25-day-old mice were used. Mice were euthanized and eyeballs were immediately enucleated and transferred into cold medium. The connective tissues around eyeballs were cleared and the anterior part of the eye including cornea and lens were removed. Next, the retinal pigment epithelium (RPE)/choroid/sclera complex separated from retina were cut into approximately 1 mm x 1 mm fragment. They were then embedded in growth factor-reduced matrigel (Corning, Cat.354230) in 24-well plates. 1 ml pre-warmed complete medium, including EBM™-2 Basal Medium (Lonza, Cat.CC-3156), EGM™-2 SingleQuotsTM Supplements (Lonza, Cat.CC-4176) containing VEGFA and 100 U/ml penicillin/streptomycin (Sigma-Aldrich, Cat.P0781), was added to each well. For WT and *Tpc2*$^{-/-}$ sprouting culture, RPE/choroid/sclera pieces were pre-incubated in complete medium for 2 days before placing in the EBM™-2 basal medium without EGM™-2 SingleQuots™ Supplements for another 2 days. In experiments with TPC blockers, tetrandrine stock solution was diluted in culture medium with a final concentration of 5 µM. Ned-19 stock was diluted with a working concentration of 100 µM in the same way. DMSO solutions with respective concentrations were prepared in the same manner and served as controls. After dissection, tissue pieces were cultured for 4 h in complete medium once embedded in matrigel. Thereafter,

medium was replaced with fresh medium containing 5 µM tetrandrine, 100 µM Ned-19, or vehicle controls.

Cultures were incubated at 37 °C with 5% CO_2 and the medium was replaced every 48 h. Phase-contrast images of tissue pieces were taken every day with EVOS M5000 microscope (Thermo Fisher Scientific) between day 1 and day 4. Sprouting areas were analyzed using the ImageJ64 software with SWIFT-choroid macros developed by Z Shao and M Friedlander [134]. Choroidal images were open with ImageJ software. The wand tool with a tolerance value of 30% was used to select and outline the original choroidal tissue. After creating a selection by clicking the inside of tissue, the first macro was used to delete the choroidal tissue from the image and measure the choroid area in pixel units. The threshold was defined with suitable low and high values, then utilized to distinguish the microvascular sprouting area from the background. The freehand selection tool was used to select the threshold-outlined area. Analysis was performed with second macro. Threshold-outlined area in pixel units was displayed on the results table.

3.6 Primary cell culture

3.6.1 Peritoneal macrophages (PM) culture

PM was obtained from two to three-month-old WT and *Tpc2*$^{-/-}$ mice. A small incision in the outer skin of the peritoneum was cut using scissors and forceps. The inner skin lining the peritoneal cavity was then exposed by pulling the incision. 10 ml of cold PBS was injected slowly into the peritoneal cavity using a 20-gauge needle without injuring any organs. After gentle massaging the peritoneum for 2 min, fluid was collected by a 5 ml syringe and transferred into tubes kept on ice. Blood contamination should be avoided in this process. The collected cell suspension was centrifuged with a speed of 1000 × *g* for 10 min at 4 °C. The supernatant was discard and cell pellets were resuspended by RPMI 1640 medium (Thermo Fisher Scientific, Cat. 21875034) containing 10% heat-inactivated fetal bovine serum (FBS, Sigma-Aldrich, Cat.S0615) and 100 U/ml penicillin/streptomycin and seeded in a 6-well culture plate or sterile 12-mm-diameter glass coverslips (Glaswarentabrik Karl Hecht GmbH). For attachment, cells were incubated for 2 h at 37 °C in 5% CO_2. Thereafter, medium was replaced with fresh medium to remove the non-adherent cells. PM were cultured for 48 h and then used for RNA extraction or endolysosomal patch-clamp experiments.

3.6.2 Bone marrow-derived macrophages (BMDM) culture

BMDMs were prepared from two to three-month-old WT and *Tpc2*$^{-/-}$ mice. After euthanizing the mice, tibia and femur were isolated and sprayed with 70% ethanol. Tibia and femur were exposed by cutting away the outer skin and surrounding musculature. Then hip joints were cut using scissors and the exposed bone marrow was flushed out of the bones using a 25-gauge

needle mounted on the sterile 10 ml syringe loaded with cold PBS. Clumps were gently dissociated into single-cell suspension with the rubber end of the plunger from a 5 ml syringe following passing through a 40 µm cell strainer (VWR, Cat.734-0002) into a 50 ml tube. After centrifugation at 1000 x rpm for 10 min at room temperature, cell pellets were resuspended and cultured in RPMI 1640 medium supplemented with 10% heat-inactivated FBS, 40 ng/ml murine monocyte-colony stimulating factor (M-CSF; Miltenyi Biotech, Cat.130-101-703) and 100 U/ml penicillin/streptomycin at 37 °C with 5% CO_2 for 7 days to promote differentiation of cells into macrophages.

For the establishment of polarized BMDMs, cells were stimulated with 100 ng/ml lipopolysaccharide (LPS, ENZO, Cat.ALX-581-012-L00) and 20 ng/ml interferon-γ (IFN-γ, R&D system, Cat.485-MI-100) or with 20 ng/ml IL-4 (R&D system, Cat.404-ML-010) to induce polarization towards M1 or M2 phenotypes, respectively.

3.6.3 Retinal pigment epithelium (RPE) culture

6 to 8-week-old WT mice were used for RPE culture. Before RPE collection, 24-well plates were coated with 100% FBS overnight at 37 °C. Mice were euthanized and whole eyes were pulled gently to detach from ocular muscles using angled forceps. After placing eyes in a six-well plate containing 2 ml of cold PBS, the connective tissues and optic nerve were carefully cut away from the eyeball using a dissecting stereomicroscope. The cleaned eyeballs were transferred into DMEM medium (Gibco™, Cat.11320033) containing 4.5 g/l glucose (Sigma-Aldrich, Cat.G8769) overnight in the dark at room temperature. The day after, enzyme solution was prepared by dissolving 1.5 mg trypsin (Thermo Fisher Scientific, Cat.27250018) and 2 mg type I collagenase (Worthington Biochemicals, Cat.LS004196) in 1 ml of DMEM medium following by filtered with a syringe filter with 0.2 µm pore size. The single eye was incubated in 500 µl enzymatic solution for 1 h at 37 °C. To stop the enzymatic reaction, the eye was slightly transferred into fresh DMEM supplemented with 20% FBS after digestion. Dissection was performed immediately afterward. The sclera was carefully ripped from the site of optic nerve to expose RPE attached to the retina. The RPE sheets were then scratched and pulled from retina and cut into small pieces. The detached RPE sheets were collected with a 1 ml micropipette and centrifuged at 400 × *g* for one minute. After discarding supernatant and washing with PBS, RPE sheets were incubated in 0.05 % trypsin at 37 °C for 5 min for further dissociation. Digestion was stopped by adding fresh medium containing 20% FBS. In order to create sing cell suspension, RPE was gently pipetted up and down, no more than 10 times. Finally, RPE cell suspension was seeded in a coated 24-well plate and incubated at 37 °C, 5% CO_2. After 24 h incubation at 37 °C with 5% CO_2, cells were carefully replaced with fresh medium supplemented with 10% FBS and 100 U/ml penicillin/streptomycin.

3.6.4 Brain microglia culture

Before preparation of brain microglia culture, 24-well plate was coated with 500 µl of 10 µg/ml poly-D-lysine (Sigma-Aldrich, Cat.P7886) overnight and then washed with PBS three times. Fire-polished glass Pasteur pipettes with decreasing tip diameters were coated with 4 % BSA (Gibico™, Cat.15260037) before use. Brains were scooped out from 3 to 5-day-old pups, determined the weight, and then placed into cold Hank's Balanced Salt Solution (HBSS, Gibco™, Cat.14170112) without calcium and magnesium supplemented with 5 mM HEPES (Gibco™, Cat.15630056). Meninges were removed and cortices were cut into small pieces. These pieces were collected using a 5 ml pipette and transferred into a sterile 15 ml tube. After centrifuging at 300 × *g* for 2 min at room temperature, the upper supernatant was aspirated carefully. The remaining tissues were incubated in 1950 µl of 1 mg/ml papain (Sigma-Aldrich, Cat.5306) for 15 min in the 37 °C water bath. The tube was shaken from time to time during incubation. 50 µl of 10 mg/ml Deoxyribonuclease I (DNase I, Sigma-Aldrich, Cat.DN25) was added into a tube to digest DNA released from dead cells. Tissues were further subjected to mechanical pipetting using the wide-tipped, fire-polished glass pipette gently in order to avoid air bubbles. After another 10 min of incubation in water bath, tissues were dissociated with mechanical pipetting using fire-polished pipettes in decreasing diameter. Cell suspension was applied through a 40 µm cell strainer placed on a 50 ml tube to remove cell clumps. The number of homogenous cell suspension was determined using trypan blue (Thermo Fisher Scientific, Cat.T10282) and counted using Countess™ II FL automated cell counter (Thermo Fisher Scientific, Cat.AMQAF1000). Thereafter, cell suspension was centrifuged at 300 × *g* for 10 min at room temperature and supernatant was discarded. The remaining cell pellets were suspended in 90 µl of magnetic cell sorting (MACS) buffer per 10^7 cells and then mixed completely with 10 µl of CD11b MicroBeads (Miltenyi Biotec, Cat.130-049-601) per 10^7 cells. The mixture was incubated for 15 min at 4 °C and washed by adding 2 ml MACS buffer and centrifuging at 300 × *g* for 10 min. After discarding supernatant, cell pellets were resuspended in 500 µl MACS buffer and then proceeded to magnetic separation. Microglia were isolated by Magnetic-activated cell sorting (MACS) column technology (Miltenyi Biotec). LS column (Miltenyi Biotec, Cat.130-042-401) was placed in the magnetic field of MACS separator (Miltenyi Biotec, Cat.130-090-976). The column was rinsed with 3 ml buffer before use. Cell suspension was applied onto the column. Unlabeled cells passed through the column when washing with 3 ml buffer three times. Then column was removed from the separator and placed on a fresh 15 ml collection tube. 1 ml of MACS buffer was loaded onto the column and cells were flushed out by firmly pushing the plunger into the column. Cell number was determined again. After centrifuging at 300 × *g* for 2 min at room temperature and aspirating supernatant, cell pellet was gently resuspended by adding pre-heated microglia

medium consisting of DMEM-F12 medium (Gibco™, Cat.21331-020) supplemented with 10% heat-inactivated FBS and antibiotics and finally seeded into coated 24-well plates.

MACS buffer

1 x PBS	100 ml
BSA	0.5 g
2 mM EDTA	4 ml
autoMACS Rinsing Solution	1.45 L

Store at 4 °C.

3.6.5 Retinal microglia culture

The protocol of retinal microglia culture was established by Dr.Elisa Murenu. For the culture of retinal microglia, eyeballs were obtained from postnatal pups in the age of 8 to 10 days old. Retinas were delicately freed of both retinal pigmented epithelium and choroid. Dissection of eyes was performed in the presence of cold HBSS without calcium and magnesium supplemented with 5 mM HEPES. Tissues were later centrifuged at 1000 x rpm for 5 min, and the cell pellet resuspended in a medium mainly containing DMEM-F12, 10% heat-inactivated FBS, and 100 U/ml penicillin/streptomycin. After gentle pipetting, the suspension was transferred to a 25 cm^2-flask and maintained at 37 °C with 5% CO_2 until confluence was reached. The medium was replaced the first time after one week and later every 3 days. Then cells were detached by 0.05% trypsin for 5 min at 37 °C to remove astrocytes and Müller glia. The remaining retinal microglia were scraped by scraper and sub-cultured in 6-well plate or on 12-mm-diameter coverslips for further use.

3.7 Transwell migration assay

Bone marrows were cultured for 7 days for maturation. BMDMs were then stimulated with either 100 ng/ml LPS and 20 ng/ml IFN-γ or 20 ng/ml IL-4 for 48 h to induce M1 and M2 polarized cells respectively. BMDMs without any stimulations were defined as M0 macrophages. After 48 h of stimulation, cell culture medium was aspirated and cells were washed with calcium- and magnesium-free Dulbecco's phosphate-buffered saline (DPBS, Gibco™, Cat.14190094) three times. 3 ml of pre-warmed accutase (Thermo Fisher Scientific, Cat.A1110501) were added into the culture and incubated for approximately 10 min at 37 °C for cell detachment. When digestive activity was stopped by adding 3 ml medium, cells were detached and resuspended by pipetting. Cell suspension was transferred to the tube and centrifuged at 300 × *g* for 5 min. After removing the supernatant, cell pellets were resuspended by pre-warmed medium and the total cell number was determined.

To prepare the chemoattractant, RPMI 1640 medium was supplemented with 40 ng/ml M-CSF, 10% heat-inactivated FBS, and 100 U/ml penicillin/streptomycin. For migration, a 6.5 mm transwell with 8.0 µm pore polycarbonate membrane insert (Corning, Cat.CLS3422) was used. The 700 µl of chemoattractant was filled in each well of the 24-well companion plate. The upper chamber was transferred into the prefilled plate. Thereafter, 200 µl of cell suspension containing 1 x 10^5 of M0, M1, or M2 BMDMs were seeded into the chamber. Plates were then placed into the incubator at 37 °C for 6 h. After incubation, the upper chamber was transferred into another 24-well plate containing crystal violet solution (Sigma-Aldrich, Cat.C0775). Cells were fixed and stained for 10 min, then washed with water three times. Cells from the upper chamber were removed using a cotton swab. The insert was kept in an empty 24-well plate to dry each chamber. Migrated cells on the lower part of the membrane were observed and imaged using a phase-contrast microscope with a 20 x objective. Images from four different quadrants were taken for each experimental condition and analyzed with ImageJ64 software. The total number of migrated cells in each quadrant was counted with cell counter function. The mean of cell number was calculated and used for statistical analysis.

Crystal violet solution

Crystal violet	500 mg
Methanol	25 ml
Water	75 ml

Store at room temperature.

3.8 Endolysosomal patch-clamp experiment

Endolysosomal patch-clamp experiment was conducted by Dr. Cheng-Chang Chen. Cells were treated with vacuolin (Santa Cruz Cat. sc-216045) at 37 °C and 5% CO_2 for 1 h. Vacuolin was washed out at least 10 min before patch-clamp experimentation. Isolation-micropipettes were used to open up the plasma membrane of macrophages on the coverslips, and isolation the vesicle out of the cell. Afterwards, electrode-pipettes were applied to form whole-endolysosomal configuration for patch-clamping.

Macrophages and microglia were used for experiments within 2-10 days after preparation. Patch recordings were performed with an Axopatch 200B amplifier (Molecular Device) and a Digidata 1320A data acquisition system (Molecular Device). PClamp and Clampfit software were used to record and analyze data. Recording glass pipettes were polished and had a resistance of 4–8 MΩ. For all experiments, salt-agar bridges were used to connect the reference Ag-AgCl wire to the bath solution to minimize voltage offsets. Liquid junction potential was corrected. 1 µM $PI(3,5)P_2$ (water-soluble diC8 form, Echelon Biosciences) was

applied to evoke endogenous TPC2 currents on isolated endolysosomes [121]. 500 ms voltage ramps from -100 to +100 mV were applied every 5 s, holding potential at 0 mV. The current amplitudes at -100mV were extracted from individual ramp current recordings. All statistical analysis was done using Origin 8 software.

The required solutions were prepared as follows. All chemicals used were obtained from Sigma-Aldrich if not mentioned extraordinarily.

Cytoplasmic solution

K-MSA	140 mM
KOH	5 mM
NaCl	4 mM
$CaCl_2$	0.39 mM
EGTA	1 mM
HEPES	10 mM

pH was adjusted with KOH to 7.2, sterilized by passing through a 0.2 µm filter.

Luminal solution

Na-MSA	140 mM
K-MSA	5 mM
Ca-MSA	2 mM
$CaCl_2$	1 mM
HEPES	10 mM
MES	10 mM

pH was adjusted with NaOH to 4.6, sterilized by passing through a 0.2 µm filter.

1mM Vacuolin-1

Dissolve 1 mg of vacuolin-1 in 1.732 ml of DMSO; mix complete and store at 4 °C.

3.9 Interleukin-1β secretion assay

To induce interleukin-1β (IL-1β) expression and secretion, BMDMs were dissociated with accutase after culturing 7 days and seeded in 12-well plate to a cell density of 3 $\times 10^5$/well. Culture medium was replaced with 1 ml of fresh medium supplemented with or without 1 µg/ml Lipopolysaccharides (LPS) from Escherichia coli serotype O1101:B4 (Enzo, Cat. ALX-581-012-L001). Cells were primed with LPS for 4 h to induce pro-IL-1β expression, followed by adding 5 mM adenosine 5′-triphosphate (ATP, Sigma-Aldrich, A7699) for 5, 10, and 20 min to

stimulate the maturation and secretion of IL-1β. Afterwards, extracellular medium was collected and centrifuged at 10,000 × *g* for 30 min at 4 °C to remove cell debris. The supernatant was transferred to a fresh tube for enzyme-linked immunosorbent assay (ELISA) analysis. A mouse IL-1β/IL-1F2 Quantikine ELISA kit (R&D system, MLB00C) was used and performed according to the manufacture's instructions. Detailed experimental procedure was described below. The remaining cells were washed with PBS three times and lysed by adding 150 µl lysis buffer (0.5% Triton X-100, v/v) supplemented with cOmplete ULTRA Protease Inhibitor Cocktail tablets (Roche) using the mixer mill MM400 (Retsch) with the frequency of 30/s for 1 min. Cell lysate was centrifuged at 30,000 × *g* and 4 °C for 15 min and supernatant was transferred to a fresh tube for Western blot analysis. For immunocytochemistry, BMDMs or retinal microglia were seeded and cultivated in 12-mm-diameter coverslips at a density of 5×10^4/well or 2.5×10^4/well. Cultures were treated with 1 µg/ml LPS for 4 h, followed by stimulation with 5 mM ATP for 20 min as above. After washing with PBS, cells were fixed with 4% paraformaldehyde (PFA) and used for immunocytochemistry experiments.

Lysis buffer

Triton X-100	2.5 ml
5 M NaCl	15 ml
2.5 M $CaCl_2$	0.4 ml
H_2O	add to 500 ml

4% PFA

Paraformaldehyde	6 g
0.1 M PBS	add to 150 ml

Dissolve at 60 °C and filtrate sterilely.

3.10 Immunohistochemistry

Two weeks post laser photocoagulation, mice were sacrificed and their eyes were enucleated and placed in the cold 0.1 M PB buffer. Under a stereomicroscope (Stemi 2000, Zeiss), connective tissues and muscles were carefully cleaned from eyeballs without damaging the posterior region of sclera where lesion spots localized. Then eyeballs were transferred in 4% PFA for fixation. After 5 min of short fixation, eyes were returned into cold 0.1 M PB. In order to easily manipulate dissection, eyes were placed on the Whatman paper covered on the petri dish lid. The anterior part of the eyes including cornea and lens were excised carefully by cutting along the *ora serrata* using angled micro-scissors. The vitreous body was removed and the remaining part of the eye consisting of retina, RPE, choroid, and sclera were placed

into 4% PFA for 45 minutes for further fixation. After this, eyes were washed with 0.1 M PB for 5 min three times.

For flat-mount staining, retinas were removed from the eyes. Hereafter, the remaining RPE/choroid/sclera complexes were incubated in 1% Triton-X 100 for 30 min for permeabilization and then blocked in blocking buffer for another 30 min at room temperature. Tissues were incubated with primary antibodies diluted in blocking buffer overnight at 4 °C. On the next day, tissues were washed with 0.1 M PB for 10 min three times followed by incubated in secondary antibodies diluted in blocking buffer for 2 h at room temperature. After another washing step with 0.1 M PB for 10 min three times, cell nuclei were visualized with 5 µg/ml Hoechst 33342 solution (Thermo Fisher Scientific, Cat.H1399) for 30 min. The tissues were washed with 0.1 M PB for 10 min and flat-mounted on the glass object slides (Superfrost Plus microscopic slides, Thermo Fisher Scientific). They were finally covered with Fluoromount-G™ Slide Mounting Medium (Thermo Fisher Scientific, Cat.00-4958-02) and coverslips. All antibodies used are listed in Table 1. Images were obtained using the Leica TCS SP8 spectral confocal laser scanning microscope (Leica, Wetzlar, Germany), acquired with LASX software. Images were collected as Z-series stacks, then transformed into the maximum intensity projections for quantification. Positive staining areas were outlined and measure with LASX software.

To detect IL-1β expression in the retina, mice eyes from WT and *Tpc2*$^{-/-}$ mice were enucleated and processed after 24 h of laser treatment. Eyes were prepared and dissected as described above. Tissues including retina, RPE, choroid, and sclera were dehydrated in 30% sucrose overnight at 4 °C after fixation with 4% PFA. Hereafter, tissues were embedded in optimum cutting temperature compound (OCT, Electron Microscopy Sciences) and frozen on the dry ice. The frozen tissues were then cryosectioned at a thickness of 10 µm using a Leica CM3050 S cryostat (Leica), mounted on coated glass object slides (Superfrost Plus microscopic slides, Thermo Fisher Scientific) and stored at -20 °C for future use.

Retinal cryosections were thawed at room temperature and rinsed with 0.1 M PB. After a fixation step with 4% PFA for 10 min. Cryosections were washed with 0.1 M PB for 5 min and incubated in blocking buffer in a humidified chamber at room temperature for 1 h. Blocking buffer was then drained off from cryosections and primary antibody diluted in blocking buffer was applied. Cryosections were incubated in humidified chamber overnight at 4 °C. Antibodies solution was removed and cryosections were washed three times with 0.1 M PB for 10 min. Cryosections were subsequently incubated in secondary antibody diluted in blocking buffer in a humidified chamber at room temperature for 2 h. They were washed three times with 0.1 M PB for 10 min and stained with 5 µg/ml Hoechst 33342 solution for nuclei visualization. Finally, cryosections were washed with 0.1 M PB for 10 min and mounted in Slide Mounting Medium and coverslips. All antibodies used are listed in Table 1.

Images in single plane were obtained using the Leica TCS SP8 spectral confocal laser scanning microscope (Leica, Wetzlar, Germany) and acquired with LASX software. All of the images were collected in same parameters. To quantify IL-1β positive area in the retina, images were opened with ImageJ64 software. After adjusting to a suitable threshold, IL-1β signal was quantified as fluorescence intensity above the threshold. Subretinal region was outlined with Hoechst stained area. IL-1β positive area was shown as the area occupied by fluorescent signal in subretinal area. All of images were measured in the same range of threshold. To quantified Iba1 positive cells in subretinal area of sections, the number of cells positive for Iba1 staining was manually counted within each image. To quantify IL-1β signal in Iba1+ cells, The area of Iba1+ cells was outlined and served as region of interest (ROI). The value of IL-1β mean intensity was then measured in each ROI.

0.1 M PB

Na_2HPO_4 x $2H_2O$	28.48 g
$NaHPO_4$ x H_2O	5.52 g
H_2O	Add to 2 L
Adjust pH to 7.4	

Blocking Buffer

5% chemiblocker (Merck Millipore) and 0.4% Triton X-100 in 0.1 M PB.

Table 1 Antibodies used for immunohistochemistry

Antibody	Source	Dilution
Alexa Fluor 488-conjugated Isolectin GS-IB4	Thermo Fisher Scientific, I21411	1:25
rabbit anti-Iba1	Wako, 019-19741	1:500
rabbit anti-C5b-9	Abcam, ab55811	1:500
mouse anti-IL-1β	Cell Signaling, 12242S	1:50
rabbit anti-IL-1β	Abcam, Ab9722	1:500
guinea pig anti-Iba1	Synaptic System, 234004	1:500

Alexa Fluor 555 donkey anti-rabbit IgG	Invitrogen, A-31572	1:500
Alexa Flour 488 donkey anti-rabbit IgG	Invitrogen, A21206	1:500
Flourescein (FITC) donkey anti-guinea pig IgG	Jackson, 706-095-148	1:400
Alexa Fluor 647 goat anti-mouse IgG	Life Technologies, A21236	1:500

3.11 Immunocytochemistry

Peritoneal macrophages, BMDMs or retinal microglia were cultured onto sterile 12-mm-diameter coverslips. Cells treated or untreated with LPS and ATP were washed with PBS followed by fixation in 4% PFA for 10 min. After a washing step with PBS for 10 min three times, cells were blocked in PBS containing 5% ChemiBlocker and 0.1% Saponin (Sigma-Aldrich, Cat.47036) for 1 h at room temperature. Thereafter, cells were incubated with primary antibody diluted in PBS containing 5% ChemiBlocker and 0.1% Saponin in humidified chamber overnight at 4 °C. Cells were washed three times with PBS for 10 min and then incubated with secondary antibody diluted in PBS containing 5% ChemiBlocker and 0.1% Saponin at room temperature for 2 h. After another washing step with PBS for 10 min three times, cell nuclei were visualized with Hoechst 33342 solution. Ultimately, cells were washed with PBS and coverslips were placed cell layer down on a glass slide containing a drop of mounting medium. The cells were stored at 4 °C for later analysis. All antibodies used are listed in Table 2.

For immunostaining with choroidal sprouting assay, explants were washed with PBS three times. 4% PFA was then added for 60 min before permeabilization with PBS containing 5% ChemiBlocker and 0.5% Triton X-100 for 3 h at room temperature. After this, explants were incubated in primary antibody diluted in blocking buffer overnight at 4 °C. On the next day, secondary antibodies diluted in blocking buffer were applied after the washing step with PBS for 15 min three times. After incubation overnight at 4 °C, explants were subjected to another washing step and cell nuclei were visualized with Hoechst 33342 solution. Finally, explants were covered with mounting medium and coverslips and then store at 4 °C for later analysis. All antibodies used are listed in Table 2.

Images were obtained using the Leica TCS SP8 spectral confocal laser scanning microscope (Leica, Wetzlar, Germany), acquired with LASX software, and quantified with ImageJ64 software. All of images were collected and processed with same setting and parameters.

Table 2 Antibodies used for Immunocytochemistry

Antibody	Source	Dilution
rabbit anti-IL-1β	Abcam, ab205924	1:500
rat anti-LAMP-1	Santa Cruz Biotechnology, sc-19992	1:120
rabbit anti-NG2 chondroitin sulfate proteoglycan antibody	Sigma-Aldrich, AB5320	1:250
rabbit anti-vimentin	Cell Signaling, 5741	1:100
rat anti-CD11b	Biolegend, 101202	1:500
mouse anti-Otx2	Origene, TA809511	1:250
Guinea pig anti-Iba1	Synaptic System, 234004	1:500
Alexa Flour 488 donkey anti-rat IgG	Thermo Fisher Scientific, A21208	1:500
Alexa Fluor 647 goat anti-rabbit IgG	Life Technologies, A32733	1:500
Alexa Fluor 555 donkey anti-rabbit IgG	Invitrogen, A-31572	1:500

3.12 Enzyme-linked immunosorbent assay (ELISA)

After 24 h or 48 h of laser treatment, eyes were enucleated from WT and *Tpc2*$^{-/-}$ mice. Eyes were dissected as described above and retinas harvested from the eyes were placed in 150 µl lysis buffer containing cOmplete ULTRA Protease Inhibitor Cocktail tablets for each eye. Subsequently, retinas were homogenized using the mixer mill MM400 with the frequency of 30/s for 30 s and rotated at 4 °C for 20 min. After centrifugation at 30,000 × *g* and 4 °C for 15 min, the upper supernatant was transferred to a fresh tube for ELISA analysis. For cell culture, extracellular medium was collected and centrifuged at 10,000 × *g* for 30 min at 4 °C to remove cell debris. The supernatant was transferred to a fresh tube for enzyme-linked immunosorbent assay (ELISA) analysis.

To determine the total protein concentration, Qubit Protein Assay Kit (Thermo Fisher Scientific, Cat.Q33211) was used following the manufacturer's instructions. The required number of 0.5-

mL assay tubes were prepared and labeled for standards and samples. The Qubit working solution was prepared by diluting the Qubit Protein Reagent 1:200 in Qubit Protein Buffer. For standard solution preparation, 190 µL of Qubit working solution and 10 µL of each Qubit standard were added to each of the tubes and mixed by vortexing. Thereafter, 3 µL of each sample was added to individual assay tubes containing 197 µL of Qubit working solution and mixed by vortexing. All tubes were incubated at room temperature for 15 min. Qubit® 3.0 Fluorometer (Thermo Fisher Scientific, Cat.Q33216) was used to measure and calculate protein concentration.

To determine the level of IL-1β in homogenized tissue supernatant or cell culture medium, a mouse IL-1β/IL-1F2 Quantikine ELISA kit (R&D system, MLB00C) was used and performed according to the manufacture's instruction. The required numbers of microplate stripes were set on the plate frame. Mouse IL-1β Standard was reconstituted with Calibrator Diluent RD5-16 in a stock concentration of 800 pg/ml and produced a dilution series with the concentration of 400 pg/ml, 200 pg/ml, 100 pg/ml. 50 pg/ml, 25 pg/ml, and 12.5 pg/ml. 50 µL of Assay Diluent RD1N was added to each well, and then 50 µL of standard, control, or sample were added to individual wells. The plate was covered and sealed with the adhesive strip provided and then incubated for 2 h at room temperature. Afterwards, solutions in each well were aspirated. Plates were washed five times by filling with wash buffer, then removing complete liquid. After the last wash, the remaining wash buffer was aspirated and the plates were inverted and blotted against clean paper towels for drying. 100 µL of Mouse IL-1β Conjugate was added to each well. The plate was covered with a new adhesive strip and incubated for 2 h at room temperature. The aspiration/washing step was repeated similarly five times. To develop, Color Reagents A and B were mixed in equal volumes within 15 min of use, protecting them from light. 100 µL of Substrate Solution was each well. After incubation for 30 min at room temperature, the reaction was stopped by adding 100 µL of Stop Solution to each well. Finally, the optical density of each well was determined using SpectraMax iD3 (Molecular Devices) at a wavelength of 450 nm with correction of wavelength at 540 nm. The concentration of IL-1β was calculated using standard curves obtained from solutions with known IL-1β concentration then normalized to total protein.

The level of VEGFA protein in the supernatant of retinal homogenates was determined using a MILLIPLEX MAP Mouse Cytokine/Chemokine Magnetic Bead Panel - Premixed 32 Plex - Immunology Multiplex Assay (MERCK, Cat. MCYTMAG-70K). A similar protocol was used as described above.

3.13 Western blot

Cell lysate was prepared and supernatant concentration was determined as described above. Total protein from cell lysates was boiled in 6 × Laemmli sample buffer supplemented with

DTT at 72 °C for 10 min. Protein was separated based on the molecular weight using SDS-PAGE gel. 6% and 12% gel solution were prepared according to the recipe. The gel gradient was generated using the glass plates assembled with spacers (Bio-Rad). 4.25 ml of 12% gel solution was poured followed by loading 4.25 ml of 6% gel solution without any air bubbles. 1 ml of isopropanol was overlayed to maintain an even and horizontal resolving gel surface. Thereafter, 5% stacking gel solution was added to make the entire SDS-PAGE gel. Samples containing 15 µg of protein in the same volume were loaded in SDS-PAGE wells. PageRuler Prestained Protein Ladder (Thermo Fisher Scientific) was used as a molecular weight marker. Electrophoresis was run in electrophoresis buffer at 100 V for 20 min then 150 V for 40 min.
For membrane transfer, PVDF membrane was activated in methanol before use. Protein was transferred using Mini Trans-Blot Cell (Bio-Rad) containing transfer buffer at the stable electric current of 350 mA for 1.5 h. After blotting, the membrane was blocked for 1 h at room temperature using blocking buffer followed by overnight incubation in the primary antibody diluted in blocking buffer at 4 °C. On the next day, the membrane was washed three times with TBST for 10 min. Hereafter, membrane was incubated in conjugated secondary antibody diluted in blocking buffer at room temperature for 2 h and washed three times with TBST for 10 min. For signal development, chemiluminescent substrate, Western Blotting Luminol Reagent (Santa Cruz) was used and prepared based upon manufacture instruction. Images were captured using the Chemidoc MP Imaging system (Bio-Rad) and the ImageLab software. All antibodies used were shown in Table 3.

Table 3 Antibodies used for western blot

Antibody	Source	Dilution
rabbit anti-IL-1β	Abcam, Ab9722	1:1000
mouse anti-β-tubulin	Cell Signaling Technology, 86298	1:1000
Donkey Anti-Mouse IgG (H+L)	Jackson, 715-035-150	1:2000
Donkey Anti-Rabbit IgG (H+L)	Jackson, 711-035-152	1:2000

6x Laemmli buffer

Tris-HCl pH 6.8	7 ml
Glycerol	3 ml
SDS	1.0 g

Bromophenol blue	1.2 mg
DTT	0.93 g
H_2O	add to 10 ml

1x Electrophoresis buffer

Tris base	3.03 g
Glycin	14.4 g
SDS	1.0 g
H_2O	add to 1 L

4x 0.5 M Tris-HCl/SDS buffer

Tris base	0.5 M
SDS	0.4%
H_2O	add to 500 ml

Adjust pH to 6.8.

4x 1.5 M Tris-HCl/SDS buffer

Tris base	1.5 M
SDS	0.4%
H_2O	add to 500 ml

Adjust pH to 8.8.

Stacking gel (for 2 gels)

30% acrylamide/bis-acrylamide	1 ml
4x 0.5 M Tris-HCl/SDS buffer	1.9 ml
H_2O	4.6 ml
APS	37.5 µl
TEMED	7.5 µl

6 % Gradient separation gel (for 2 gels)

30% acrylamide/bis-acrylamide	2.3 ml
4x Tris-HCl/SDS buffer 1.5 M	2.8 ml
H_2O	6.2 ml
APS	22.5 µl
TEMED	7.5 µl

12% Gradient separation gel (for 2 gels)

30% acrylamide/bis-acrylamide	4.6 ml
4x Tris-HCl/SDS buffer 1.5 M	2.8 ml
H_2O	3.9 ml
APS	22.5 µl
TEMED	7.5 µl

Transfer buffer

Tris	3.0 g
Glycin	14.4 g
H_2O	add to 1 L

TBST

Tris	1.2 g
NaCl	8 g
Tween 20	1 ml
H_2O	add to 1 L

Blocking solution

TBST	15 ml
Non-fat dried milk powder	0.75 g

3.14 Quantitative RT-PCR

RNA from cultured cells was extracted using RNeasy Plus Mini kit (Qiagen, Cat.74134) according to the manufacturer´s instructions. Cells were disrupted and homogenized in Buffer RLT Plus, and purified in gDNA Eliminator spin column, finally eluted in RNase-free water. The concentration and quality of isolated RNA were determined using a Nanodrop 2000c spectrophotometer.

For reverse transcription, cDNA was synthesized with the RevertAid First Strand cDNA SynthesisKit (Thermo Fisher Scientific, Cat.K1622) following the instruction of the manufacturer. The total amount of 150 ng RNA from cells as template RNA mixing with Oligo (dT) primer and Random Hexamer primer were used for first-strand cDNA synthesis. For PCR amplification of first-strand cDNA, 5 × Reaction Buffer, RiboLock RNase Inhibitor, 10 mM dNTP Mix as well as RevertAid M-MuLV Reverse Transcriptase was added into reverse transcription reaction product and amplified in the thermal ProFlex PCR system (Thermo Fisher Scientific).

qRT-PCR was performed using SYBR Select Master Mix (Applied Biosystems, Cat.4472903) according to the manufacture's instruction. The reaction mix was prepared by adding 2 × SYBR Select Master Mix, Forward and reverse primers, cDNA template, RNase-free water in a total volume of 20 µl for a 96-well plate. Three technical replicates were set for each gene of interest. qRT-PCR reaction plate was placed and run on a StepOnePlus Real-time PCR System (Applied Biosystems). Relative quantification was calculated according to the $2^{-\Delta\Delta}$CT method. Murine Hypoxanthine guanine phosphoribosyl transferase (Hprt) was used as the housekeeping gene. All primers used can be found in the appendix (Supplementary Table 1).

3.15 Statistics

All graphical data are represented as mean ±SEM for the indicated n values of the experiments. Statistical analysis was carried out using GraphPad Prism 7 or Origin 8 software. P-values were calculated by Student's *t*-test, Two-way ANOVA or One-way ANOVA with Tukey's multiple comparisons test. $P < 0.05$ were considered to show significant differences, $^{*}P < 0.05$, $^{**}P < 0.01$, $^{***}P < 0.001$, ns, no significate differences.

4 Results

4.1 Inhibition of TPC2 activity prevents excessive choroidal neovascularization in a mouse laser photocoagulation model of wet AMD.

To evaluate the potential role of TPCs in CNV pathogenesis, a laser-induced choroidal neovascularization mouse model of AMD was adopted. This model has proven to be a robust model for studying the complexity of AMD pathobiology and for evaluating efficacy of therapies for exudative AMD. In this CNV model, Bruch's membrane is damaged by focal laser photocoagulation, resulting in an inflammatory response, invasion of the lesion site by immune cells and formation of novel leaky choroidal blood vessels which grow into and damage the adjacent retina. The pathological neovascularization can be non-invasively monitored by fluorescein fundus angiography (FFA), which allows for visualization of the (major) blood vessels and vascular leakage areas. Figure 8A shows representative images of the normal fundus with four laser burns shown as bright spots from Tpc2-knockout (*Tpc2*$^{-/-}$, lower panel) and litter-matched WT (upper panel) mice on day 1 and day 7 after laser photocoagulation. FFA images were obtained at 7 and 14 days after laser treatment. Massive vascular leakage from CNV lesions were detected in WT mice (indicated by dotted lines in Figure 8A, upper panel). In comparison, retinas from *Tpc2*$^{-/-}$ mice showed a substantial reduction of leakage area at the lesion sites (Figure 8A, lower panel). The laser-induced CNV is a self-limiting model of neoangiogenesis and the lesion peaks at days 7-10 and regresses 2-3 weeks later [135]. We therefore firstly quantified the leakage area on day 7 which revealed an approximately 50% reduction (***P*<0.01) in *Tpc2*$^{-/-}$ compared with WT control mice (Figure 8B; n = 7 to 9 eyes/group). On day 14 after laser damage the leakage area started to regress, but a similar effect induced by TPC2 deficiency was still recorded (Figure 8C). Since TPC1 is homologous to TPC2, the effect of TPC1 on CNV formation was also evaluated using *Tpc1*$^{-/-}$ mice. This revealed no significant differences between the CNV responses in *Tpc1*$^{-/-}$ vs WT control mice (Figures 9A and B). As such, the following studies mainly focused on TPC2.

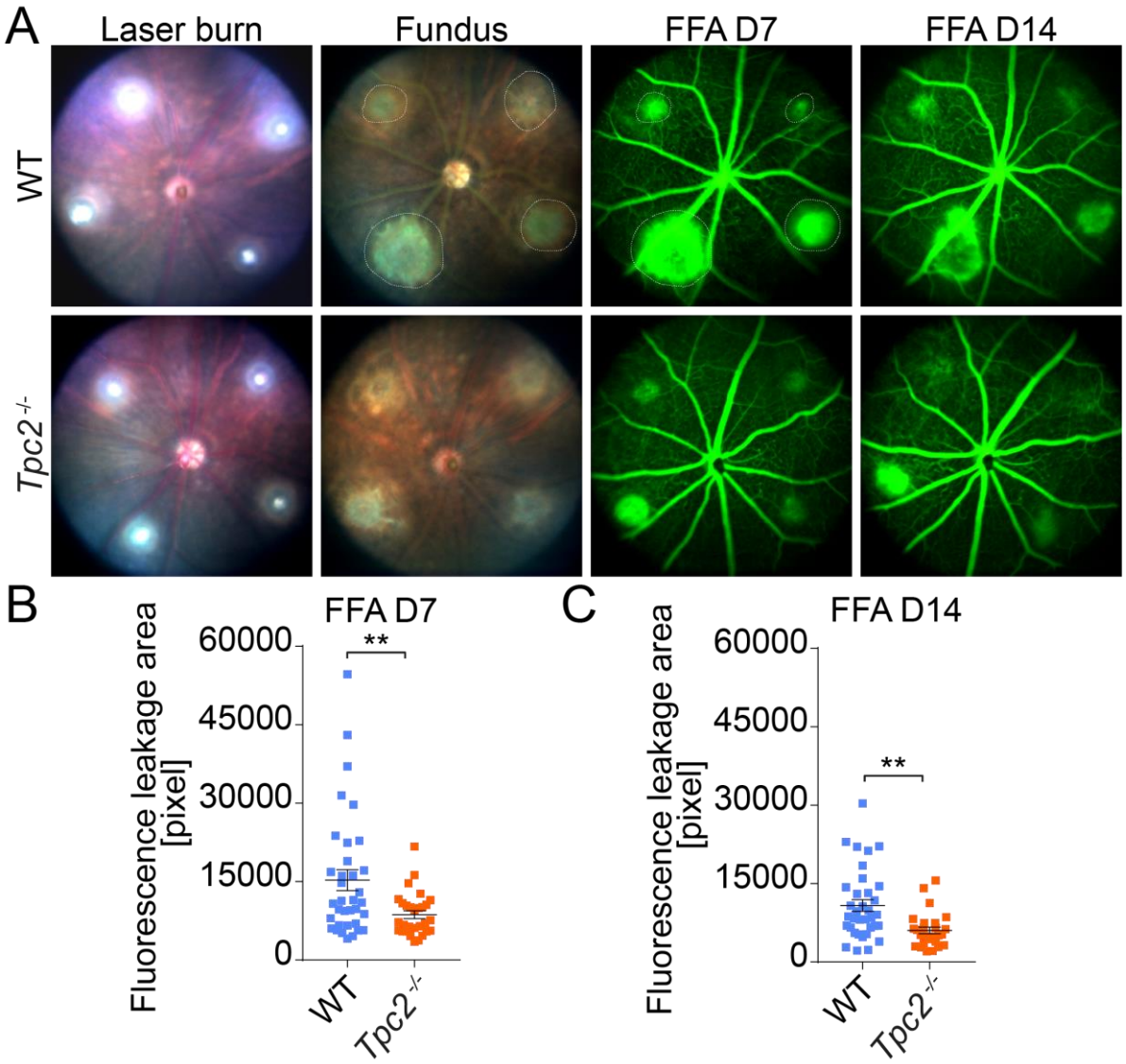

Figure 8 Genetic deletion of TPC2 attenuates choroidal neovascularization (CNV) in a laser-induced mice model.

(A) Representative images of normal fundus photography on day 1 and day 7 after laser damage with four laser burns from 6 to 8-week-old *Tpc2*$^{-/-}$ (lower panel) and litter-matched WT mice (upper panel) and corresponding fundus fluorescein angiography (FFA) images from 7 and 14 days after laser photocoagulation. Four laser burns are indicated by the dotted line in upper panel. (B, C) Quantification of vascular leakage areas by analyzing pixel intensities after 7 days (B) and 14 days (C) of laser-induced damage for WT versus *Tpc2*$^{-/-}$ mice. Each data point represents one lesion site on day 7 or day 14 after laser photocoagulation. Data are presented as mean ± SEM. Group size as n= 7 to 9 mice. Student's *t*-test was used for statistical analysis. ns, no significant difference, **P*<0.05, ***P*<0.01,****P*<0.001.

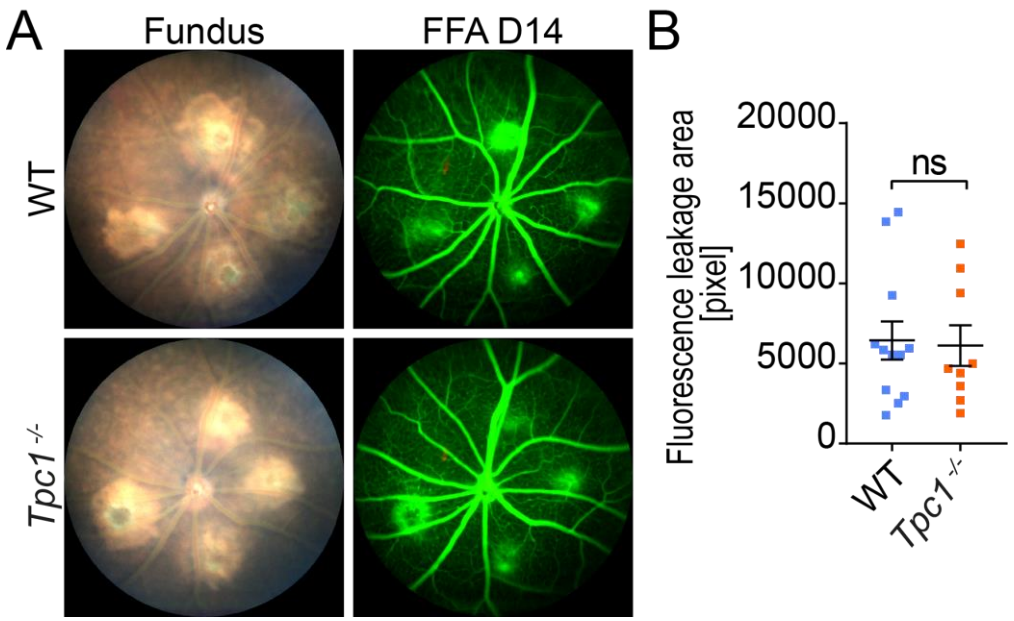

Figure 9 Genetic deletion of TPC1 has no effect choroidal neovascularization (CNV) in a laser-induced mice model.

(A) Representative images of fundus photography and FFA from 6 to 8-week-old *Tpc1*$^{-/-}$ (lower panel) and litter-matched WT mice (upper panel) at 14 days after laser photocoagulation. (B) Quantification of vascular leakage areas by analyzing pixel intensities after laser-induced damage for WT versus *Tpc1*$^{-/-}$ mice. Each data point represents one lesion site on day 14 after laser photocoagulation. Data are presented as mean ± SEM. Group size as n= 3 mice. Student's *t*-test was used for statistical analysis. ns, no significant difference, **P*<0.05, ***P*<0.01,****P*<0.001.

To confirm that the differences observed in *Tpc2*$^{-/-}$ mice dependent on TPC2 ion channel function and to exclude the potential contribution of developmental effects caused by the genetic deletion of *Tpc2* the effects of two established TPC channel blockers, tetrandrine [124] and Ned-19 [136], were evaluated on CNV formation in WT mice. 1µl of 10 µM tetrandrine or 2 mM Ned-19 was applied immediately before the laser treatment via single intravitreal injection and the extent of CNV was evaluated after 7 and 14 days. Both tetrandrine (Figures 10A, B and C) and Ned-19 (Figures 11A, B and C) significantly inhibited the laser-induced neovascularization to a similar extent as the genetic deletion of TPC2 on day 7 and day 14 after laser injury.

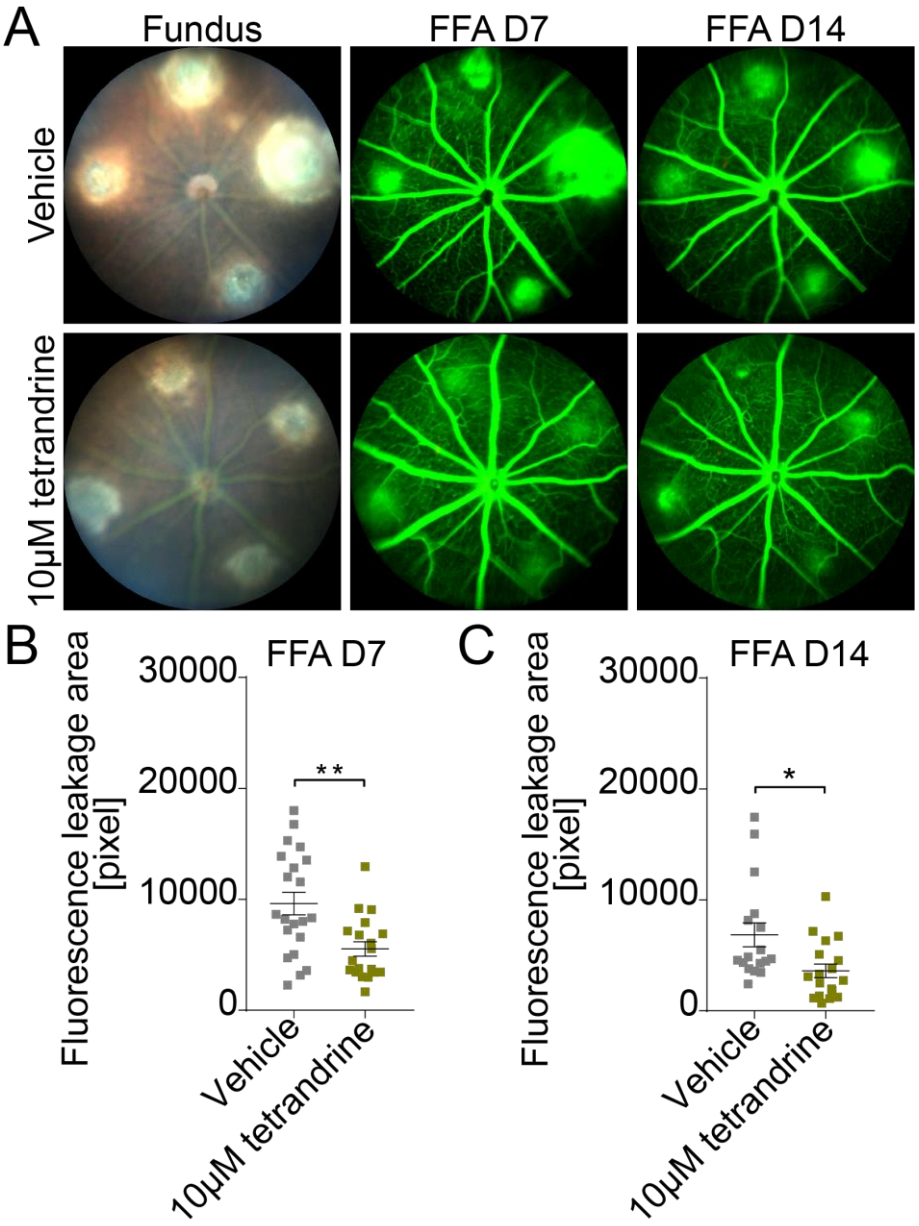

Figure 10 Pharmacological block of TPC2 activity with tetrandrine prevents CNV in a laser-induced mice model.

(A) Representative fundus and FFA images of C57BL/6J WT mice on day 7 and day 14 after laser photocoagulation. Mice were intravitreally injected into the right eyes with 1 µl of 10 µM tetrandrine (lower panel) and left eyes with vehicles in upper panel immediately before laser coagulation. (B, C) Quantification of vascular leakage in lesion sites for vehicles versus tetrandrine-treated eyes on day 7 (B) or day 14 (C) after laser damage. Each data point represents one lesion site. Data are presented as mean ± SEM. Group size as n = 6. Student's *t*-test was used for statistical analysis. **P*<0.05, ***P*<0.01, ****P*<0.001.

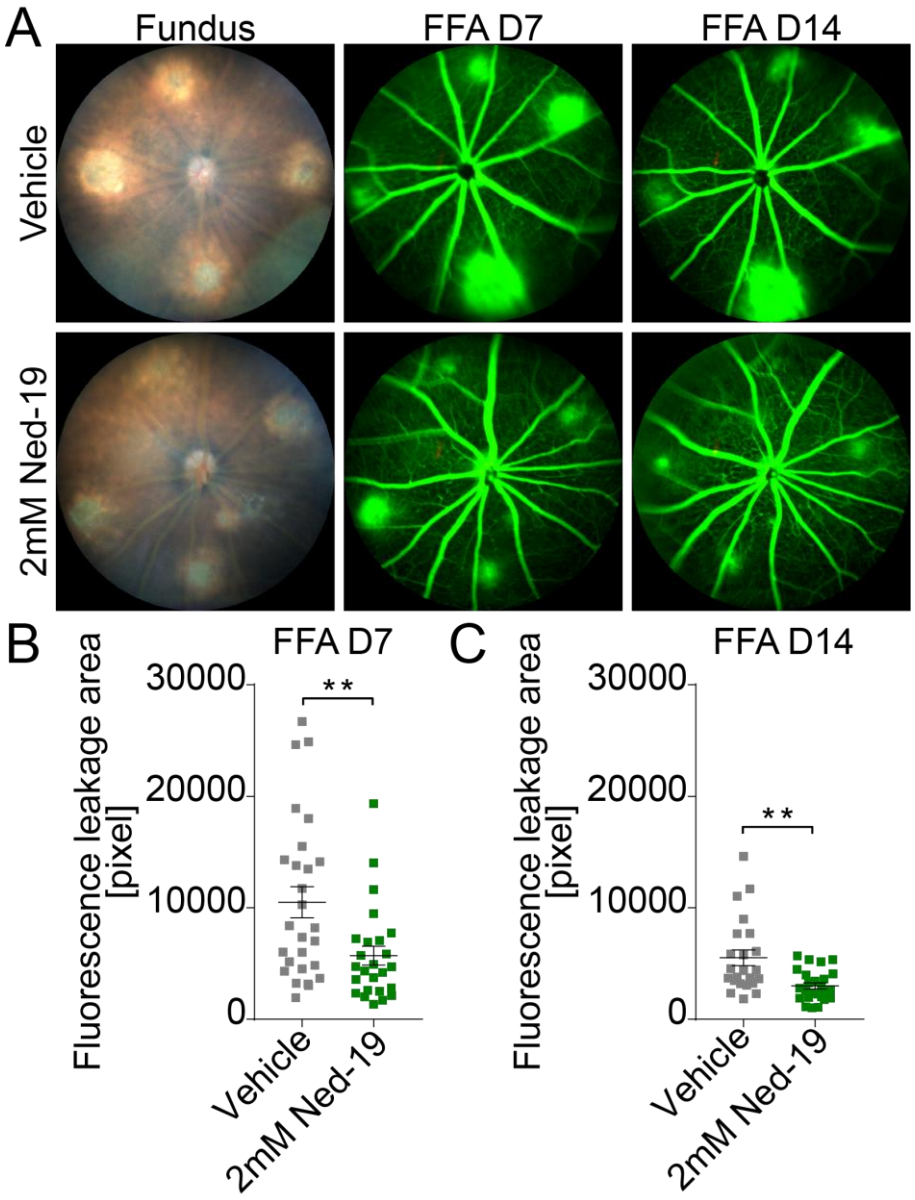

Figure 11 Pharmacological block of TPC2 activity with Ned-19 prevents CNV in a laser-induced mice model.

(A) Representative fundus and FFA images of C57BL/6J WT mice on day 7 and day 14 after laser photocoagulation. Mice were intravitreally injected into the right eyes with 1 µl of 2mM Ned-19 (lower panel) and left eyes with vehicles in upper panel immediately before laser coagulation. (B, C) Quantification of vascular leakage in lesion sites for vehicles versus Ned-19-treated eyes on day 7 (B) or day 14 (C) after laser damage. Each data point represents one lesion site. Data are presented as mean ± SEM. Group size as n = 6. Student's *t*-test was used for statistical analysis. **P*<0.05, ***P*<0.01, ****P*<0.001.

4.2 Block of TPC2 suppresses choroidal capillary sprouting.

To gain further insight into whether TPC2 directly modulates choroidal neovascularization, the effect of TPC2 was also explored on *ex vivo* choroidal vascular sprouting. Choroidal pieces with attached RPE and sclera were dissected from WT and *Tpc2*$^{-/-}$ mice, embedded in matrigel,

and cultured in endothelial cell growth medium containing VEGFA to induce microvascular sprouting. Vascular sprouting was visualized under a microscope. As shown in Figure 12A, choroid tissue developed vascular sprouting in a time-dependent manner. The microvascular areas were quantified using a computerized quantification method (SWIFT macro in ImageJ64 software, Figure 12B). From day 1 to day 4 of culture, WT tissues exhibited a dramatic increase of capillary sprouting area (Figure 13A, upper row). The sprouting was also primed in tissues from *Tpc2*$^{-/-}$ mice, while the sprouting area showed significantly less vascular growth compared with WT tissues at day 4 (Figure 13A, lower row). The statistical analysis of the sprouting area quantification of tissues revealed an approximate 50% reduction caused by deletion of TPC2 (221604 ± 24769 µm^2 in WT tissues VS 110706 ± 22460 µm^2 in *Tpc2*$^{-/-}$ tissues; n = 8 pieces/group) (Figure 13B). Immunostaining analysis indicated that microvascular sprouts from the choroid were positively stained with endothelial cell markers isolectin B4 (IB4), surrounded by NG2 positive pericytes and vimentin-positive fibroblasts (Figures 14A and B).

It is well established that VEGFA production plays a central role in triggering neovascularization in the laser-induced CNV model and human AMD pathology. Therefore, it was examined whether the absence of TPC2 could affect VEGFA expression by determining the levels of VEGFA in retinas of WT and *Tpc2*$^{-/-}$ mice at 48 h after laser coagulation (Figure 13C). Consistent with the reduced leakage area in *Tpc2*$^{-/-}$ mice, VEGFA levels were indeed also reduced in knockout mice compared to controls (7.236 ± 0.9083 pg/ml in WT retina; 3.172 ± 0.7426 pg/ml in *Tpc2*$^{-/-}$ retina, n = 5 to 6 eyes/group).

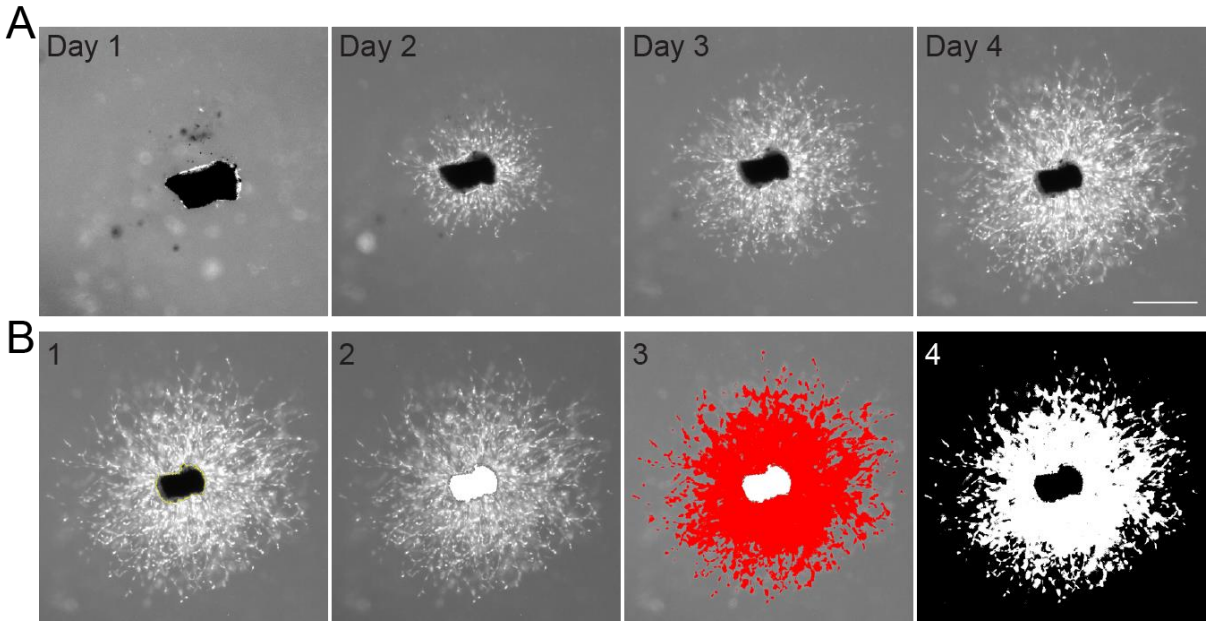

Figure 12 Microvascular sprouting from choroid tissue and quantification method of sprouting culture.

(A) *Ex vivo* choroidal sprouting assay of retinal tissue biopsies comprising RPE, choroid, and sclera. Tissues were cultured in matrigel and bright-field images were recorded every 24 h. Representative images of cultured choroidal tissue on day 1, 2, 3 and 4 respectively. Scale bar = 500 µm. (B) Microvascular sprouts on day 4 were processed and quantified with the SWIFT-Choroid macro in ImageJ64 software (NIH). (*1*) Outline of choroid tissue in the center of image; (*2*) Exclusion of choroid tissue; (*3*) Tracing microvascular area with suitable threshold; (*4*) Measuring the microvascular area and transforming images with SWIFT-Choroid macro.

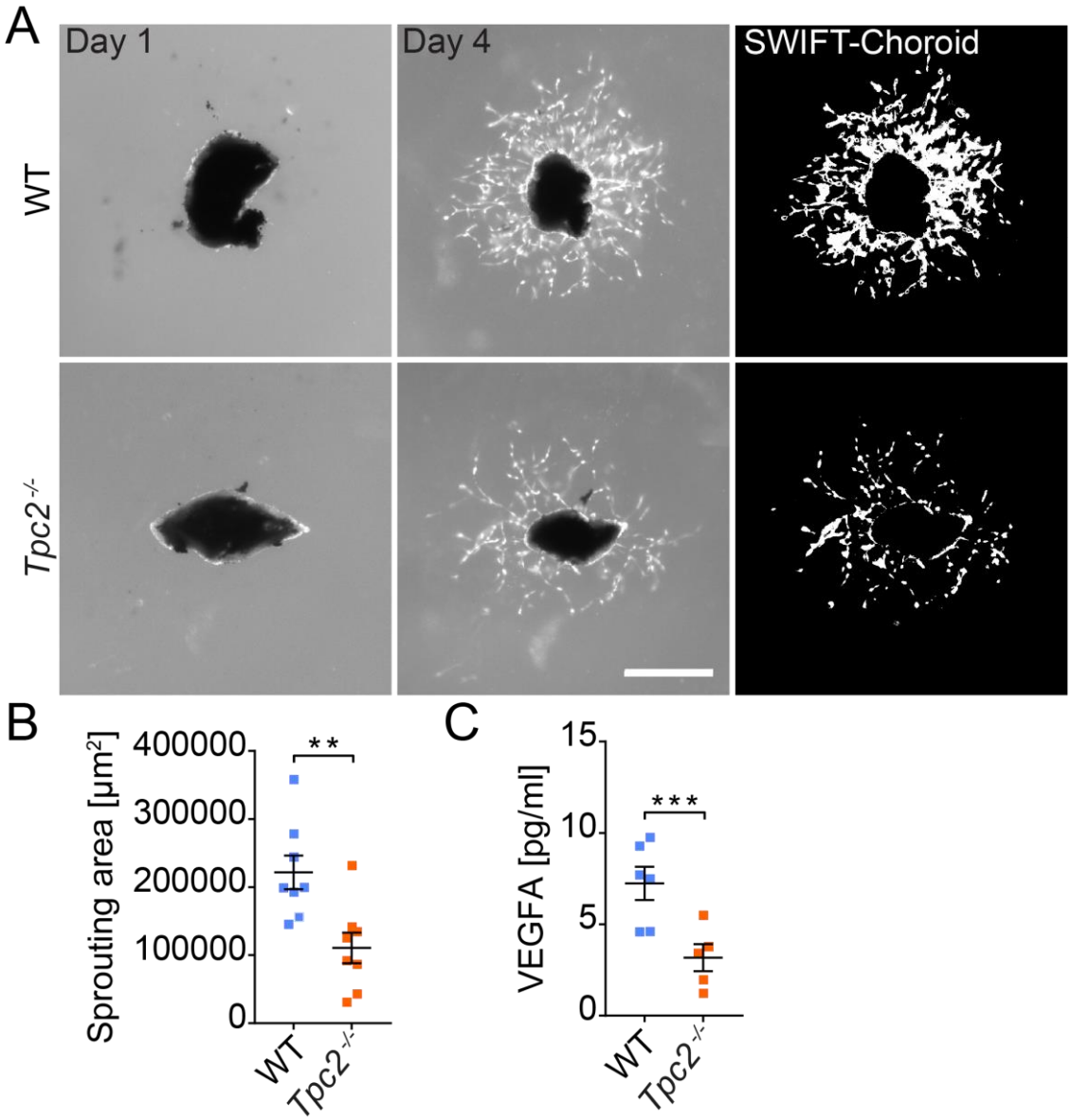

Figure 13 TPC2 deficiency inhibits choroidal sprouting and reduces ocular VEGFA levels after laser damage.

(A) Tissue was dissected from peripheral region of eyes of 21 to 25-day-old WT and *Tpc2*$^{-/-}$ mice, embedded in matrigel and cultured in medium. Microvascular sprouts were visualized using microscopy and processed and quantified with the SWIFT-Choroid macro in ImageJ64 software. Representative images were taken on day 1 and day 4 in culture (original and after SWIFT processing) are shown as indicated. Scale bar = 500 µm. (B) Quantification of the vascular sprouting area of WT versus *Tpc2*$^{-/-}$ mice. Each data point represents one RPE/choroid/sclera piece on day 4. Data are presented as mean ± SEM. n = 8 pieces/group. Student's *t*-test, **P*<0.05, ***P*<0.01, ****P*<0.001. (C) ELISA-based quantification of VEGFA levels in retinas from WT and *Tpc2*$^{-/-}$ mice on day 2 after laser photocoagulation. Each dot represents one eye. Data are presented as mean ± SEM, n = 6 eyes/group. Student's *t*-test, ***P*<0.01, ****P*<0.001.

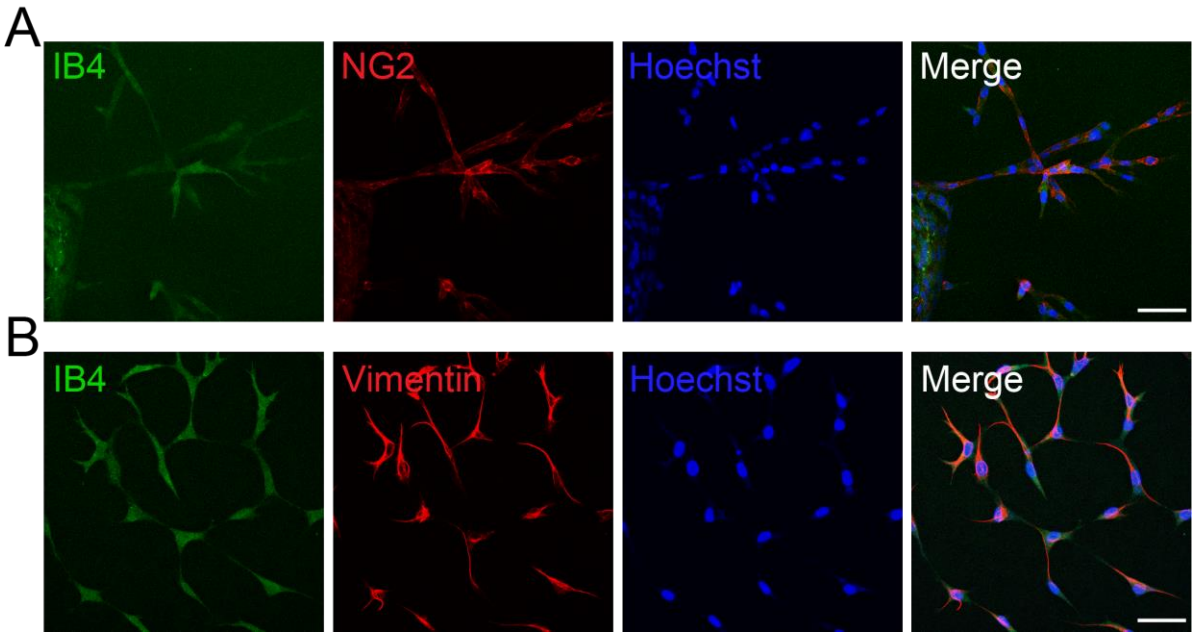

Figure 14 Representative immunostaining images of choroid sprouts.

(A) Choroid sprouts stained positively with endothelial cell marker isolectin B4 (IB4, green) and pericytes marker chondroitin sulfate proteoglycan NG2 (NG2, red). Scale bar = 50 µm. (B) Choroid sprouts stained positively with endothelial cell marker IB4 (green) and fibroblast marker vimentin (red). Scale bar = 50 µm.

Consistent with the *in vivo* findings, pharmacological blocking of TPC2 activity by either tetrandrine (Figures 15A and B) or Ned-19 (Figures 15C and D) also revealed a similar inhibitory effect as TPC2 knockout on choroidal sprouting. The sprouting area in tissues treated with 5 µM tetrandrine or 100 µM Ned-19 showed significantly less microvascular growth in comparison to the vehicle-treated tissues respectively (Figures 15B and D).

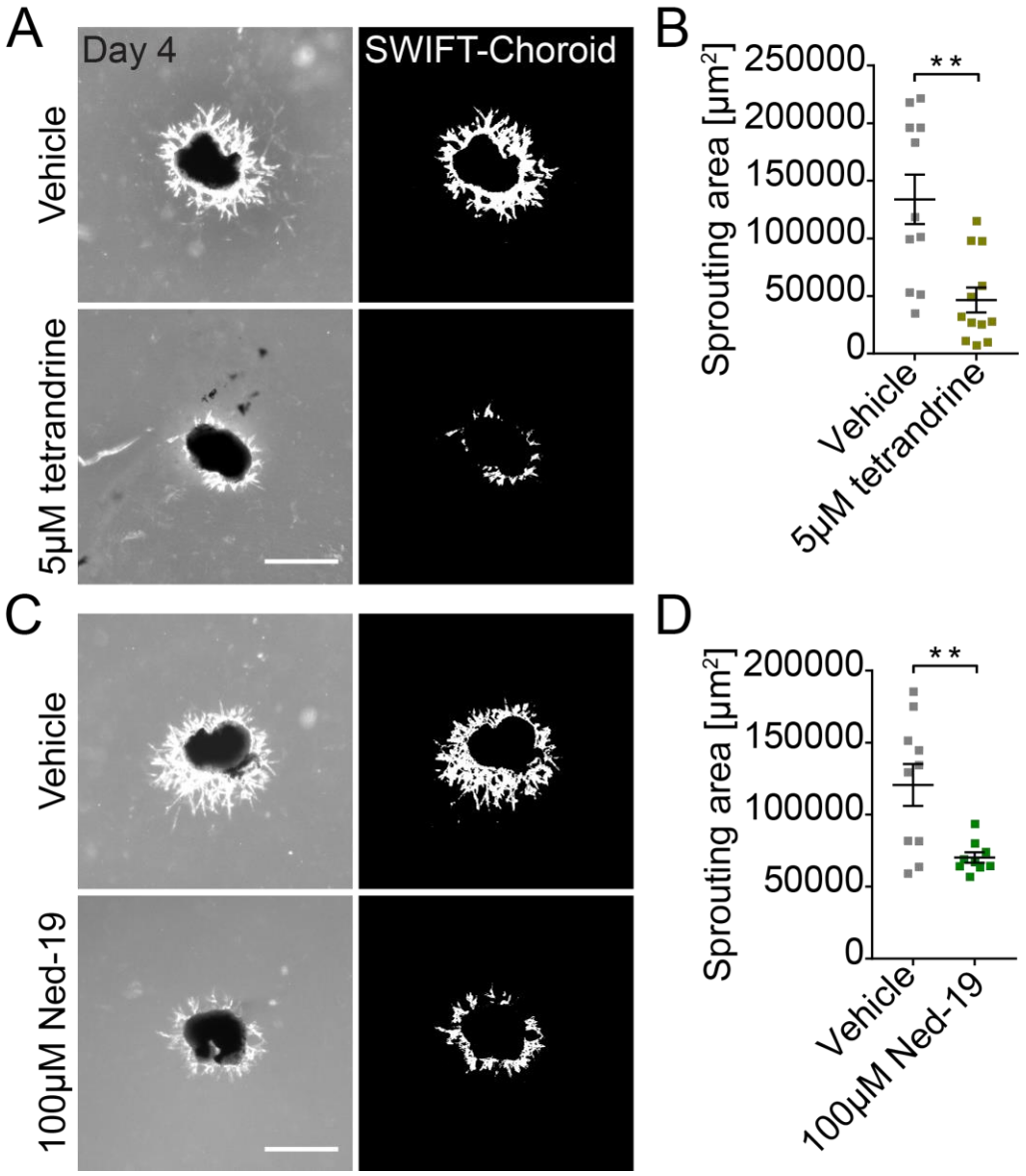

Figure 15 Pharmacological block of TPC2 reduces choroidal vascular growth.

(A, C) Representative images obtained at day 1 and day 4 and corresponding SWIFT-choroid images obtained from RPE/choroid/sclera pieces incubation in the presence of 5 µM tetrandrine (A), 100 µM Ned-19 (C) or respective vehicle controls. (B, D) Quantification of the vascular sprouting area of WT tissue in the absence or presence of 5 µM tetrandrine (B) or 100 µM Ned-19 (D) in the medium. Each data point represents one tissue on day 4. Data are presented as mean ± SEM. n = 9-12 pieces/group. Student's *t*-test, **P*<0.05, ***P*<0.01, ****P*<0.001.

4.3 TPC2 deficiency results in reduced infiltration of Iba1 positive cells and complement activation in CNV lesions.

To further validate the *in vivo* data, the neovascularization and inflammatory response after laser coagulation was examined using an *ex vivo* strategy. RPE/choroid/sclera flat mounts were dissected from the CNV-treated eyes and stained with the endothelial cell- and macrophage/microglia-marker IB4 and the macrophage/microglia-marker Iba1 (Figure 16A,

left panels). In comparison to WT mice 14 days following laser treatment, mice lacking TPC2 had significantly decreased vascular outgrowth indicated by the quantification of the IB4-positive area (Figure 16C; 20632 ± 1595 µm^2 in WT mice VS 8373 ± 709.4 µm^2 in *Tpc2*$^{-/-}$ mice). In WT mice, the IB4 labeling also revealed a substantial amount of macrophage/microglia-like cells surrounding the lesions, which were also immunopositive for Iba1. This co-immunostaining confirmed that these infiltrating cells were macrophages/microglia (Figure 16A). Quantification of the Iba1 positive area revealed that there was a profound decrease of infiltration of macrophages/microglia in *Tpc2*$^{-/-}$ mice, indicating a lower inflammatory response due to the absence of TPC2 (Figure 16D; 14716 ± 1276 µm^2 in WT mice VS 9741 ± 751 µm^2 in *Tpc2*$^{-/-}$ mice).

The complement system is the major immune effector during the development of neovascular AMD. Activation of the complement cascade terminates with the formation of the membrane attack complex (MAC) on the surface of cells, which is known as a key component in the pathology of AMD. In particular, MAC could trigger downstream activation of the Nod-like receptor protein 3 (NLRP3) inflammasome which is also considered a major factor in the inflammatory reaction of AMD [137]. Flat mounts of CNV complex were immunostained with C5b-9. Indeed, a substantial deposition of C5b-9 was observed in the CNV lesion site of WT mice (Figure 16B, upper panel). By contrast, the deposition of C5b-9 was dramatically decreased in the laser lesions from *Tpc2*$^{-/-}$ mice (Figure 16B lower panel and Figure 16E).

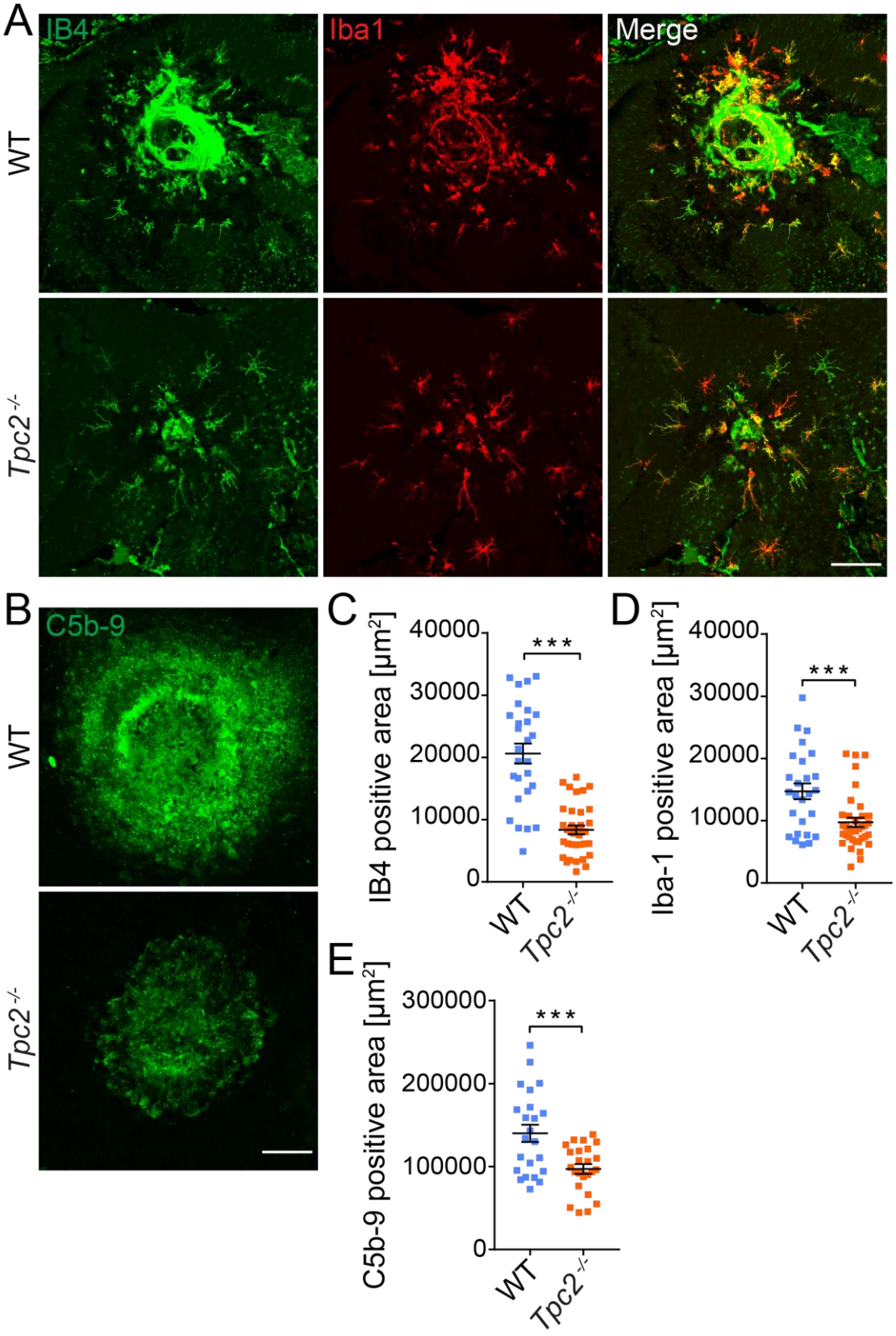

Figure 16 *Tpc2*$^{-/-}$ mice display reduced infiltration of inflammatory cells and lower C5b-9 levels in choroidal leakage areas.

(A) Representative images of lesion sites in RPE/choroid flat mounts prepared from WT and *Tpc2*$^{-/-}$ mice 14 days after laser coagulation. Whole mounts were double immunostained with the endothelial cell marker isolectin B4 (IB4, green) and the microglia/macrophage marker Iba1 (red). Scale bar = 100 µm. (B) Representatives images of C5b- 9-stained (green) lesion area of WT and a *Tpc2*$^{-/-}$ mice. Scale bar = 75 µm. (C-E) Quantification of IB4 (C), Iba1 (D) and C5b-9 (E) stained area. Each dot represents one CNV lesion site. Data are presented as mean ± SEM. Student's *t*-test, ***P<0.001.

4.4 TPC2 expression and electrophysiological analysis of TPC2-mediated currents in macrophages and microglia.

The results shown above suggest that suppression of TPC2 function ameliorates the inflammatory response and the extent of neovascularization in the mouse CNV model. In order to understand this phenotype, it is important to determine the cell type in which the presence or absence of TPC2 impacts neovascularization after injury. To this end, primary cultures of various cell types were established by isolating RPE, peritoneal macrophages, bone marrow and microglia from WT mice. Figure 17A shows representative images of these cell types. Acutely isolated RPE cells showing the characteristic pigmentation in culture. Peritoneal macrophages and BMDMs were immunostained with macrophage marker CD11b to ensure cell purity and identity (Figures 17B and C). Brain microglia were positively stained with macrophage/microglia marker Iba1 (Figure 17D). The established retinal microglia culture showed high purity of microglia despite some Otx2+ retinal neurons (Figure 17E). Primary cells isolated from WT and *Tpc2*$^{-/-}$ mice showed no differences in morphology. qRT-PCR analyses revealed a detectable TPC2 gene expression in all cultured cell types. The levels of TCP2 transcripts were significantly higher in brain and retinal microglia compared to RPE cells, peritoneal and bone marrow-derived macrophages (BMDM) (Figure 18).

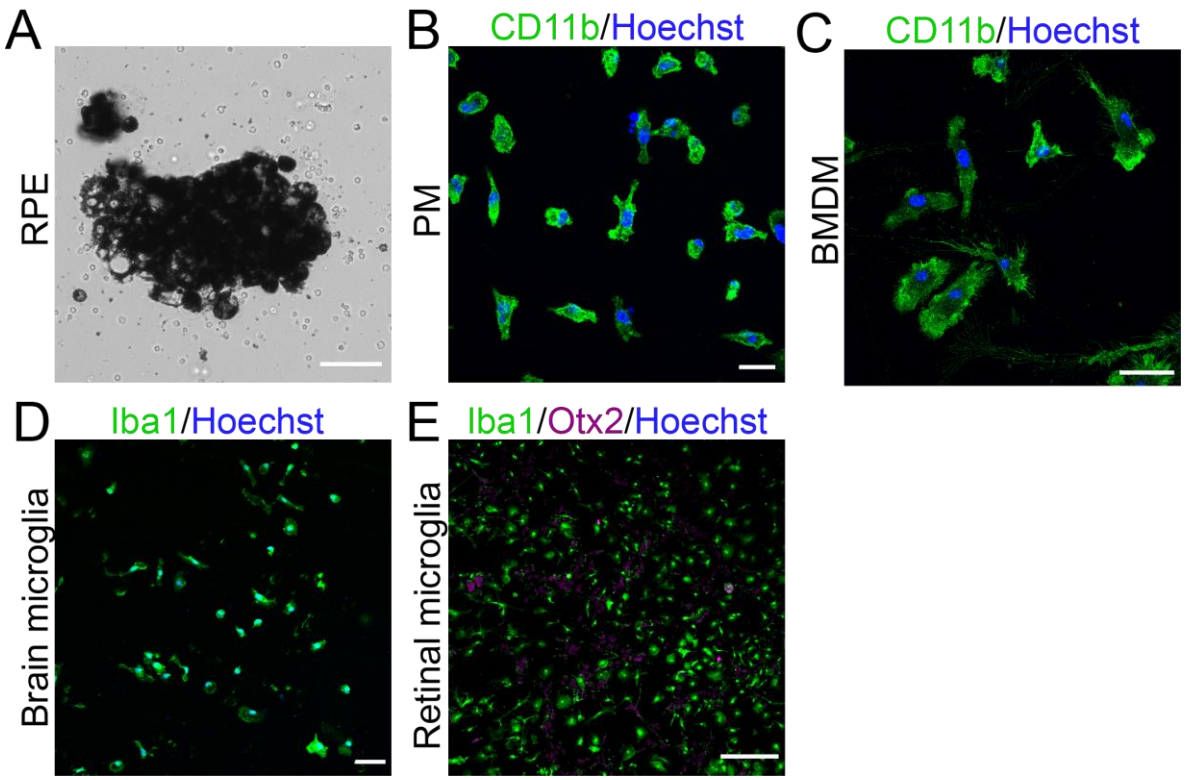

Figure 17 Representative images of primary RPE, peritoneal macrophage, BMDM and microglia culture.

(A) Bright-field images of primary RPE cells isolated from WT mice at 2 days in culture. Scale bar = 50 µm. (B, C) Primary peritoneal macrophages (PM) in (B) and bone marrow-derived macrophages (C) isolated from WT mice were identified using immunocytochemistry with macrophage marker CD11b (green). Scale bar in (B) = 20 µm. Scale bar in (C) = 30 µm. (D) Primary brain microglia were immunostained with microglia/macrophage marker Iba1 (green). Scale bar = 50 µm. (E) Primary retinal microglia were immunostained with Iba1 and retinal neuron marker Otx2. Scale bar = 200 µm.

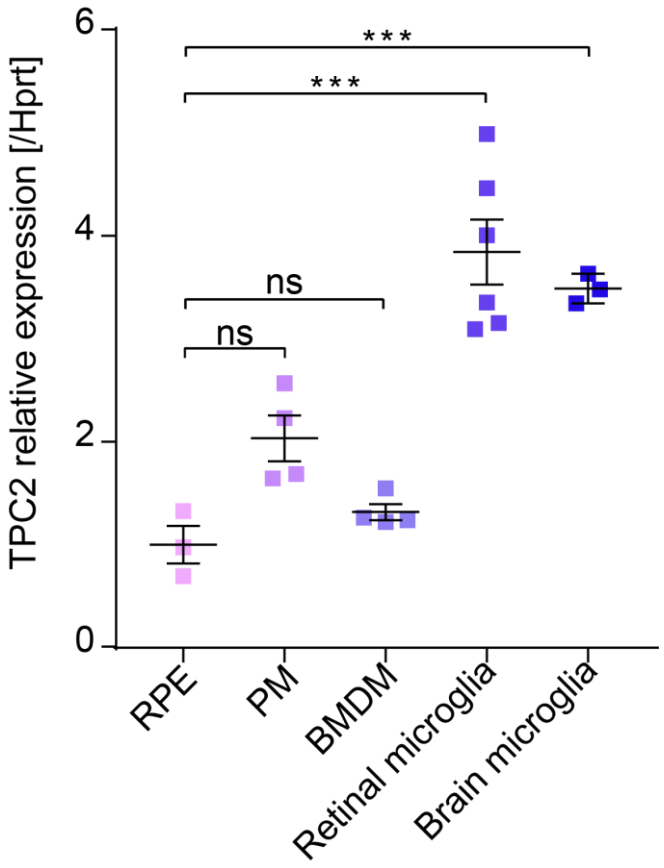

Figure 18 TPC2 mRNA expression in RPE, macrophages and microglia.

qRT-PCR analysis of TPC2 expression in cultivated murine retinal pigmented epithelium (RPE), peritoneal macrophages (PM), bone marrow-derived macrophages (BMDM), and brain and retinal microglia. Relative TPC2 mRNA expression was normalized to hypoxanthine phosphoribosyltransferase (Hprt) mRNA expression. TPC2 mRNA expression level in RPE cells was set to 1. Three to six independent experiments were performed in duplicate. Data are presented as mean ± SEM. One-way ANOVA followed by Tukey's multiple comparisons test was used, ****P*<0.001, ns, no significant difference.

The TPC2 gene expression pattern in different cell types was further corroborated using endolysosomal patch-clamp recordings, which tested TPC2 channel activity in these cells. To specifically activate voltage-independent TPC2-like currents, a low concentration of $PI(3,5)P_2$ (1 µM) was used in the presence of Na^+ and Ca^{2+} as the major permeant ions [121, 138]. In vacuolin-enlarged endolysosomes of WT BMDMs and peritoneal macrophages, $PI(3,5)P_2$ elicited a significant large TPC2-like current compared to the basal condition (Figures 19A, C, E, and F). In contrast, no activation was found in cells lacking TPC2 (Figures 19B, D, E, and F). Similarly, an increased current evoked by $PI(3,5)P_2$ was also present in WT brain microglia (Figures 20A and D), but was undetectable in *Tpc2*$^{-/-}$ brain microglia (Figures 20B and D).In WT retinal microglia, TPC2-like current was also detectable (Figures 20C and E).

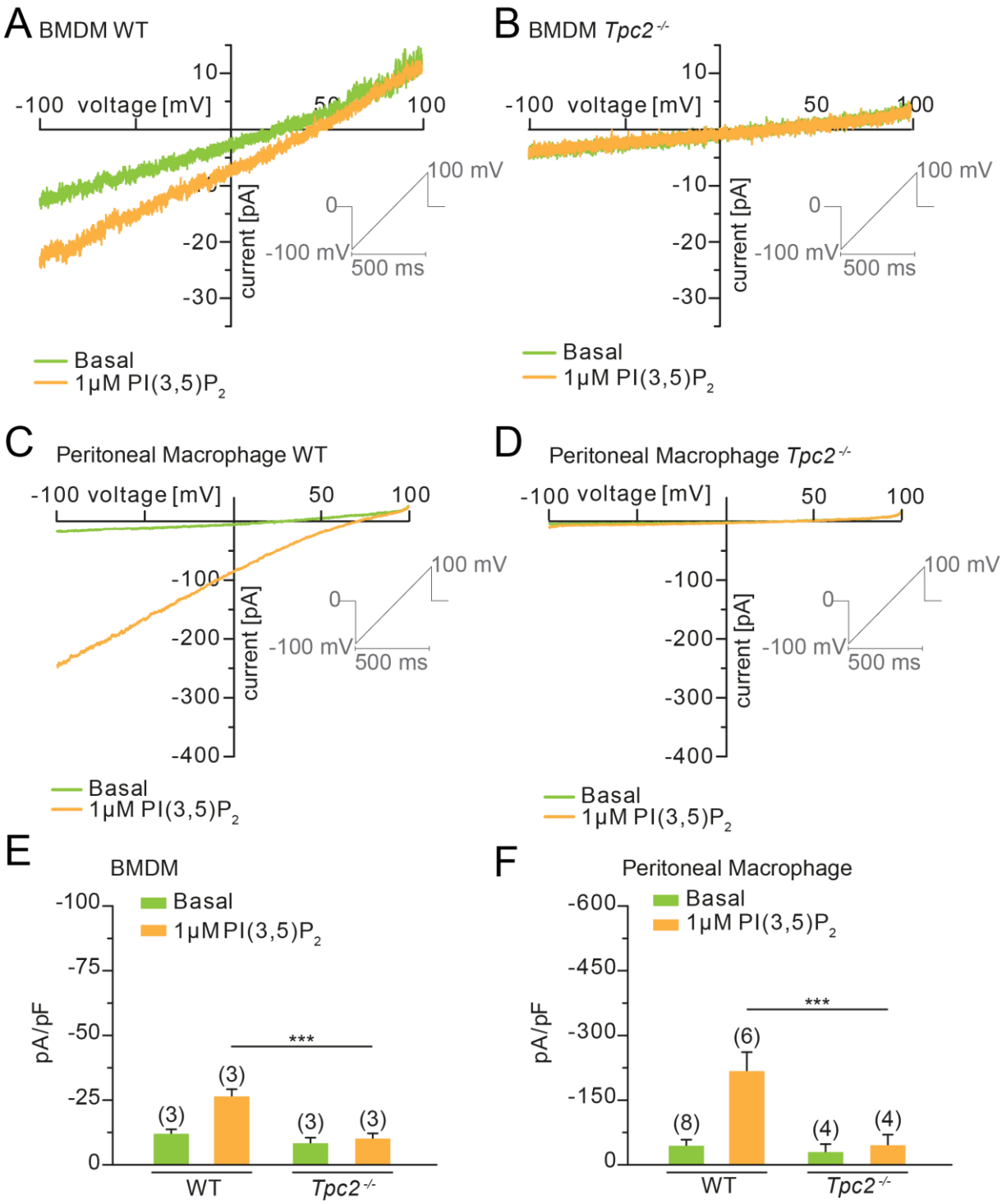

Figure 19 Endolysosomal patch-clamp analysis of TPC2-like current in macrophages.

(A-D) Representative current-voltage relationships recorded from vacuolin-enlarged endolysosomal vesicles isolated from cultured WT (A) and *Tpc2*$^{-/-}$ (B) BMDM or WT (C) and *Tpc2*$^{-/-}$ (D) PM. Currents were obtained before and after the application of 1 µM phosphatidylinositol 3,5-bisphosphate ($PI(3,5)P_2$). (E, F) Statistical analysis of current densities recorded at −100 mV for currents from BMDMD (E) and currents obtained under identical conditions from PM (F). Data are presented as mean ± SEM. To test for statistical significance two-way ANOVA was applied, ***P<0.001.

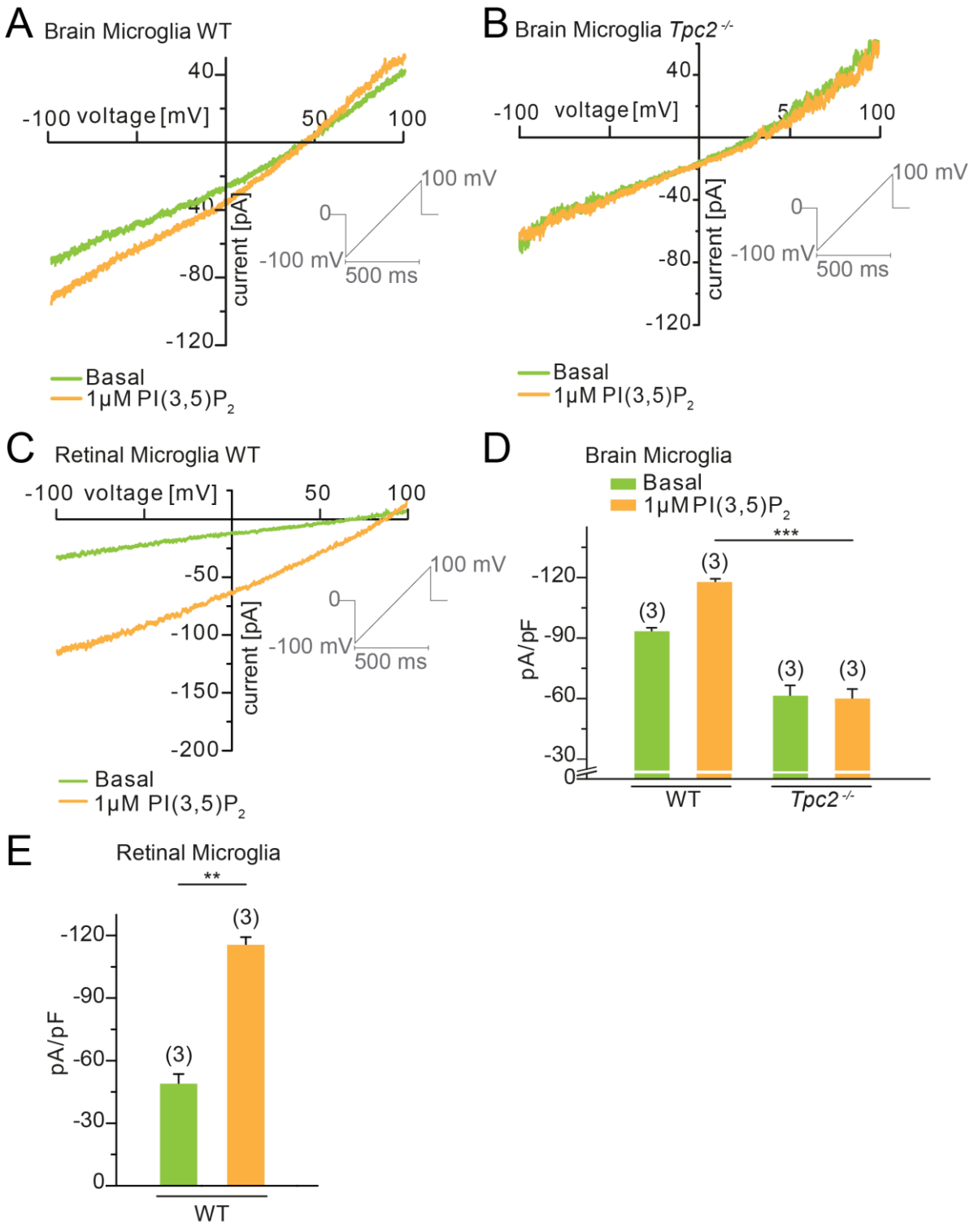

Figure 20 Endolysosomal patch-clamp analysis of TPC2-like current in microglia.

(A-C) Representative current-voltage relationships recorded from vacuolin-enlarged endolysosomal vesicles isolated from cultured WT (A) and *Tpc2*$^{-/-}$ (B) brain microglia or WT (C) retinal microglia. Currents were obtained before and after the application of 1 µM phosphatidylinositol 3,5-bisphosphate ($PI(3,5)P_2$). (D, E) Statistical analysis of current densities recorded at −100 mV for currents from brain microglia (D) and currents obtained under identical conditions from retinal microglia (E). Data are presented as mean ± SEM. To test for statistical significance two-way ANOVA or Student's *t*-test was applied, ***P*<0.01, ****P*<0.001.

4.5 Increased expression of TPC2 in M1 and M2 polarized macrophages.

After the functional characterization of TPC2 in immune cells, an open question was how the activity of this channel could be linked to the inflammatory response observed in the CNV model. Infiltrating immune cells, like macrophages, in CNV lesions show high plasticity and diversity in response to tissue signals. They can be polarized into classical proinflammatory (M1) and alternative anti-inflammatory (M2) macrophages, both of which are found in AMD eyes [56]. Therefore, it should be determined whether TPC2 plays a role in macrophage polarization. To address this question, polarized M1 and M2 BMDMs were established by stimulating cultured cells with LPS and IFN-γ or IL-4, respectively. Compared to BMDM without any stimulation (M0), M1 cells exhibited a rounded shape while M2 cells changed their morphology into an elongated spindle-like shape (Figure 21A, upper row). Deletion of TPC2 did not affect cell morphology (Figure 21A, lower row). To further confirm the macrophage polarization state, qRT-PCR analysis was performed to assess the expression of M1 (CD86, iNOS, IL-12 p40, and TNF-α) and M2 markers (Arg-1, CD206, Fizz1, and YM-1) in BMDMs exposed to LPS/IFN-γ or IL-4 stimuli after 24 h of incubation. As shown in Figures 21C-F, macrophages stimulated with LPS/IFN-γ expressed high mRNA levels of CD86, iNOS, IL-12 p40, and TNF-α. By contrast, cells activated with IL-4 expressed high mRNA levels of Arg-1, CD206, Fizz1, and YM-1 (Figures 21G-J). These results confirmed the cell identities and indicated that BMDMs could be sufficiently polarized into M1 or M2 macrophages using the chosen stimulation protocols with LPS/IFN-γ or IL-4. The expression of these M1 and M2 markers was comparable in cells obtained from *Tpc2*$^{-/-}$ or WT polarized macrophages, suggesting that deletion of TPC2 does not affect the polarization efficiency nor alters the mRNA expression of these markers (Figures 21C-J). Of note, a significant increase of TPC2 mRNA expression was detected in WT cells stimulated with LPS/IFN-γ or IL-4 for 24 h (Figure 21B), indicating TPC2 is directly associated with the polarization of macrophages.

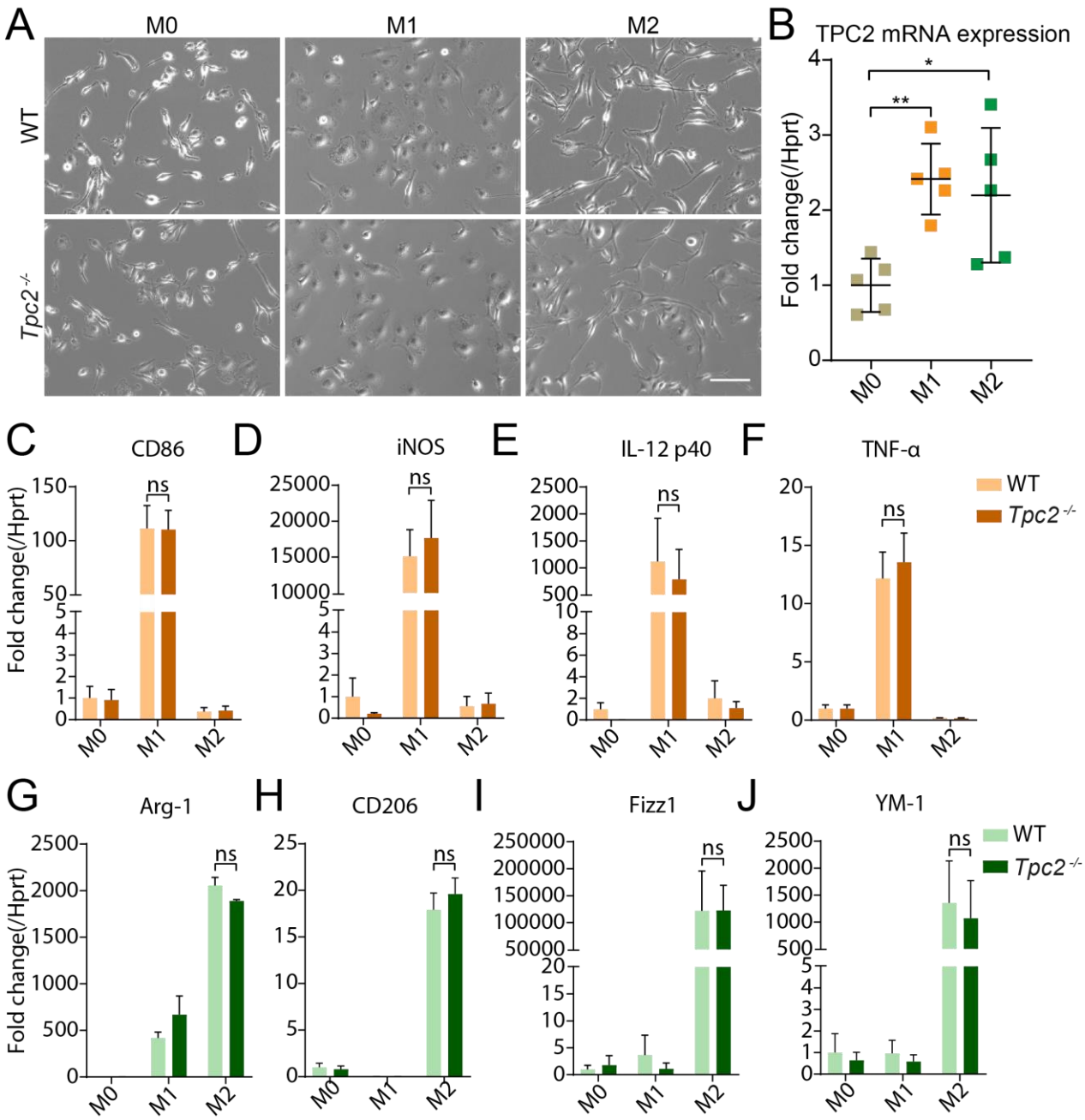

Figure 21 Identification of M1 and M2 polarized macrophages and TPC2 expression in polarized macrophages.

BMDMs were treated for 24 h with 100 ng/ml LPS and 20 ng/ml IFN-γ to induce M1 polarization or 20 ng/ml IL-4 to induce M2 polarization. (A) Representative images of M0, M1, and M2 macrophages were acquired with EVOS M5000 phase-contrast microscope. (B) Relative TPC2 mRNA expression was normalized to hypoxanthine phosphoribosyltransferase (Hprt) mRNA expression. TPC2 mRNA expression level in M0 macrophages was set to 1. Five independent experiments were performed in duplicate. Data are presented as mean ± SEM. One-way ANOVA followed by Tukey's multiple comparisons test was used, **P*<0.05, ***P*<0.01. (C-J) qRT-PCR analysis was used to detect mRNA expression of M1 markers, CD86 (C), iNOS (D), IL-12 p40 (E) and TNF-α (F), and M2 markers, Arg-1 (G), CD206 (H), Fizz1 (I) and YM-1 (J). Hprt was served as the housekeeping gene. mRNA expression of each marker in WT M0 cells was set to 1 respectively. Three independent experiments were performed in duplicate. Data are presented as mean ± SEM. Two-way ANOVA, ns, no significant difference.

4.6 TPC2 has no effect on the migration ability of polarized macrophages.

Since the expression of TPC2 was upregulated during macrophage polarization and TPC2 was shown to regulate cancer cell migration in a recent study from our group [126], it was hypothesized that TPC2 may also be involved in the migration of polarized macrophages. To explore this, a transwell system was utilized to determine the migratory behavior of WT and *Tpc2*$^{-/-}$ polarized macrophages. M0, M1, and M2 polarized macrophages from WT and *Tpc2*$^{-/-}$ mice were seeded on an 8 µM pore membrane, and medium containing M-CSF was added in the lower compartment as chemoattractant. In comparison to M0 macrophages that have an intermediated migration capability, M1 cells exhibited less migration, while M2 cells showed enhanced migration towards M-CSF (Figure 22A, upper panel). Interestingly, macrophages lacking TPC2 revealed no differences in their migration pattern compared with the corresponding WT M0, M1, or M2 macrophages (Figure 22A, lower panel, and B).

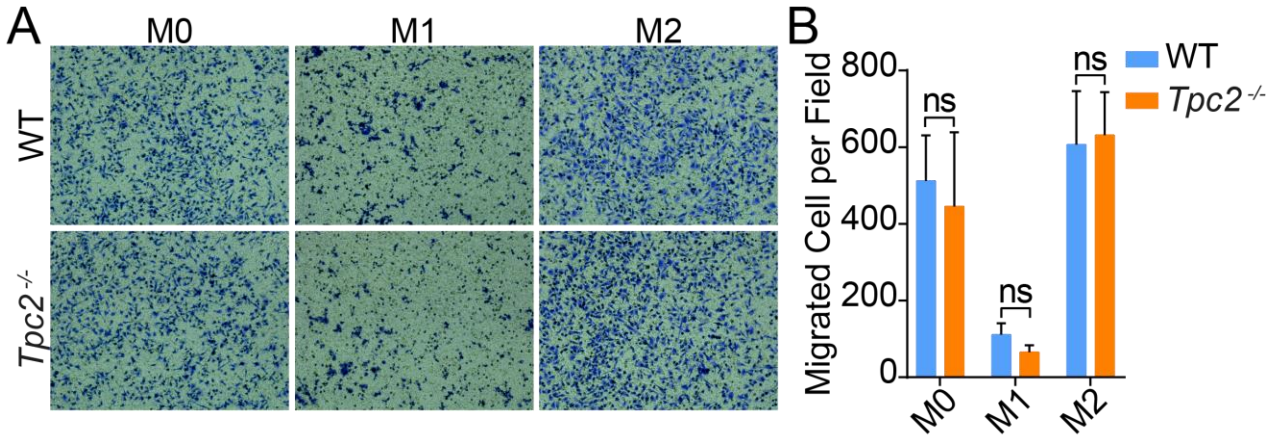

Figure 22 Transwell assay for migration of polarized macrophages.

BMDMs were differentiated and polarized with or without LPS/IFN-γ or IL-4 for 48 h then seeded in the 8 µM pore membrane of transwell. Medium supplemented with 40 ng/ml M-CSF was loaded in the lower compartment as a chemoattractant. Cells were migrated for 6 h through membrane, followed by fixation and visualization with crystal violet. (A) Representative images of migrated M0, M1 and M2 macrophages from WT and *Tpc2*$^{-/-}$ mice. (B) Quantification of migrated cells towards M-CSF per field. Shown are mean values ± SEM of 3 independent experiments. Two-way ANOVA, ns, no significant difference.

4.7 Deletion of TPC2 impairs IL-1β secretion from macrophages and microglia.

A battery of proinflammatory and anti-inflammatory cytokines is produced and secreted by macrophages and microglia in response to tissue injury. Among these cytokines, IL-1β is a major proinflammatory factor that has been associated with the pathology of neovascular AMD [139]. IL-1β is synthesized in microglia and macrophages as a biologically inactive precursor protein, pro-IL-1β, upon stimulation from exogenous and endogenous pathogen- and damage-associated molecular patterns (PAMPs and DAMPs) [139]. Following activation and assembly

of the NLRP3 inflammasome, pro-IL-1β is cleaved by the proinflammatory protease caspase-1 to the mature form of IL-1β that is subsequently secreted into the extracellular space through unconventional secretory pathways, including secretory lysosomes [140]. To assess the release of proinflammatory cytokines, in the absence of TPC2, global IL-1β levels were quantified by ELISA in retinal homogenates from WT and *Tpc2*$^{-/-}$ eyes 24 h after laser photocoagulation. Interestingly, there was analysis showed lower levels of IL-1β in the *Tpc2*$^{-/-}$ compared to the WT retina (Figure 23) (8.066 ± 0.7616 pg/ml in WT retina; 6.11 ± 0.2096 pg/ml in *Tpc2*$^{-/-}$ retina, n = 6 eyes/group).

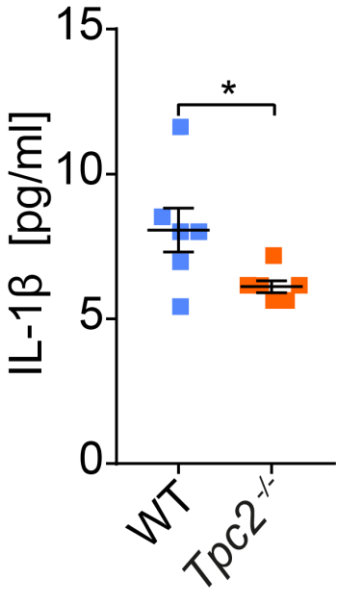

Figure 23 TPC2 deficiency reduces ocular IL-1β levels after laser photocoagulation.

Quantification of interleukin-1β (IL-1β). Retinas were dissected and homogenized from WT and *Tpc2*$^{-/-}$ mice on day 1 after laser photocoagulation. IL-1β level in the retina was determined by ELISA. A reduced IL-1β concentration was found in *Tpc2*$^{-/-}$ retinas compared with WT control retinas. Each dot represents one eye. Data are presented as mean ± SEM, n = 6 eyes/group. Student's *t*-test, **P*<0.05.

To further investigate the correlation between microglia and proinflammatory cytokine release in the absence of TPC2, retinal cross-sections were immunolabelled for IL-1β and Iba1 after laser photocoagulation injury. Irrespective of the genotype, only a few Iba1+ cells were present in the inner plexiform layer (IPL) and outer plexiform layer (OPL), and almost no IL-1β signal was observed in non-lesioned parts of the retina (Figure 24A). By contrast, within the lesion area of the WT retina, a high number of Iba1+ cells and massive IL-1β signal were observed in the subretinal space (Figure 24B, upper row). While the number of Iba1+ cells and the overall amount of IL-1β signal in the subretinal area of *Tpc2*$^{-/-}$ retina were significantly lower (Figure 24B, C and D).

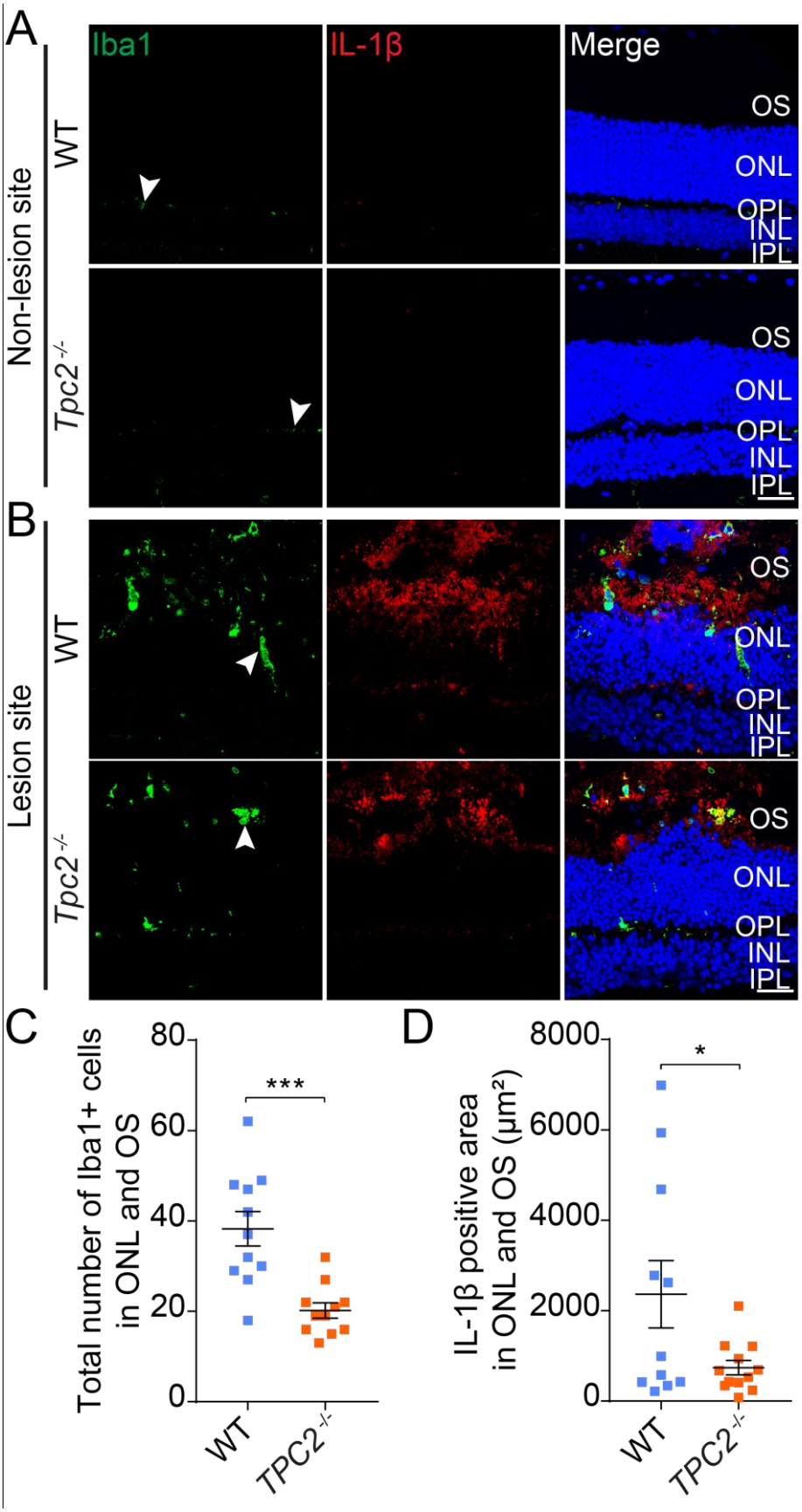

Figure 24 *Tpc2*$^{-/-}$ mice display reduced overall amounts of IL-1β in CNV areas.

Immunolabelled cross-sections of retinas from WT and *Tpc2*$^{-/-}$ mice on day 1 after laser treatment. Sections were co-stained for Iba1 (left panels) and IL-1β (middle panels). The right panels show the overlay of the two respective images. (A) Representative images from the non-damaged area of WT and *Tpc2*$^{-/-}$ mice. Only a few quiescent Iba1+ cells (green, marked by arrowhead) were present in the inner plexiform (IPL) and outer plexiform layer (OPL) of WT and *Tpc2*$^{-/-}$ mice. IL-1β (red) was undetectable in both genotypes. Scale bar = 30 µm. (B) Representative images from CNV lesion area. By contrast, Iba1+ cells infiltrated the outer nuclear layer (ONL) and outer segments (OS) (marked by white arrows). Scale bar = 30 µm. INL, inner nuclear layer. (C, D) Quantification of the total number of Iba1+ cells (C) or IL-1β positive areas (D) in ONL and OS of lesion sites from WT and *Tpc2*$^{-/-}$ retina. Each dot represents one CNV lesion site. n = 10-12 lesions/group. Data are presented as mean ± SEM. 2-tailed Student's *t*-test, **P*<0.05, ****P*<0.001.

To further confirm this finding, IL-1β expression and secretion were analyzed in cultured BMDMs from WT and *Tpc2*$^{-/-}$ mice. Priming of BMDMs with lipopolysaccharides (LPS) led to a dramatic upregulation of pro-IL-1β transcript (Figure 25C) and protein (Figures 25A and B) level in WT BMDMs. This upregulation was also present in *Tpc2*$^{-/-}$ cells (Figures 25A-C).

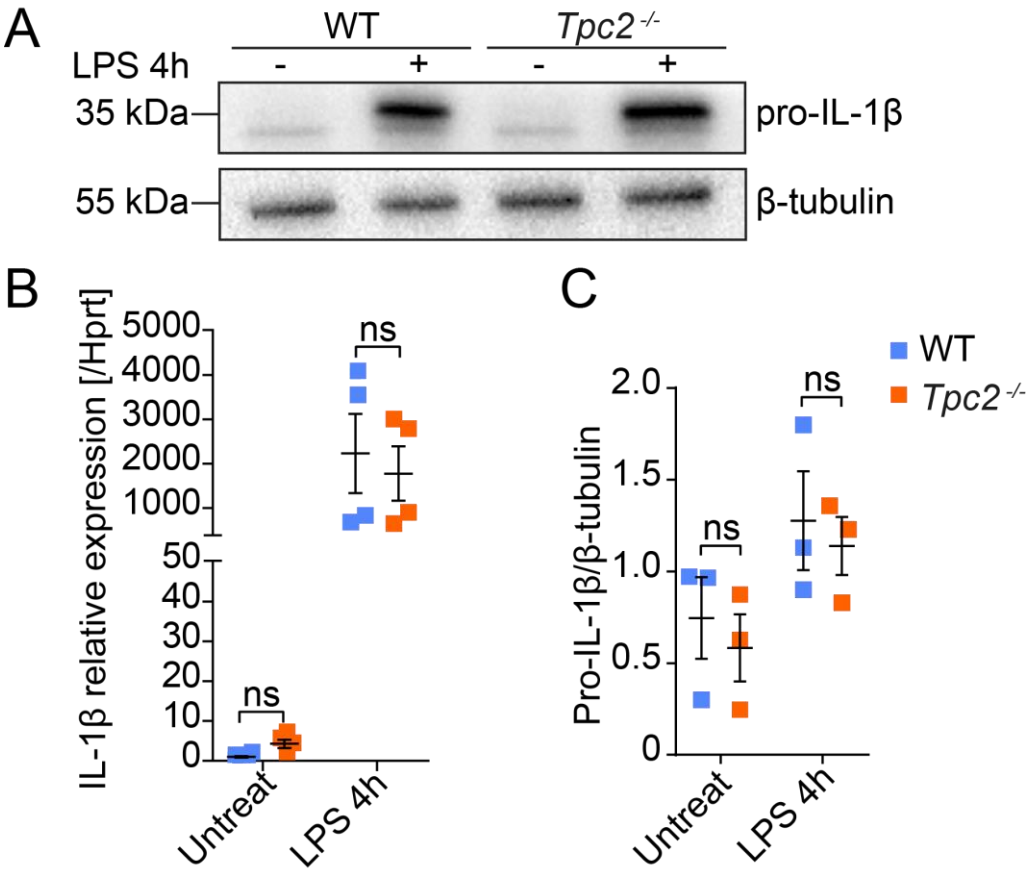

Figure 25 TPC2 is not crucial for IL-1β expression in macrophages.

(A) Western blot analysis of cell lysates from cultured BMDMs of WT and *Tpc2*$^{-/-}$ mice. The blot was probed for IL-1β and β-tubulin as a loading control. In cells analyzed in lanes 2 and 4, lipopolysaccharides (LPS) were added at 1 µg/ml to the medium 4 h prior to lysis to induce pro-IL-1β expression. (B) Densitometric quantification of pro-IL-1β expression. Three independent experiments were performed. Data are presented as mean ± SEM. Two-way ANOVA, ns, no significant difference. (C) qRT-PCR quantification of pro-IL-1β mRNA in WT and *Tpc2*$^{-/-}$ BMDMs

under basal condition and after stimulation with 1 µg/ml LPS for 4 h. pro-IL-1β mRNA in untreated WT BMDM was set to 1. Four independent experiments were performed in duplicate. Data are presented as mean ± SEM. Two-way ANOVA, ns, no significant difference.

In order to quantify the amount of secreted IL-1β, LPS-primed BMDMs were first treated with ATP [91] to induce cleavage of pro-IL-1β and secretion of IL-1β. As shown in Figure 26, exposure to LPS alone for 4 h failed to drive the secretion of IL-1β in macrophages. By contrast, the combined LPS and ATP treatment triggered a considerable secretion of mature IL-1β from LPS-primed WT macrophages in a time-dependent manner. Of note, the ELISA detected decreased levels of IL-1β in cell culture supernatants from *Tpc2*$^{-/-}$ macrophages suggesting an impaired secretion of IL-1β in the absence of TPC2 (Figure 26).

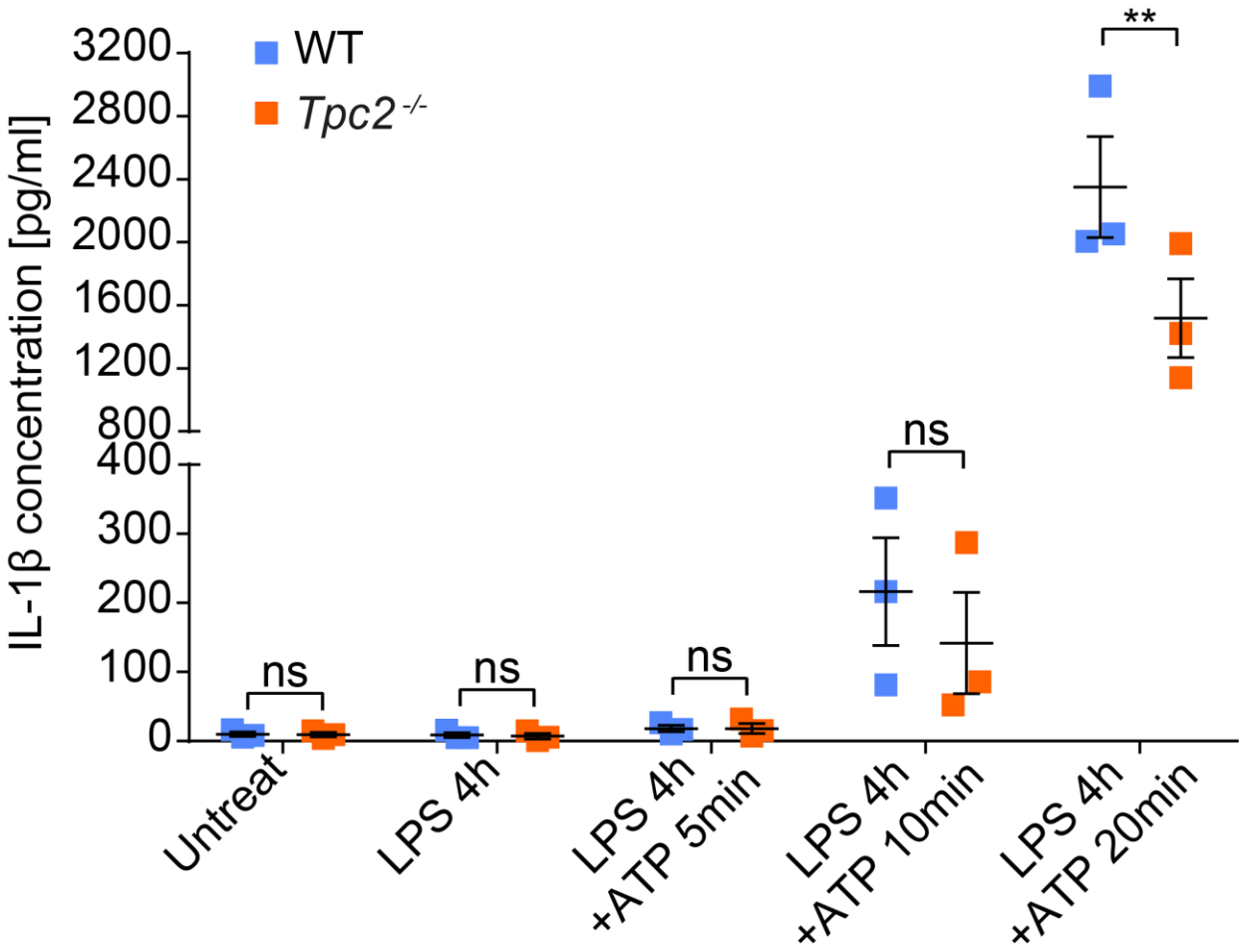

Figure 26 TPC2 is required for IL-1β secretion in macrophages.

Determination of secreted IL-1β. WT and *Tpc2*$^{-/-}$ BMDMs were pretreated with or without 1 µg/ml LPS for 4 h to induce IL-1β expression, followed by stimulation with 5 mM adenosine triphosphate (ATP) for 5, 10, and 20 min to promote IL-1β maturation and secretion. Extracellular medium was collected and processed for ELISA analysis. Data are presented as mean ± SEM. Two-way ANOVA, **P*<0.05, ***P*<0.01, ****P*<0.001, ns, no significant difference.

These findings suggest that TPC2 may not be essential for priming BMDMs and IL-1β expression, but is involved in the release of IL-1β. If this is true, one would expect that once produced, IL-1β accumulates in intracellular compartments of *Tpc2*$^{-/-}$ cells. To verify this hypothesis, retina sections were double immunostained with Iba1 and another IL-1β antibody which was more specific to detect cytosol IL-1β. As shown in Figure 27A, *Tpc2*$^{-/-}$ Iba1+ cells displayed a strong IL-1β co-staining, suggesting an intracellular accumulation of IL-1β in *Tpc2*$^{-/-}$ cells. Fluorescence intensity quantification further showed an increase of IL-1β signal in *Tpc2*$^{-/-}$ Iba1+ cells in comparison to WT Iba-1+ cells (Figure 27B).

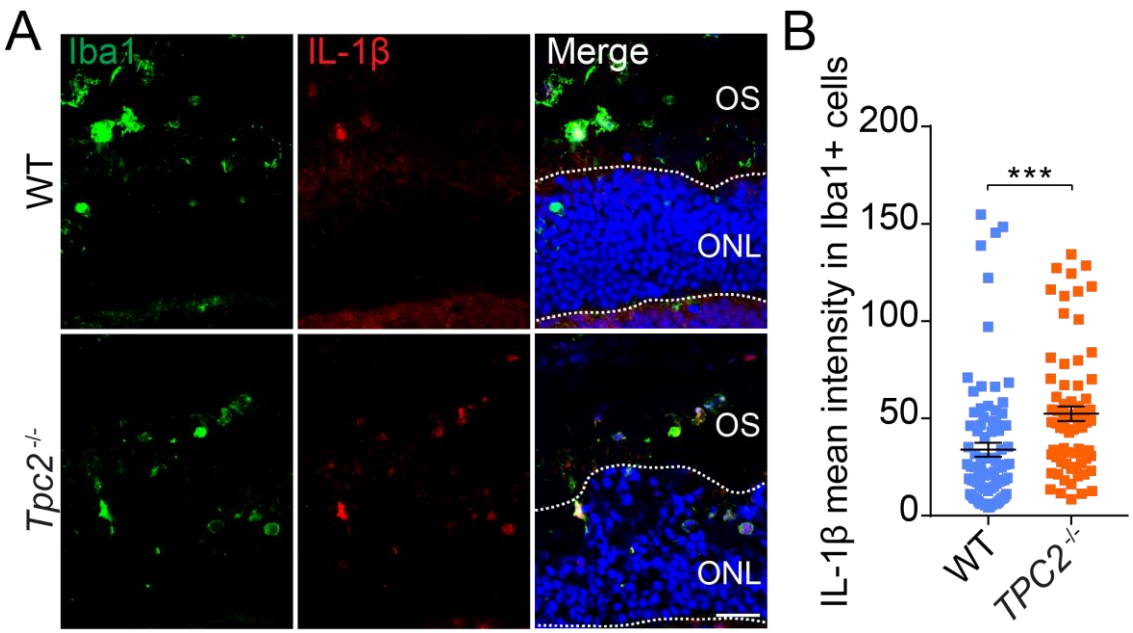

Figure 27 *Tpc2*$^{-/-}$ mice display increased amounts of IL-1β in Iba1 positive cells

(A) Immunolabelled cross-sections of retinas from WT and *Tpc2*$^{-/-}$ mice on day 1 after laser treatment. Sections were co-stained for Iba1 (left panels) and IL-1β (middle panels). The right panels show overlay of the two respective images. Scale bar = 20 µm. ONL, outer nuclear layer; OS, outer segment. (C) Quantification of IL-1β mean intensity in Iba1+ cells from WT and *Tpc2*$^{-/-}$ retinas. Each dot represents one cell. n = 72-86 cells/group. Data are presented as mean ± SEM. 2-tailed Student's *t*-test, ***P<0.001.

Moreover, isolated *Tpc2*$^{-/-}$ BMDMs challenged with LPS/ATP revealed a strong intracellular IL-1β signal that mainly co-localized with the lysosomal marker LAMP-1 (Figure 28A, second row), indicating IL-1β is contained in these LAMP-1 positive organelles. Both the IL-1β and LAMP-1 signal were significantly weaker in WT cells (Figure 28A, first row). The mean fluorescence intensity of the staining in whole cytosol was quantified with ImageJ64 software. The quantification data showed an increase for *Tpc2*$^{-/-}$ cells (IL-1β: 63.27 ± 1.841; LAMP-1: 41.87 ± 1.595; n = 50) compared to WT cells of 51.17 ± 1.701 (n = 45) for IL-1β (Figure 28B) and of 35.3 ± 1.512 (n = 45) for LAMP-1 (Figure 28C). Increased intracellular accumulation of IL-1β in LAMP-1+ organelles was also observed in LPS/ATP-stimulated retinal microglia

derived from *Tpc2*$^{-/-}$ mice (Figure 29A). Again, the overall signal intensity for IL-1β (49.35 ± 3.282 vs 27.12 ± 1.581, *n* = 45), and LAMP-1 (69.82 ± 4.139 vs 36.23 ± 3.269, *n* = 46) was higher in *Tpc2*$^{-/-}$ than in WT cells (Figure 29B and C).

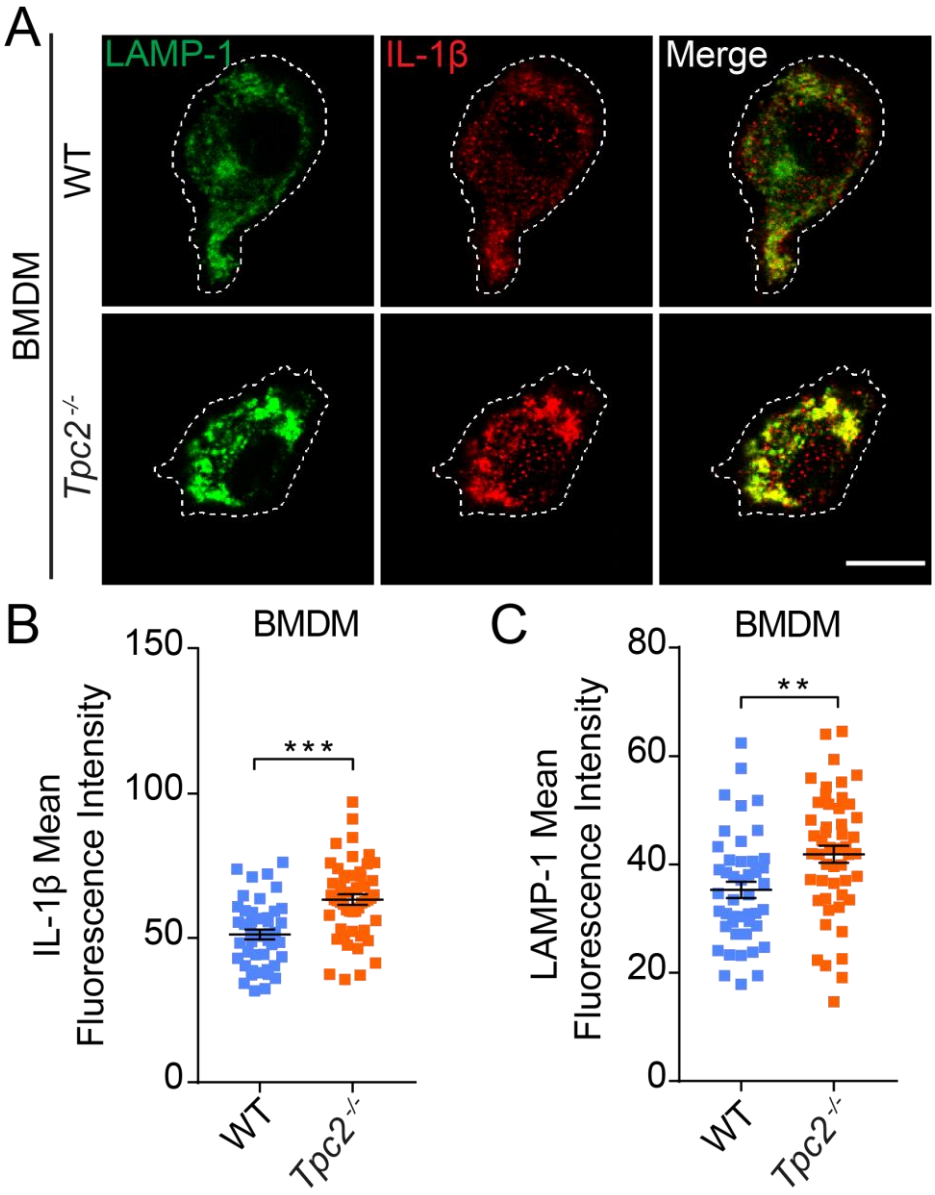

Figure 28 Deletion of TPC2 induces intracellular accumulation of IL-1β in macrophages.

(A) Detection of IL-1β in cultured BMDMs from WT and *Tpc2*$^{-/-}$ mice. Cells were pretreated with 1 µg/ml LPS for 4 h, followed by stimulation with 5 mM ATP for 20 min. Then cells were fixed and co-stained for the lysosomal marker protein LAMP-1 (green) and IL-1β (red). Scale bar = 10 µm. (B, C) Densitometric analysis of intracellular levels of IL-1β (B) and LAMP-1 (C) in BMDMs of WT and *Tpc2*$^{-/-}$ mice. Data are presented as mean ± SEM, n = 40 to 50 cells/group. 2-tailed Student's *t*-test, **P*<0.05, ***P*<0.01, ****P*<0.001.

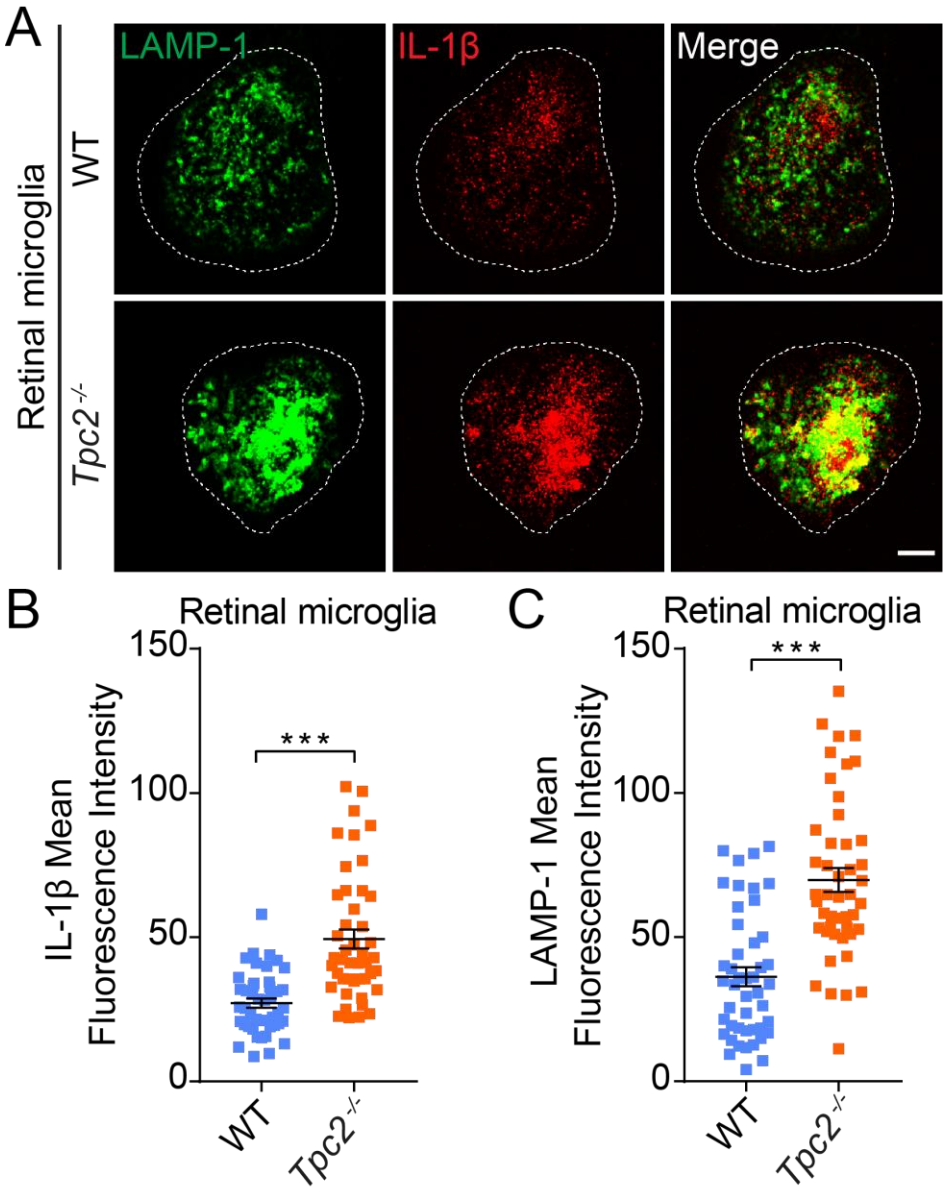

Figure 29 Deletion of TPC2 induces intracellular accumulation of IL-1β in retinal microglia.

(A) Detection of IL-1β in cultured retinal microglia from WT and *Tpc2*$^{-/-}$ mice. Cells were pretreated with 1 µg/ml LPS for 4 h, followed by stimulation with 5 mM ATP for 20 min. Then cells were fixed and co-stained for the lysosomal marker protein LAMP-1 (green) and IL-1β (red). Scale bar = 10 µm. (B, C) Densitometric analysis of intracellular levels of IL-1β (B) and LAMP-1 (C) in retinal microglia of WT and *Tpc2*$^{-/-}$ mice. Data are presented as mean ± SEM, n = 40 to 50 cells/group. 2-tailed Student's *t*-test, **P*<0.05, ***P*<0.01, ****P*<0.001.

5 Discussion

This study investigated the role of endolysosomal cation channel TPC1 and TPC2 in the context of choroidal neovascularization and retinal inflammation, two clinical hallmarks of neovascular AMD.

AMD is a complex multifactorial disease that results from the chronic interaction of various environmental and genetic risk factors. The establishment of suitable animal models to study human AMD is essential for elucidating the pathogenesis and testing potential therapies for this disease. Despite the obvious limitation that rodents lack a macula, rodent animal models are still very valuable in order to study the basic processes and genes involved in maintaining retinal integrity during the pathobiology of AMD. The mouse has several advantages for the study of human AMD. Its relatively short life span allows us to monitor the histological and functional changes in tissues during aging. Moreover, the ease of genetic manipulation and >90% homology of functional genes between human and mouse genomes has rendered mice the most popular animal model for studying the effects of gain- or loss-of-function genetic mutations. Considering the histological features of AMD, numerous mice models have been developed that exhibit either spontaneous or induced progression of AMD. Some transgenic mice, such as *Cfh*$^{-/-}$ mice, C3a and C5a receptor$^{-/-}$ mice, and C3 overexpression mice, have been generated to exhibit AMD features and used to examine the role of the complement system in AMD development [141]. Genetic deletion of chemokines and their receptors including CCL2/CCR2 and Cx3cr1 in mice have also been created to reproduce pathological aspects of AMD [52, 142]. Furthermore, impaired intrinsic anti-oxidant mechanisms or severe oxidative stress in mice could also develop many features of AMD. Other AMD models could also be established by mimicking the defective lipid/glucose metabolism in mice [141]. However, due to the high level of heterogeneity and complexity involved in the onset and progression of AMD, there is currently no single animal model that exhibits all the characteristics of this disease. In recent years, a laser-induced Bruch's membrane photocoagulation mouse model has been established and used extensively to study exudative AMD [135, 143]. In this model, the physical lesion in the Bruch's membrane induces blood vessel outgrowth from the choroid into the subretinal space and leads to strong inflammatory responses, which mimic the main pathological events of human neovascular AMD. Through systemic or local administration of new drugs, together with novel transgenic mouse technologies, this model offers the opportunity for us to identify potential therapeutic targets for AMD. Based on the laser-induced CNV model, this study revealed that mice in which TPC2 has been genetically deleted display significantly less neovascularization and immune activities in response to laser damage compared to WT mice.

Of note, intravitreal delivery of one of the established TPC channel inhibitors, tetrandrine or Ned-19, also reduced the extent of laser-induced choroidal neovascularization in WT mice. These findings suggest that the lack of TPC channel function, rather than developmental or long-term compensatory changes that might have resulted from the TPC2 knockout, is responsible for the protection from CNV. This effect seems to be specific for TPC2 since no obvious differences were observed between laser-treated *TPC1*$^{-/-}$ and WT mice. The different roles of TPC2 and its homolog TPC1 in the CNV model could be explained by the following reasons. TPC2 localization is more restricted to late endosomes and lysosomes, whereas TPC1 is predominantly distributed in early and recycling endosomes [144]. Their distinct subcellular localization suggest they have different biological and physiological properties. Indeed, Cang *et al.* demonstrated that TPC1, but not TPC2, formed a non-inactivating lysoNa$_v$-like voltage-gated channel [138]. They further reported that luminal alkalization could open TPC1 by shifting the channel's voltage dependence of activation toward hyperpolarization [138]. Regarding channel activation, Mg^{2+} has been identified as a novel regulator of TPC2, as both cytoplasmic and lysosomal Mg^{2+} could inhibit TPC2 current, whereas TPC1 activity was only slightly inhibited by Mg^{2+} [120]. It has been found that loss of each TPC isoform led to respective effects in endo-lysosomal trafficking. Cultured *Tpc1*$^{-/-}$ mouse embryonic fibroblast (MEFs) cells showed impaired cholera toxin trafficking, while the ligand-induced degradation of endogenous platelet-derived growth factor receptor β (PDGFβ) was delayed in *Tpc2*$^{-/-}$ MEFs [113]. In addition, the functions of the two channels could also change under distinct pathophysiological conditions. For instance, there is some evidence that inhibiting TPC1 activity (but not TPC2) decreases ER-endosome contact and disrupts late endosome and lysosomal morphology in primary cultured fibroblasts [145]. Nevertheless, Hockey *et al.* identified that pronounced lysosomal morphology defects could be reversed by inhibiting TPC2 (not TPC1) and associated regulators in fibroblasts from Parkinson's disease patients with the common LRRK2 G2019s mutation [129]. In sum, despite sharing certain similarities, TPC1 and TPC2 still have disparities regarding activation mechanisms and responses to cellular signals. Further investigation will be necessary to decipher the detailed role of TPC isoforms in physiological processes and related disorders.

In line with the *in vivo* findings, in which the absence of TPC2 lead to decreased neovascularization after laser damage, genetic deletion or pharmacological inhibition of TPC2 also impaired blood vessel formation in response to VEGFA and other growth factors in the *ex vivo* choroidal sprouting assay that is highly efficient and pertinent to angiogenic research, especially for wet AMD study. These results also agree with a previous study by Favia *et al.* [133], which showed that TPC2-dependent Ca^{2+} release was involved in VEGF/VEGFR2-induced angiogenic responses in endothelial cells. The VEGF family, in particular VEGFA, are

crucial regulators of blood-vessel formation during physiological or pathological processes, mainly through the interplay with its receptor VEGFR2 [146]. Phosphorylated VEGFR2 upon binding VEGF results in the activation of downstream signaling cascades and increases the intracellular calcium concentration that leads to endothelial cell proliferation [147]. Favia *et al.* identified that pharmacological blockage of NAADP, the potent Ca^{2+} mobilizing messenger, using antagonist Ned-19 or genetic deletion of TPC2 could abolish VEGF-induced Ca^{2+} release and angiogenesis [133]. In this study, data from immunostained sprouting cultures indicate that choroid sprouts consist of endothelial cells as well as other cell types including pericytes and fibroblasts. Even though the respective signaling cascade in choroidal endothelial cells has not been examined, it is reasonable to speculate that TPC2 plays a similar role in these cells. Additionally, the global VEGFA levels in retinal tissue harvested after the laser-induced CNV were lower in *Tpc2*$^{-/-}$ than in WT control mice, indicating that TPC2 might also be involved upstream of the VEGFA pathway, which also contributes to the effects observed in laser-induced CNV. The development of AMD is guided by several angiogenic factors and among them, VEGFA is the most potent to lead the angiogenic process. In the inflammatory response underlying neovascular AMD, VEGFA is produced by the RPE, Müller glia, as well as activated microglia and macrophages that are invading the area of tissue damage. However, it is unclear in which specific cell type TPC2 plays a role in VEGFA regulation. Further work is required to determine the exact mechanism of how TPC2 affects VEGFA production.

The lower retinal VEGFA levels in *Tpc2*$^{-/-}$ mice, after laser damage, may also result from a reduced immune activation. Indeed, it was consistently observed that a smaller number of invading immune cells accumulated in the lesion area of *Tpc2*$^{-/-}$ eyes compared to WT eyes. Moreover, using endolysosomal patch-clamp experiments, TPC2-mediated currents were identified in microglia and macrophages, indicating that this ion channel is functional in these immune cells. By contrast, only low levels of TPC2 mRNA were detected in RPE and it was not possible to detect TPC2-mediated currents in RPE cells (personal communication Dr. Chen-Chang Chen, not shown), suggesting that TPC2 is of minor importance for these cells. Subsequently, M1 and M2 polarized macrophages were investigated using M-CSF-cultured BMDMs, which are predominant *in vitro* system to generate polarized macrophages [148]. These cells were polarized into M1 macrophages upon the widely-used combination of activators (LPS and IFN-γ), while IL-4 was used to shift cells into the M2 type [149]. The robust increased expression of M1 and M2 markers in respectively activated WT cells indicated the successful establishment of polarized macrophages. Interestingly, TPC2 mRNA levels were dramatically upregulated in cultured M1 and M2 polarized macrophages, implicating this ion channel in both the pro- and anti-inflammatory cell profile. Several lines of evidence suggested

both M1 and M2 states of macrophages exist in the lesion area of AMD and display diverse functions in the pathogenesis [56, 57]. Thus, further experiments such as quantitative flow cytometric analysis could help identify whether the specific pattern and activation status of macrophages were affected in *Tpc2*$^{-/-}$ mice after laser damage.

As there were no differences in morphology and transcriptional expression of M1/M2 markers in *Tpc2*$^{-/-}$ polarized macrophages compared to WT, more comprehensive studies are required to decipher the specific TPC2 function in macrophages. One hypothesis regarding the impact of TPC2 on macrophages is derived from our previous work that demonstrated that TPC2 controls cancer cell migration by modulating the trafficking of β1-integrin [126]. Since the migration/accumulation of proinflammatory (M1) and anti-inflammatory (M2) macrophages in the damaged retinal area is essential for the development and resolution of AMD, the role of TPC2 in macrophage migration was further investigated. Using a transwell migration assay with chemoattractant stimulation, the pattern of M1/M2 macrophages was first established. M2 macrophages exhibited a much greater migratory capacity compared to M1 (Figure 22). These results are in accordance with previously published studies in which the migratory properties of macrophages were considered to be dependent on their activation status [150, 151]. The less motile M1 macrophages might contribute to the clearance of pathogens and toxins in limited areas of a lesion [152], whereas motile M2 macrophages are able to migrate efficiently from lymph nodes towards lesion sites, facilitate wound healing and return the tissue to homeostasis. The transwell migration assay revealed no abrogated migratory ability of polarized macrophages in *Tpc2*$^{-/-}$ polarized macrophages, indicating that deletion of TPC2 does not impact cell mobility. These results are also supported by the consistent TPC2 mRNA levels in M1 and M2 macrophages, regardless of their migratory profile (Figure 21B). Another explanation would be that macrophages might adopt diverse migratory mechanisms in different environments. In fact, unlike metastatic cancer cells, macrophages move rapidly in response to environmental and cellular stimuli. It has been shown that macrophages apply the classical five-step model of migration while moving on a two-dimensional (2D) surface such as endothelial monolayers: *(1)* leading pseudopod formation; *(2)* pseudopod adhesion on the underlying matrix; *(3)* cell body translocation; *(4)* release of trailing edge; *(5)* retraction of the rear end (Figure 30) [153]. In three-dimensional (3D) extracellular matrix (ECM), macrophages utilize mesenchymal or amoeboid migration to reach the inflammation site. The mesenchymal mode strongly relies on adhesion to ECM, whereas the amoeboid migration is based on integrin-independent flowing and squeezing [154]. Furthermore, the migration mode can also vary depending on the extracellular environment and matrix density. As such, these various migration modes have a complex underlying regulatory mechanism. Different maturation and activation states of macrophages might also affect their migration properties. Although the

transwell migration assay has been extensively used to study 2D migration of macrophages, it is a minimalistic model and therefore may not reflect the exact *in vivo* situation. To further elucidate the influence of TPC2 on macrophage migration capacity, improved assays in 3D could be developed to help address this question.

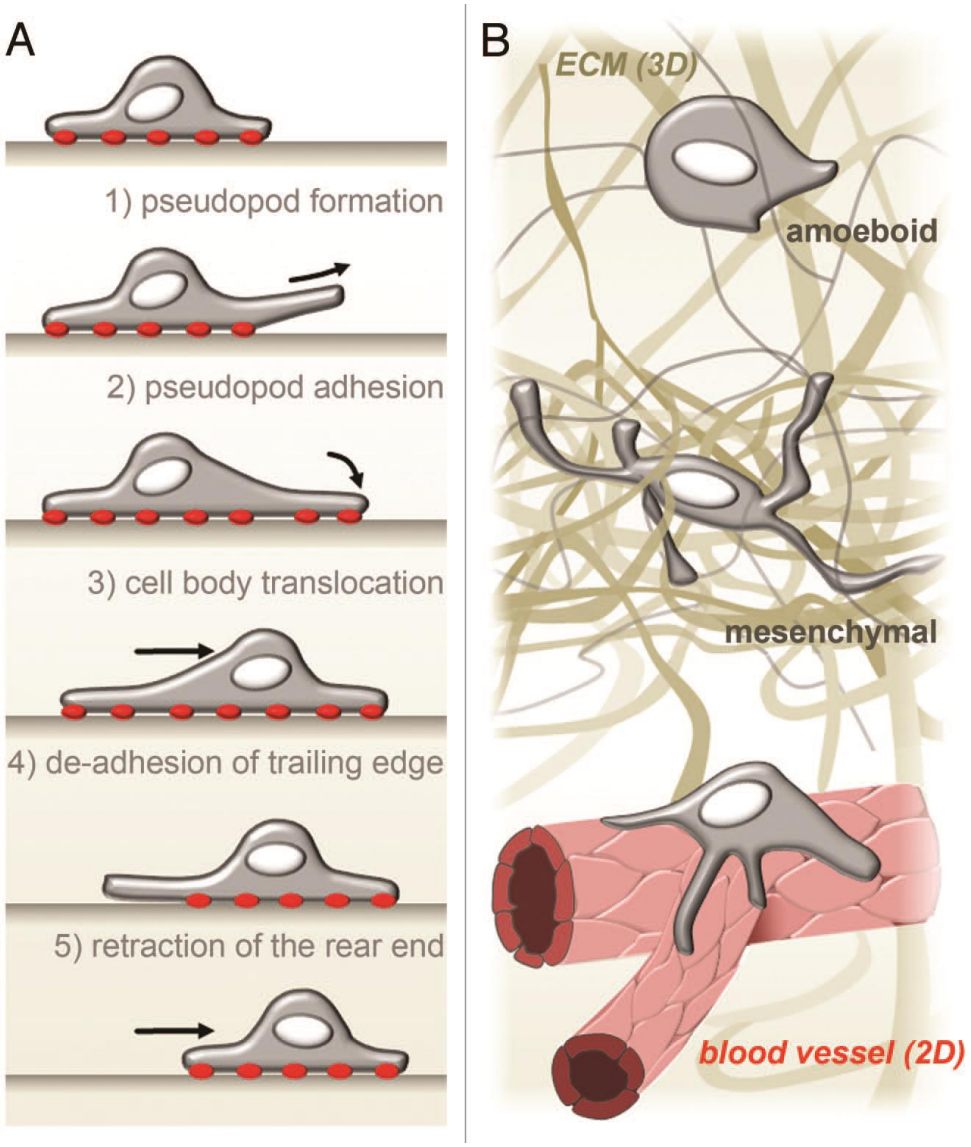

Figure 30 Macrophage migration mode in 2D and 3D.

(A) Macrophages apply the classical five-step model of migration while moving on the 2D surface. (B) Macrophages utilize mesenchymal or amoeboid migration through the 3D extracellular matrix [153].

Macrophages secrete a range of cytokines when exposed to inflammatory stimuli. In addition to VEGFA, the proinflammatory cytokine IL-1β has also been linked to the progression of AMD. Macrophages and microglia, which are recognized as the major cellular source of IL-1β, produce and secrete high amounts of this cytokine in a complex signaling cascade that requires an initial priming step and an activation step. In the priming step, the expression of

inflammasome components and pro-IL-1β are upregulated in response to noxious signals, such as pathogen- or damage-associated molecular patterns (PAMPs or DAMPs), or through cytokines including tumor necrosis factor α (TNFα) or IL-1β itself. In the second step, the inflammasome is activated by PAMPs, DAMPs, or terminal complement component (MAC), followed by the formation and activation of inflammasome, leading to IL-1β processing and extracellular release. Subsequently, the released IL-1β can initiate and propagate inflammatory actions, including the recruitment of macrophages and microglia [155], the release of VEGFA [156], CNV formation [100], and induction of photoreceptor cell death and retinal damage [157]. In this study, the overall IL-1β levels were significantly higher in WT mice compared to *Tpc2*$^{-/-}$ after laser injury (Figure 23 and 24D), suggesting that TPC2 may be involved in the production and/or the release of this cytokine. Experiments with cultured macrophages showed that the initial priming step with LPS stimulation led to the enhanced synthesis of inactive pro-IL-1β, but elicited only modest release of mature IL-1β (Figure 25). When LPS-primed macrophages were additionally challenged with ATP, they rapidly secreted large amounts of mature IL-1β. Based on this experimental approach, it was found that deletion of TPC2 did not affect the production of pro-IL-1β (Figure 25). However, the amount of mature IL-1β in cell culture supernatant was significantly lower in *Tpc2*$^{-/-}$ macrophages compared to WT controls (Figure 26). This was further corroborated by the high IL-1β intensity in *Tpc2*$^{-/-}$ Iba1+ cell from CNV retina sections (Figure 27) and increased accumulation of IL-1β in endolysosomal (LAMP-1+) organelles in *Tpc2*$^{-/-}$ macrophages and microglia compared to WT (Figures 28 and 29). Taken together, these findings show that TPC2 is involved in the vesicular secretion of IL-1β (Figure 31).

IL-1β has been shown to be translated on free polyribosomes associated with the cytoskeleton [158]. Synthesized pro-IL-1β is mainly found in the cytosol and only a portion resides in endolysosomal vesicles destined for degradation [159]. When immune cells respond to a secondary stimulus, such as ATP released by dying cells or other immune cells, a large amount of pro-IL-1β is processed and subsequently secreted extracellularly [160]. As a secretory protein lacking a signal sequence, IL-1β does not follow the conventional route of endoplasmic reticulum-to-Golgi secretory pathway, raising the question of how it can be exported extracellularly. A non-conventional secretory pathway involving lysosomal exocytosis has been proposed in accordance with multiple studies. Using differential ultracentrifugation and immunoelectron microscopy, Andrei *et al.* showed that IL-1β was contained within endosomes and colocalized with lysosomal marker LAMP-1 [86]. It was further shown that the mature IL-1β was detected in the endolysosome-enriched fraction of cells but not in the cytosol [87]. Furthermore, it has been suggested that IL-1β processing and secretion from macrophages are correlated with the release of LAMP-1 [91]. Consistent with

these reports, immunocytochemistry data in this thesis directly confirmed the overlap between IL-1β and LAMP-1 signal in WT macrophages and microglia (Figures 28 and 29). Importantly, this overlap was much more pronounced in the respective *Tpc2*$^{-/-}$ cells, indicating that the deletion of TPC2 impairs the externalization of IL-1β by trapping IL-1β in endolysosomal organelles. There are several possibilities of how TPC2 affects this release. Previous studies demonstrated that sustained cytosolic Ca^{2+} is essential for ATP-induced IL-1β secretion in macrophages [87, 161]. Along this line, it was found that lysosomal Ca^{2+} signaling, but not ER and mitochondria Ca^{2+}, regulate IL-1β secretion by mediating lysosomal exocytosis in monocytic cells. In particular, this lysosomal Ca^{2+} could be blocked by the TPC blocker Ned-19 [162]. Collectively, even though this study did not examine the involvement of lysosomal Ca^{2+} signal on IL-1β secretion, it is likely that the regulation of TPC2 on lysosomal Ca^{2+} homeostasis is responsible for secreting IL-1β into extracellular space via lysosomal exocytosis in macrophages and microglia.

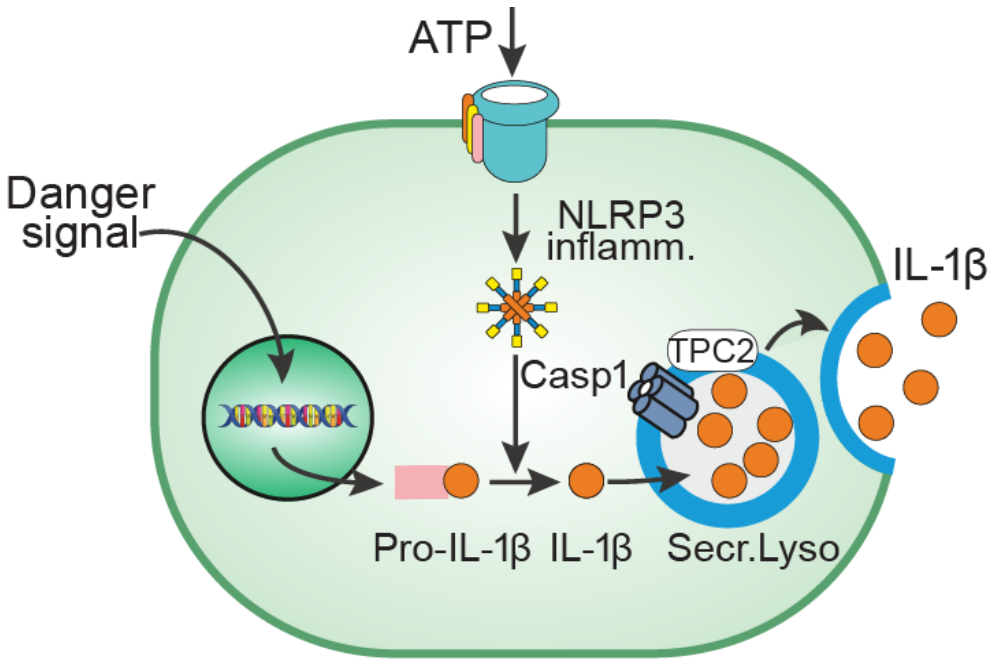

Figure 31 TPC2 regulates IL-1β secretion via lysosome exocytosis in macrophages and microglia

In response to danger signals, macrophages and microglia upregulate the expression of IL-1β and inflammasome components. Upon the stimulation of a second signal such as ATP, NLRP3 inflammasome is assembled and pro- IL-1β is cleaved into mature IL-1β. The subsequent secretion of IL-1β is mediated by TPC2 through lysosome exocytosis.

Endolysosomal trafficking plays a crucial role in a variety of physiological and pathological processes. It can transport intracellular cargos including ligands and receptors for recycling or degradation, or inflammatory cytokines and chemokines for rapid release. TPCs, recognized

as cation channels located in the membrane of endolysosomes, are postulated to contribute to the regulation of intracellular trafficking. To support this theory, there is increasing evidence demonstrating that inhibition of this channel accounts for lysosomal accumulation of a variety of cargoes. For instance, Nguyen *et al.* have found that blocking TPC2 interrupted β1-integrin recycling by accumulating it in endocytic vesicles, leading to the abrogation of cancer cell migration [126]. It has also been shown that deficiency of TPC2 halted the trafficking of LDL-cholesterol and EGF/EGF-receptor in mouse embryonic fibroblasts [123]. Furthermore, disrupting TPC function impeded Ebola virus trafficking through the endolysosomal network, preventing infection [124]. Consistently, this study observed an accumulation of IL-1β in LAMP-1 positive endolysosomal vesicles after deletion of TPC2 in macrophages and microglia, highlighting the involvement of TPC2 in endolysosomal trafficking.

The pathogenesis of AMD involves a number of inflammatory and angiogenic cytokines, such as IL-1α, IL-6, IL-18, IL-33, TNFα, transforming growth factor β (TGFβ), and placental growth factor (PGF). It remains to be confirmed whether TPC2 also accounts for the secretion and signaling cascades of these proteins, as it does for IL-1β. Overall, this study highlights TPC2 as a potential novel drug target against wet AMD.

6 Summary

Neovascular AMD is an inflammatory ocular disease that is characterized by strong activation of the innate immune system, the inadequate release of proangiogenic and proinflammatory factors, abnormal formation of leaky blood vessels as well as the induction of photoreceptor death in the macula. The molecular mechanisms underlying neovascular AMD remain largely unknown. Two-pore channels are members of the large pore-loop cation channel family that are specifically expressed in endolysosomal organelles. There is substantial evidence linking TPCs to several pathophysiological conditions and diseases, such as cancer, cardiac dysfunction, diabetes, fatty liver, and Ebola virus disease. While the influence of TPCs on pathomechanism of AMD has not been investigated. To address this issue, a laser-induced choroidal neovascularization mice model was established with WT and *Tpc2*$^{-/-}$ mice. Surprisingly, genetic deletion of TPC2, as well as acute pharmacological blocking of TPC2, profoundly diminished the formation of leaky choroidal blood vessels and accumulation of immune cells following laser coagulation. Deletion of TPC2 also reduced retinal VEGFA after laser damage.

To assess whether TPC2 is directly associated with angiogenesis, choroidal pieces from WT and *Tpc2*$^{-/-}$ mice were dissected and cultured in presence of VEGFA. Consistent with *in vivo* findings, tissue loss of TPC2 showed limited microvascular outgrowth. It has been reported that TPC2 controls EC proliferation and vessel formation through the VEGFA/VEGFR2 signaling pathway. Furthermore, immunostaining data showed choroidal sprouts consist of endothelial cells which are surrounded by pericytes and fibroblasts. It is reasonable to assume the effect of TPC2 in choroidal sprouting culture is attributed to its regulation in choroidal endothelial cells.

To further determine the potential mechanism in which TPC2 is involved, the expression profiles of TPC2 were firstly examined in different retinal cell types. Both qRT-PCR and endolysosomal patch-clamp analysis showed relatively high expression of TPC2 in macrophages and microglia in comparison to its expression in RPE cells. Moreover, TPC2 mRNA level was significantly upregulated in polarized M1 and M2 macrophages. Based on this, the following studies mainly focused on uncovering the exact functions of TPC2 in immune cells. The initial hypothesis was that TPC2 regulates macrophage migration. However, transwell migration experiment showed that WT and TPC2-deficient macrophages did not differ from each other with regard to their migration pattern. Instead, the following findings in this thesis suggest TPC2 is involved in the secretion of interleukin-1β (IL-1β) which is a key proinflammatory cytokine in AMD. Firstly, ELISA analysis and immunolabeled retinal cross-

sections revealed that the global IL-1β level was significantly lower in *Tpc2*$^{-/-}$ retinas. Interestingly, some *Tpc2*$^{-/-}$ Iba1 positive immune cells displayed a strong IL-1β co-staining. Secondly, qRT-PCR and western blot experiments showed that deletion of TPC2 in cultured BMDMs did not alter the IL-1β expression. Lastly, immunocytochemistry analysis suggested TPC2 deficiency led to the impairment of IL-1β release via lysosomal exocytosis in macrophages and microglia. All of these results demonstrated that TPC2 is not essential for principal priming of BMDMs and expression of IL-1β, but is involved in the release of IL-1β.

Taken together, this thesis reveals a novel role of TPC2 in the inflammatory and neovascular processes of neovascular AMD, providing new insights into the pathomechanism of this disease.

7 References

1. Alfaro, D.V. and J.B. Kerrison, *Age-Related Macular Degeneration*. 2014, Philadelphia, UNITED STATES: Wolters Kluwer Health.
2. Curcio, C.A., J.D. Messinger, K.R. Sloan, A. Mitra, G. McGwin, and R.F. Spaide, *Human chorioretinal layer thicknesses measured in macula-wide, high-resolution histologic sections.* Investigative ophthalmology & visual science, 2011. **52**(7): p. 3943-3954.
3. Klaver, C.C., R.C. Wolfs, J.R. Vingerling, A. Hofman, and P.T. de Jong, *Age-specific prevalence and causes of blindness and visual impairment in an older population: the Rotterdam Study.* Archives of ophthalmology, 1998. **116**(5): p. 653-658.
4. Wong, W.L., X. Su, X. Li, C.M.G. Cheung, R. Klein, C.-Y. Cheng, and T.Y. Wong, *Global prevalence of age-related macular degeneration and disease burden projection for 2020 and 2040: a systematic review and meta-analysis.* The Lancet Global Health, 2014. **2**(2): p. e106-e116.
5. Smith, W., J. Assink, R. Klein, P. Mitchell, C.C. Klaver, B.E. Klein, A. Hofman, S. Jensen, J.J. Wang, and P.T. de Jong, *Risk factors for age-related macular degeneration: pooled findings from three continents.* Ophthalmology, 2001. **108**(4): p. 697-704.
6. Klein, R., B.E. Klein, S.C. Tomany, S.M. Meuer, and G.-H. Huang, *Ten-year incidence and progression of age-related maculopathy: The Beaver Dam eye study.* Ophthalmology, 2002. **109**(10): p. 1767-1779.
7. Chen, Y., J. Zeng, C. Zhao, K. Wang, E. Trood, J. Buehler, M. Weed, D. Kasuga, P.S. Bernstein, and G. Hughes, *Assessing susceptibility to age-related macular degeneration with genetic markers and environmental factors.* Archives of ophthalmology, 2011. **129**(3): p. 344-351.
8. Seddon, J.M., W.C. Willett, F.E. Speizer, and S.E. Hankinson, *A prospective study of cigarette smoking and age-related macular degeneration in women.* Jama, 1996. **276**(14): p. 1141-1146.
9. Halliwell, B., *Reactive oxygen species in living systems: source, biochemistry, and role in human disease.* The American journal of medicine, 1991. **91**(3): p. S14-S22.
10. Friedman, E., *The role of the atherosclerotic process in the pathogenesis of age-related macular degeneration.* American journal of ophthalmology, 2000. **130**(5): p. 658-663.
11. Vingerling, J.R., I. Dielemans, M.L. Bots, A. Hofman, D.E. Grobbee, and P.T. de Jong, *Age-related macular degeneration is associated with atherosclerosis: the Rotterdam Study.* American journal of epidemiology, 1995. **142**(4): p. 404-409.

12. Group, A.-R.E.D.S.R., *Risk factors for the incidence of advanced age-related macular degeneration in the Age-Related Eye Disease Study (AREDS): AREDS report no. 19.* Ophthalmology, 2005. **112**(4): p. 533-539. e1.
13. Wang, I., H.-J. Lin, L. Wan, C.-L. Lin, T.-H. Yen, and F.-C. Sung, *Risk of age-related macular degeneration in end-stage renal disease patients receiving long-term dialysis.* Retina, 2016. **36**(10): p. 1866-1873.
14. Shim, S.H., S.-G. Kim, J.H. Bae, H.G. Yu, and S.J. Song, *Risk factors for progression of early age-related macular degeneration in Koreans.* Ophthalmic Epidemiology, 2016. **23**(2): p. 80-87.
15. Ngai, L., N. Stocks, J. Sparrow, R. Patel, A. Rumley, G. Lowe, G.D. Smith, and Y. Ben-Shlomo, *The prevalence and analysis of risk factors for age-related macular degeneration: 18-year follow-up data from the Speedwell eye study, United Kingdom.* Eye, 2011. **25**(6): p. 784-793.
16. Choudhury, F., R. Varma, R. McKean-Cowdin, R. Klein, S.P. Azen, and L.A.L.E.S. Group, *Risk factors for four-year incidence and progression of age-related macular degeneration: the Los Angeles Latino Eye Study.* American journal of ophthalmology, 2011. **152**(3): p. 385-395.
17. Chen, Y.-J., L. Yeung, C.-C. Sun, C.-C. Huang, K.-S. Chen, and Y.-H. Lu, *Age-related macular degeneration in chronic kidney disease: A meta-analysis of observational studies.* American journal of nephrology, 2018. **48**(4): p. 278-291.
18. Klein, R., M.D. Knudtson, K.E. Lee, and B.E. Klein, *Serum cystatin C level, kidney disease markers, and incidence of age-related macular degeneration: the Beaver Dam Eye Study.* Archives of ophthalmology, 2009. **127**(2): p. 193-199.
19. Gopinath, B., G. Liew, A. Kifley, and P. Mitchell, *Thyroid dysfunction and ten-year incidence of age-related macular degeneration.* Investigative ophthalmology & visual science, 2016. **57**(13): p. 5273-5277.
20. Lin, S.-Y., W.-H. Hsu, C.-L. Lin, C.-C. Lin, J.-M. Lin, Y.-L. Chang, C.-Y. Hsu, and C.-H. Kao, *Evidence for an association between macular degeneration and thyroid cancer in the aged population.* International journal of environmental research and public health, 2018. **15**(5): p. 902.
21. Obisesan, T.O., R. Hirsch, O. Kosoko, L. Carlson, and M. Parrott, *Moderate wine consumption is associated with decreased odds of developing age‐related macular degeneration in NHANES‐1.* Journal of the American Geriatrics Society, 1998. **46**(1): p. 1-7.

22. Blumenkranz, M.S., S.R. Russell, M.G. Robey, R. Kott-Blumenkranz, and N. Penneys, *Risk factors in age-related maculopathy complicated by choroidal neovascularization.* Ophthalmology, 1986. **93**(5): p. 552-558.
23. Taylor, H.R., B. Munoz, S. West, N.M. Bressler, S.B. Bressler, and F.S. Rosenthal, *Visible light and risk of age-related macular degeneration.* Transactions of the American Ophthalmological Society, 1990. **88**: p. 163.
24. Darzins, P., P. Mitchell, and R.F. Heller, *Sun exposure and age-related macular degeneration: An australian case—control study.* Ophthalmology, 1997. **104**(5): p. 770-776.
25. Smith, W., P. Mitchell, and S.R. Leeder, *Dietary fat and fish intake and age-related maculopathy.* Archives of ophthalmology, 2000. **118**(3): p. 401-404.
26. Mousavi, M. and R.A. Armstrong, *Genetic risk factors and age-related macular degeneration (AMD).* Journal of Optometry, 2013. **6**(4): p. 176-184.
27. Jarrett, S.G. and M.E. Boulton, *Consequences of oxidative stress in age-related macular degeneration.* Molecular aspects of medicine, 2012. **33**(4): p. 399-417.
28. Canter, J.A., L.M. Olson, K. Spencer, N. Schnetz-Boutaud, B. Anderson, M.A. Hauser, S. Schmidt, E.A. Postel, A. Agarwal, and M.A. Pericak-Vance, *Mitochondrial DNA polymorphism A4917G is independently associated with age-related macular degeneration.* PLoS One, 2008. **3**(5): p. e2091.
29. Chen, W., D. Stambolian, A.O. Edwards, K.E. Branham, M. Othman, J. Jakobsdottir, N. Tosakulwong, M.A. Pericak-Vance, P.A. Campochiaro, and M.L. Klein, *Genetic variants near TIMP3 and high-density lipoprotein–associated loci influence susceptibility to age-related macular degeneration.* Proceedings of the National Academy of Sciences, 2010. **107**(16): p. 7401-7406.
30. Fritsche, L.G., S. Freitag‐Wolf, T. Bettecken, T. Meitinger, C.N. Keilhauer, M. Krawczak, and B.H. Weber, *Age‐related macular degeneration and functional promoter and coding variants of the apolipoprotein E gene.* Human mutation, 2009. **30**(7): p. 1048-1053.
31. Gold, B., J.E. Merriam, J. Zernant, L.S. Hancox, A.J. Taiber, K. Gehrs, K. Cramer, J. Neel, J. Bergeron, and G.R. Barile, *Variation in factor B (BF) and complement component 2 (C2) genes is associated with age-related macular degeneration.* Nature genetics, 2006. **38**(4): p. 458-462.
32. Yates, J.R., T. Sepp, B.K. Matharu, J.C. Khan, D.A. Thurlby, H. Shahid, D.G. Clayton, C. Hayward, J. Morgan, and A.F. Wright, *Complement C3 variant and the risk of age-related macular degeneration.* New England Journal of Medicine, 2007. **357**(6): p. 553-561.

33. Fagerness, J.A., J.B. Maller, B.M. Neale, R.C. Reynolds, M.J. Daly, and J.M. Seddon, *Variation near complement factor I is associated with risk of advanced AMD.* European Journal of Human Genetics, 2009. **17**(1): p. 100-104.
34. DeWan, A., M. Liu, S. Hartman, S.S.-M. Zhang, D.T. Liu, C. Zhao, P.O. Tam, W.M. Chan, D.S. Lam, and M. Snyder, *HTRA1 promoter polymorphism in wet age-related macular degeneration.* Science, 2006. **314**(5801): p. 989-992.
35. Streilein, J.W., *Immunological non-responsiveness and acquisition of tolerance in relation to immune privilege in the eye.* Eye, 1995. **9**(2): p. 236-240.
36. Ambati, J., J.P. Atkinson, and B.D. Gelfand, *Immunology of age-related macular degeneration.* Nature Reviews Immunology, 2013. **13**(6): p. 438-451.
37. Horie, S., S. Sugita, Y. Futagami, Y. Yamada, and M. Mochizuki, *Human retinal pigment epithelium-induced CD4+ CD25+ regulatory T cells suppress activation of intraocular effector T cells.* Clinical Immunology, 2010. **136**(1): p. 83-95.
38. Cunha-Vaz, J.G., *The blood–retinal barriers system. Basic concepts and clinical evaluation.* Experimental eye research, 2004. **78**(3): p. 715-721.
39. Caspi, R.R., *Ocular autoimmunity: the price of privilege?* Immunological reviews, 2006. **213**(1): p. 23-35.
40. Thanos, S., *The relationship of microglial cells to dying neurons during natural neuronal cell death and axotomy-induced degeneration of the Rat retina.* European Journal of Neuroscience, 1991. **3**(12): p. 1189-1207.
41. Roumier, A., C. Béchade, J.-C. Poncer, K.-H. Smalla, E. Tomasello, E. Vivier, E.D. Gundelfinger, A. Triller, and A. Bessis, *Impaired synaptic function in the microglial KARAP/DAP12-deficient mouse.* Journal of Neuroscience, 2004. **24**(50): p. 11421-11428.
42. Provis, J., C. Diaz, and P. Penfold, *Microglia in human retina: a heterogeneous population with distinct ontogenies.* Perspectives on developmental neurobiology, 1996. **3**(3): p. 213-222.
43. Santos, A.M., R. Calvente, M. Tassi, M.C. Carrasco, D. Martín-Oliva, J.L. Marín-Teva, J. Navascués, and M.A. Cuadros, *Embryonic and postnatal development of microglial cells in the mouse retina.* Journal of Comparative Neurology, 2008. **506**(2): p. 224-239.
44. Damani, M.R., L. Zhao, A.M. Fontainhas, J. Amaral, R.N. Fariss, and W.T. Wong, *Age-related alterations in the dynamic behavior of microglia.* Aging cell, 2011. **10**(2): p. 263-276.
45. Gupta, N., K.E. Brown, and A.H. Milam, *Activated microglia in human retinitis pigmentosa, late-onset retinal degeneration, and age-related macular degeneration.* Experimental eye research, 2003. **76**(4): p. 463-471.

46. Xu, H., M. Chen, A. Manivannan, N. Lois, and J.V. Forrester, *Age‐dependent accumulation of lipofuscin in perivascular and subretinal microglia in experimental mice.* Aging cell, 2008. **7**(1): p. 58-68.
47. Killingsworth, M., J. Sarks, and S. Sarks, *Macrophages related to Bruch's membrane in age-related macular degeneration.* Eye, 1990. **4**(4): p. 613-621.
48. Grossniklaus, H.E., P.H. Miskala, W.R. Green, S.B. Bressler, B.S. Hawkins, C. Toth, D.J. Wilson, and N.M. Bressler, *Histopathologic and ultrastructural features of surgically excised subfoveal choroidal neovascular lesions: submacular surgery trials report no. 7.* Archives of ophthalmology (Chicago, Ill.: 1960), 2005. **123**(7): p. 914-921.
49. Shen, W., M. Yu, C. Barry, I. Constable, and P. Rakoczy, *Expression of cell adhesion molecules and vascular endothelial growth factor in experimental choroidal neovascularisation in the rat.* British Journal of Ophthalmology, 1998. **82**(9): p. 1063-1071.
50. Sakurai, E., A. Anand, B.K. Ambati, N. van Rooijen, and J. Ambati, *Macrophage depletion inhibits experimental choroidal neovascularization.* Investigative ophthalmology & visual science, 2003. **44**(8): p. 3578-3585.
51. Apte, R.S., J. Richter, J. Herndon, and T.A. Ferguson, *Macrophages inhibit neovascularization in a murine model of age-related macular degeneration.* PLoS Med, 2006. **3**(8): p. e310.
52. Ambati, J., A. Anand, S. Fernandez, E. Sakurai, B.C. Lynn, W.A. Kuziel, B.J. Rollins, and B.K. Ambati, *An animal model of age-related macular degeneration in senescent Ccl-2-or Ccr-2-deficient mice.* Nature medicine, 2003. **9**(11): p. 1390-1397.
53. Mantovani, A., A. Sica, S. Sozzani, P. Allavena, A. Vecchi, and M. Locati, *The chemokine system in diverse forms of macrophage activation and polarization.* Trends in immunology, 2004. **25**(12): p. 677-686.
54. Martinez, F.O., A. Sica, A. Mantovani, and M. Locati, *Macrophage activation and polarization.* Front biosci, 2008. **13**(1): p. 453-461.
55. Gordon, S., *Alternative activation of macrophages.* Nature reviews immunology, 2003. **3**(1): p. 23-35.
56. Cao, X., D. Shen, M.M. Patel, J. Tuo, T.M. Johnson, T.W. Olsen, and C.C. Chan, *Macrophage polarization in the maculae of age‐related macular degeneration: A pilot study.* Pathology international, 2011. **61**(9): p. 528-535.
57. Yang, Y., F. Liu, M. Tang, M. Yuan, A. Hu, Z. Zhan, Z. Li, J. Li, X. Ding, and L. Lu, *Macrophage polarization in experimental and clinical choroidal neovascularization.* Scientific reports, 2016. **6**(1): p. 1-12.

58. Zandi, S., S. Nakao, K.-H. Chun, P. Fiorina, D. Sun, R. Arita, M. Zhao, E. Kim, O. Schueller, and S. Campbell, *ROCK-isoform-specific polarization of macrophages associated with age-related macular degeneration.* Cell reports, 2015. **10**(7): p. 1173-1186.

59. Haines, J.L., M.A. Hauser, S. Schmidt, W.K. Scott, L.M. Olson, P. Gallins, K.L. Spencer, S.Y. Kwan, M. Noureddine, and J.R. Gilbert, *Complement factor H variant increases the risk of age-related macular degeneration.* Science, 2005. **308**(5720): p. 419-421.

60. Edwards, A.O., R. Ritter, K.J. Abel, A. Manning, C. Panhuysen, and L.A. Farrer, *Complement factor H polymorphism and age-related macular degeneration.* Science, 2005. **308**(5720): p. 421-424.

61. Clark, S.J., R. Perveen, S. Hakobyan, B.P. Morgan, R.B. Sim, P.N. Bishop, and A.J. Day, *Impaired binding of the age-related macular degeneration-associated complement factor H 402H allotype to Bruch's membrane in human retina.* Journal of Biological Chemistry, 2010. **285**(39): p. 30192-30202.

62. Johnson, P., K. Betts, M. Radeke, G. Hageman, D. Anderson, and L. Johnson, *Individuals homozygous for the age-related macular degeneration risk-conferring variant of complement factor H have elevated levels of CRP in the choroid.* Proceedings of the National Academy of Sciences, 2006. **103**(46): p. 17456-17461.

63. Gasque, P., *Complement: a unique innate immune sensor for danger signals.* Molecular immunology, 2004. **41**(11): p. 1089-1098.

64. Korb, L.C. and J.M. Ahearn, *C1q binds directly and specifically to surface blebs of apoptotic human keratinocytes: complement deficiency and systemic lupus erythematosus revisited.* The Journal of Immunology, 1997. **158**(10): p. 4525-4528.

65. Frank, M.M. and L.F. Fries, *The role of complement in inflammation and phagocytosis.* Immunology today, 1991. **12**(9): p. 322-326.

66. Wallis, R., D.A. Mitchell, R. Schmid, W.J. Schwaeble, and A.H. Keeble, *Paths reunited: Initiation of the classical and lectin pathways of complement activation.* Immunobiology, 2010. **215**(1): p. 1-11.

67. Wallis, R., *Interactions between mannose-binding lectin and MASPs during complement activation by the lectin pathway.* Immunobiology, 2007. **212**(4-5): p. 289-299.

68. Müller-Eberhard, H.J., *The killer molecule of complement.* Journal of Investigative Dermatology, 1985. **85**(1): p. S47-S52.

69. Fujita, T., T. Inoue, K. Ogawa, K. Iida, and N. Tamura, *The mechanism of action of decay-accelerating factor (DAF). DAF inhibits the assembly of C3 convertases by dissociating C2a and Bb.* The Journal of experimental medicine, 1987. **166**(5): p. 1221-1228.

70. Huang, Y., F. Qiao, R. Abagyan, S. Hazard, and S. Tomlinson, *Defining the CD59-C9 binding interaction.* Journal of Biological Chemistry, 2006. **281**(37): p. 27398-27404.
71. Jokiranta, T.S., J. Hellwage, V. Koistinen, P.F. Zipfel, and S. Meri, *Each of the three binding sites on complement factor H interacts with a distinct site on C3b.* Journal of Biological Chemistry, 2000. **275**(36): p. 27657-27662.
72. Mathern, D.R. and P.S. Heeger, *Molecules great and small: the complement system.* Clinical Journal of the American Society of Nephrology, 2015. **10**(9): p. 1636-1650.
73. Anderson, D.H., M.J. Radeke, N.B. Gallo, E.A. Chapin, P.T. Johnson, C.R. Curletti, L.S. Hancox, J. Hu, J.N. Ebright, and G. Malek, *The pivotal role of the complement system in aging and age-related macular degeneration: hypothesis re-visited.* Progress in retinal and eye research, 2010. **29**(2): p. 95-112.
74. Chen, M., E. Muckersie, J.V. Forrester, and H. Xu, *Immune activation in retinal aging: a gene expression study.* Investigative ophthalmology & visual science, 2010. **51**(11): p. 5888-5896.
75. Bora, P.S., J.-H. Sohn, J.M. Cruz, P. Jha, H. Nishihori, Y. Wang, S. Kaliappan, H.J. Kaplan, and N.S. Bora, *Role of complement and complement membrane attack complex in laser-induced choroidal neovascularization.* The Journal of Immunology, 2005. **174**(1): p. 491-497.
76. Brockmann, C., T. Brockmann, S. Dege, C. Busch, N. Kociok, A. Vater, S. Klussmann, O. Strauß, and A.M. Joussen, *Intravitreal inhibition of complement C5a reduces choroidal neovascularization in mice.* Graefe's Archive for Clinical and Experimental Ophthalmology, 2015. **253**(10): p. 1695-1704.
77. Wells, J.A., R. Murthy, R. Chibber, A. Nunn, P.A. Molinatti, E.M. Kohner, and Z.J. Gregor, *Levels of vascular endothelial growth factor are elevated in the vitreous of patients with subretinal neovascularisation.* British Journal of Ophthalmology, 1996. **80**(4): p. 363-366.
78. Kvanta, A., P. Algvere, L. Berglin, and S. Seregard, *Subfoveal fibrovascular membranes in age-related macular degeneration express vascular endothelial growth factor.* Investigative ophthalmology & visual science, 1996. **37**(9): p. 1929-1934.
79. Lim, L.S., P. Mitchell, J.M. Seddon, F.G. Holz, and T.Y. Wong, *Age-related macular degeneration.* The Lancet, 2012. **379**(9827): p. 1728-1738.
80. Gehrs, K.M., J.R. Jackson, E.N. Brown, R. Allikmets, and G.S. Hageman, *Complement, Age-Related Macular Degeneration and a Vision of the Future.* Archives of Ophthalmology, 2010. **128**(3): p. 349-358.
81. Sato, T., M. Takeuchi, Y. Karasawa, K. Takayama, and T. Enoki, *Comprehensive expression patterns of inflammatory cytokines in aqueous humor of patients with neovascular age-related macular degeneration.* Scientific reports, 2019. **9**(1): p. 1-13.

82. Afonina, I.S., C. Müller, S.J. Martin, and R. Beyaert, *Proteolytic processing of interleukin-1 family cytokines: variations on a common theme.* Immunity, 2015. **42**(6): p. 991-1004.
83. Miller, D., J. Ayala, L. Egger, S. Raju, T.-T. Yamin, G. Ding, E. Gaffney, A. Howard, O. Palyha, and A. Rolando, *Purification and characterization of active human interleukin-1 beta-converting enzyme from THP. 1 monocytic cells.* Journal of Biological Chemistry, 1993. **268**(24): p. 18062-18069.
84. Li, P., H. Allen, S. Banerjee, S. Franklin, L. Herzog, C. Johnston, J. McDowell, M. Paskind, L. Rodman, and J. Salfeld, *Mice deficient in IL-1β-converting enzyme are defective in production of mature IL-1β and resistant to endotoxic shock.* Cell, 1995. **80**(3): p. 401-411.
85. Martinon, F., O. Gaide, V. Pétrilli, A. Mayor, and J. Tschopp. *NALP inflammasomes: a central role in innate immunity*. in *Seminars in immunopathology*. 2007. Springer.
86. Andrei, C., C. Dazzi, L. Lotti, M.R. Torrisi, G. Chimini, and A. Rubartelli, *The secretory route of the leaderless protein interleukin 1β involves exocytosis of endolysosome-related vesicles.* Molecular biology of the cell, 1999. **10**(5): p. 1463-1475.
87. Andrei, C., P. Margiocco, A. Poggi, L.V. Lotti, M. Torrisi, and A. Rubartelli, *Phospholipases C and A2 control lysosome-mediated IL-1β secretion: implications for inflammatory processes.* Proceedings of the National Academy of Sciences, 2004. **101**(26): p. 9745-9750.
88. MacKenzie, A., H.L. Wilson, E. Kiss-Toth, S.K. Dower, R.A. North, and A. Surprenant, *Rapid secretion of interleukin-1β by microvesicle shedding.* Immunity, 2001. **15**(5): p. 825-835.
89. Pizzirani, C., D. Ferrari, P. Chiozzi, E. Adinolfi, D. Sandona, E. Savaglio, and F. Di Virgilio, *Stimulation of P2 receptors causes release of IL-1β–loaded microvesicles from human dendritic cells.* Blood, 2007. **109**(9): p. 3856-3864.
90. Bianco, F., E. Pravettoni, A. Colombo, U. Schenk, T. Möller, M. Matteoli, and C. Verderio, *Astrocyte-derived ATP induces vesicle shedding and IL-1β release from microglia.* The Journal of Immunology, 2005. **174**(11): p. 7268-7277.
91. Qu, Y., L. Franchi, G. Nunez, and G.R. Dubyak, *Nonclassical IL-1β secretion stimulated by P2X7 receptors is dependent on inflammasome activation and correlated with exosome release in murine macrophages.* The Journal of Immunology, 2007. **179**(3): p. 1913-1925.
92. Théry, C., L. Zitvogel, and S. Amigorena, *Exosomes: composition, biogenesis and function.* Nature reviews immunology, 2002. **2**(8): p. 569-579.
93. Brough, D. and N.J. Rothwell, *Caspase-1-dependent processing of pro-interleukin-1β is cytosolic and precedes cell death.* Journal of cell science, 2007. **120**(5): p. 772-781.

94. Harris, J., M. Hartman, C. Roche, S.G. Zeng, A. O'Shea, F.A. Sharp, E.M. Lambe, E.M. Creagh, D.T. Golenbock, and J. Tschopp, *Autophagy controls IL-1β secretion by targeting pro-IL-1β for degradation.* Journal of Biological Chemistry, 2011. **286**(11): p. 9587-9597.
95. Piccioli, P. and A. Rubartelli. *The secretion of IL-1β and options for release*. in *Seminars in immunology*. 2013. Elsevier.
96. Wesche, H., C. Korherr, M. Kracht, W. Falk, K. Resch, and M.U. Martin, *The interleukin-1 receptor accessory protein (IL-1RAcP) is essential for IL-1-induced activation of interleukin-1 receptor-associated kinase (IRAK) and stress-activated protein kinases (SAP kinases).* Journal of Biological Chemistry, 1997. **272**(12): p. 7727-7731.
97. Tseng, W.A., T. Thein, K. Kinnunen, K. Lashkari, M.S. Gregory, P.A. D'Amore, and B.R. Ksander, *NLRP3 inflammasome activation in retinal pigment epithelial cells by lysosomal destabilization: implications for age-related macular degeneration.* Investigative ophthalmology & visual science, 2013. **54**(1): p. 110-120.
98. Zhao, M., Y. Bai, W. Xie, X. Shi, F. Li, F. Yang, Y. Sun, L. Huang, and X. Li, *Interleukin-1β level is increased in vitreous of patients with neovascular age-related macular degeneration (nAMD) and polypoidal choroidal vasculopathy (PCV).* PLoS One, 2015. **10**(5): p. e0125150.
99. Marneros, A.G., *NLRP3 inflammasome blockade inhibits VEGF-A-induced age-related macular degeneration.* Cell reports, 2013. **4**(5): p. 945-958.
100. Lavalette, S., W. Raoul, M. Houssier, S. Camelo, O. Levy, B. Calippe, L. Jonet, F. Behar-Cohen, S. Chemtob, and X. Guillonneau, *Interleukin-1β inhibition prevents choroidal neovascularization and does not exacerbate photoreceptor degeneration.* The American journal of pathology, 2011. **178**(5): p. 2416-2423.
101. De Duve, C., B. Pressman, R. Gianetto, R. Wattiaux, and F. Appelmans, *Tissue fractionation studies. 6. Intracellular distribution patterns of enzymes in rat-liver tissue.* Biochemical Journal, 1955. **60**(4): p. 604-617.
102. Rink, J., E. Ghigo, Y. Kalaidzidis, and M. Zerial, *Rab conversion as a mechanism of progression from early to late endosomes.* Cell, 2005. **122**(5): p. 735-749.
103. Luzio, J.P., P.R. Pryor, and N.A. Bright, *Lysosomes: fusion and function.* Nature reviews Molecular cell biology, 2007. **8**(8): p. 622-632.
104. Medina, D.L., A. Fraldi, V. Bouche, F. Annunziata, G. Mansueto, C. Spampanato, C. Puri, A. Pignata, J.A. Martina, and M. Sardiello, *Transcriptional activation of lysosomal exocytosis promotes cellular clearance.* Developmental cell, 2011. **21**(3): p. 421-430.

105. Ludwig, A.-K. and B. Giebel, *Exosomes: small vesicles participating in intercellular communication.* The international journal of biochemistry & cell biology, 2012. **44**(1): p. 11-15.

106. Zong, X., M. Schieder, H. Cuny, S. Fenske, C. Gruner, K. Rötzer, O. Griesbeck, H. Harz, M. Biel, and C. Wahl-Schott, *The two-pore channel TPCN2 mediates NAADP-dependent Ca 2+-release from lysosomal stores.* Pflügers Archiv-European Journal of Physiology, 2009. **458**(5): p. 891-899.

107. Calcraft, P.J., M. Ruas, Z. Pan, X. Cheng, A. Arredouani, X. Hao, J. Tang, K. Rietdorf, L. Teboul, and K.-T. Chuang, *NAADP mobilizes calcium from acidic organelles through two-pore channels.* Nature, 2009. **459**(7246): p. 596-600.

108. Brailoiu, E., D. Churamani, X. Cai, M.G. Schrlau, G.C. Brailoiu, X. Gao, R. Hooper, M.J. Boulware, N.J. Dun, and J.S. Marchant, *Essential requirement for two-pore channel 1 in NAADP-mediated calcium signaling.* Journal of Cell Biology, 2009. **186**(2): p. 201-209.

109. Patel, S., C.J. Penny, and T. Rahman, *Two-pore channels enter the atomic era: Structure of plant TPC revealed.* Trends in biochemical sciences, 2016. **41**(6): p. 475-477.

110. She, J., J. Guo, Q. Chen, W. Zeng, Y. Jiang, and X.-c. Bai, *Structural insights into the voltage and phospholipid activation of the mammalian TPC1 channel.* Nature, 2018. **556**(7699): p. 130-134.

111. She, J., W. Zeng, J. Guo, Q. Chen, X.-c. Bai, and Y. Jiang, *Structural mechanisms of phospholipid activation of the human TPC2 channel.* Elife, 2019. **8**: p. e45222.

112. Morgan, A.J., F.M. Platt, E. Lloyd-Evans, and A. Galione, *Molecular mechanisms of endolysosomal Ca2+ signalling in health and disease.* Biochemical Journal, 2011. **439**(3): p. 349-378.

113. Ruas, M., K.-T. Chuang, L.C. Davis, A. Al-Douri, P.W. Tynan, R. Tunn, L. Teboul, A. Galione, and J. Parrington, *TPC1 has two variant isoforms, and their removal has different effects on endo-lysosomal functions compared to loss of TPC2.* Molecular and cellular biology, 2014. **34**(21): p. 3981-3992.

114. Ruas, M., A. Galione, and J. Parrington, *Two-pore channels: lessons from mutant mouse models.* Messenger, 2015. **4**(1): p. 4-22.

115. Grimm, C., C.-C. Chen, C. Wahl-Schott, and M. Biel, *Two-pore channels: catalyzers of endolysosomal transport and function.* Frontiers in pharmacology, 2017. **8**: p. 45.

116. Chini, E.N., K.W. Beers, and T.P. Dousa, *Nicotinate adenine dinucleotide phosphate (NAADP) triggers a specific calcium release system in sea urchin eggs.* Journal of Biological Chemistry, 1995. **270**(7): p. 3216-3223.

117. Davis, L.C., A.J. Morgan, J.-L. Chen, C.M. Snead, D. Bloor-Young, E. Shenderov, M.N. Stanton-Humphreys, S.J. Conway, G.C. Churchill, and J. Parrington, *NAADP activates two-pore channels on T cell cytolytic granules to stimulate exocytosis and killing.* Current Biology, 2012. **22**(24): p. 2331-2337.

118. Roggenkamp, H.G., I. Khansahib, Y. Zhang, D. Lodygin, A. Krüger, F. Gu, F. Möckl, A. Löhndorf, V. Wolters, and D. Woike, *HN1L/JPT2: A signaling protein that connects NAADP generation to Ca2+ microdomain formation.* Science Signaling, 2021. **14**(675).

119. Wang, X., X. Zhang, X.-p. Dong, M. Samie, X. Li, X. Cheng, A. Goschka, D. Shen, Y. Zhou, and J. Harlow, *TPC proteins are phosphoinositide-activated sodium-selective ion channels in endosomes and lysosomes.* Cell, 2012. **151**(2): p. 372-383.

120. Jha, A., M. Ahuja, S. Patel, E. Brailoiu, and S. Muallem, *Convergent regulation of the lysosomal two‐pore channel‐2 by M g2+, NAADP, PI (3, 5) P 2 and multiple protein kinases.* The EMBO journal, 2014. **33**(5): p. 501-511.

121. Cang, C., Y. Zhou, B. Navarro, Y.-j. Seo, K. Aranda, L. Shi, S. Battaglia-Hsu, I. Nissim, D.E. Clapham, and D. Ren, *mTOR regulates lysosomal ATP-sensitive two-pore Na+ channels to adapt to metabolic state.* Cell, 2013. **152**(4): p. 778-790.

122. Ruas, M., K. Rietdorf, A. Arredouani, L.C. Davis, E. Lloyd-Evans, H. Koegel, T.M. Funnell, A.J. Morgan, J.A. Ward, and K. Watanabe, *Purified TPC isoforms form NAADP receptors with distinct roles for Ca2+ signaling and endolysosomal trafficking.* Current biology, 2010. **20**(8): p. 703-709.

123. Grimm, C., L.M. Holdt, C.-C. Chen, S. Hassan, C. Müller, S. Jörs, H. Cuny, S. Kissing, B. Schröder, and E. Butz, *High susceptibility to fatty liver disease in two-pore channel 2-deficient mice.* Nature communications, 2014. **5**(1): p. 1-13.

124. Sakurai, Y., A.A. Kolokoltsov, C.-C. Chen, M.W. Tidwell, W.E. Bauta, N. Klugbauer, C. Grimm, C. Wahl-Schott, M. Biel, and R.A. Davey, *Two-pore channels control Ebola virus host cell entry and are drug targets for disease treatment.* Science, 2015. **347**(6225): p. 995-998.

125. Gunaratne, G.S., Y. Yang, F. Li, T.F. Walseth, and J.S. Marchant, *NAADP-dependent Ca2+ signaling regulates Middle East respiratory syndrome-coronavirus pseudovirus translocation through the endolysosomal system.* Cell Calcium, 2018. **75**: p. 30-41.

126. Nguyen, O.N.P., C. Grimm, L.S. Schneider, Y.-K. Chao, C. Atzberger, K. Bartel, A. Watermann, M. Ulrich, D. Mayr, and C. Wahl-Schott, *Two-pore channel function is crucial for the migration of invasive cancer cells.* Cancer Research, 2017. **77**(6): p. 1427-1438.

127. Lu, Y., B. Hao, R. Graeff, and J. Yue, *NAADP/TPC2/Ca2+ signaling inhibits autophagy.* Communicative & integrative biology, 2013. **6**(6): p. e27595.

128. Chao, Y.-K., V. Schludi, C.-C. Chen, E. Butz, O.P. Nguyen, M. Müller, J. Krüger, C. Kammerbauer, M. Ben-Johny, and A.M. Vollmar, *TPC2 polymorphisms associated with a hair pigmentation phenotype in humans result in gain of channel function by independent mechanisms.* Proceedings of the National Academy of Sciences, 2017. **114**(41): p. E8595-E8602.

129. Hockey, L.N., B.S. Kilpatrick, E.R. Eden, Y. Lin-Moshier, G.C. Brailoiu, E. Brailoiu, C.E. Futter, A.H. Schapira, J.S. Marchant, and S. Patel, *Dysregulation of lysosomal morphology by pathogenic LRRK2 is corrected by TPC2 inhibition.* Journal of cell science, 2015. **128**(2): p. 232-238.

130. Tsaih, S.-W., K. Holl, S. Jia, M. Kaldunski, M. Tschannen, H. He, J.W. Andrae, S.-H. Li, A. Stoddard, and A. Wiederhold, *Identification of a novel gene for diabetic traits in rats, mice, and humans.* Genetics, 2014. **198**(1): p. 17-29.

131. Davidson, S.M., K. Foote, S. Kunuthur, R. Gosain, N. Tan, R. Tyser, Y.J. Zhao, R. Graeff, A. Ganesan, and M.R. Duchen, *Inhibition of NAADP signalling on reperfusion protects the heart by preventing lethal calcium oscillations via two-pore channel 1 and opening of the mitochondrial permeability transition pore.* Cardiovascular research, 2015. **108**(3): p. 357-366.

132. Arlt, E., M. Fraticelli, V. Tsvilovskyy, W. Nadolni, A. Breit, T.J. O'Neill, S. Resenberger, G. Wennemuth, C. Wahl-Schott, and M. Biel, *TPC1 deficiency or blockade augments systemic anaphylaxis and mast cell activity.* Proceedings of the National Academy of Sciences, 2020. **117**(30): p. 18068-18078.

133. Favia, A., M. Desideri, G. Gambara, A. D'Alessio, M. Ruas, B. Esposito, D. Del Bufalo, J. Parrington, E. Ziparo, and F. Palombi, *VEGF-induced neoangiogenesis is mediated by NAADP and two-pore channel-2–dependent Ca2+ signaling.* Proceedings of the National Academy of Sciences, 2014. **111**(44): p. E4706-E4715.

134. Shao, Z., M. Friedlander, C.G. Hurst, Z. Cui, D.T. Pei, L.P. Evans, A.M. Juan, H. Tahir, F. Duhamel, and J. Chen, *Choroid sprouting assay: an ex vivo model of microvascular angiogenesis.* PLoS One, 2013. **8**(7): p. e69552.

135. Lambert, V., J. Lecomte, S. Hansen, S. Blacher, M.-L.A. Gonzalez, I. Struman, N.E. Sounni, E. Rozet, P. De Tullio, and J.M. Foidart, *Laser-induced choroidal neovascularization model to study age-related macular degeneration in mice.* Nature protocols, 2013. **8**(11): p. 2197.

136. Naylor, E., A. Arredouani, S.R. Vasudevan, A.M. Lewis, R. Parkesh, A. Mizote, D. Rosen, J.M. Thomas, M. Izumi, and A. Ganesan, *Identification of a chemical probe for NAADP by virtual screening.* Nature chemical biology, 2009. **5**(4): p. 220-226.

137. Xie, C.B., D. Jane-Wit, and J.S. Pober, *Complement membrane attack complex: new roles, mechanisms of action, and therapeutic targets.* The American Journal of Pathology, 2020.

138. Cang, C., B. Bekele, and D. Ren, *The voltage-gated sodium channel TPC1 confers endolysosomal excitability.* Nature chemical biology, 2014. **10**(6): p. 463-469.

139. Wooff, Y., S.M. Man, R. Natoli, R. Aggio-Bruce, and N. Fernando, *IL-1 family members mediate cell death, inflammation and angiogenesis in retinal degenerative diseases.* Frontiers in immunology, 2019. **10**: p. 1618.

140. Lopez-Castejon, G. and D. Brough, *Understanding the mechanism of IL-1β secretion.* Cytokine & growth factor reviews, 2011. **22**(4): p. 189-195.

141. Pennesi, M.E., M. Neuringer, and R.J. Courtney, *Animal models of age related macular degeneration.* Molecular aspects of medicine, 2012. **33**(4): p. 487-509.

142. Combadière, C., C. Feumi, W. Raoul, N. Keller, M. Rodéro, A. Pézard, S. Lavalette, M. Houssier, L. Jonet, and E. Picard, *CX3CR1-dependent subretinal microglia cell accumulation is associated with cardinal features of age-related macular degeneration.* The Journal of clinical investigation, 2007. **117**(10): p. 2920-2928.

143. Gong, Y., J. Li, Y. Sun, Z. Fu, C.-H. Liu, L. Evans, K. Tian, N. Saba, T. Fredrick, and P. Morss, *Optimization of an image-guided laser-induced choroidal neovascularization model in mice.* PloS one, 2015. **10**(7): p. e0132643.

144. Castonguay, J., J.H. Orth, T. Müller, F. Sleman, C. Grimm, C. Wahl-Schott, M. Biel, R.T. Mallmann, W. Bildl, and U. Schulte, *The two-pore channel TPC1 is required for efficient protein processing through early and recycling endosomes.* Scientific reports, 2017. **7**(1): p. 1-15.

145. Kilpatrick, B.S., E.R. Eden, L.N. Hockey, E. Yates, C.E. Futter, and S. Patel, *An endosomal NAADP-sensitive two-pore Ca2+ channel regulates ER-endosome membrane contact sites to control growth factor signaling.* Cell reports, 2017. **18**(7): p. 1636-1645.

146. Olsson, A.-K., A. Dimberg, J. Kreuger, and L. Claesson-Welsh, *VEGF receptor signalling? In control of vascular function.* Nature reviews Molecular cell biology, 2006. **7**(5): p. 359-371.

147. Moccia, F., R. Berra-Romani, and F. Tanzi, *Update on vascular endothelial Ca2+ signalling: A tale of ion channels, pumps and transporters.* World journal of biological chemistry, 2012. **3**(7): p. 127.

148. Weischenfeldt, J. and B. Porse, *Bone marrow-derived macrophages (BMM): isolation and applications.* Cold Spring Harbor Protocols, 2008. **2008**(12): p. pdb. prot5080.

149. Martinez, F.O. and S. Gordon, *The M1 and M2 paradigm of macrophage activation: time for reassessment.* F1000prime reports, 2014. **6**.

150. Cui, K., C.L. Ardell, N.P. Podolnikova, and V.P. Yakubenko, *Distinct migratory properties of M1, M2, and resident macrophages are regulated by αDβ2 and αMβ2 integrin-mediated adhesion.* Frontiers in Immunology, 2018. **9**: p. 2650.

151. Vogel, D.Y., P.D. Heijnen, M. Breur, H.E. de Vries, A.T. Tool, S. Amor, and C.D. Dijkstra, *Macrophages migrate in an activation-dependent manner to chemokines involved in neuroinflammation.* Journal of neuroinflammation, 2014. **11**(1): p. 23.

152. Laskin, D.L., V.R. Sunil, C.R. Gardner, and J.D. Laskin, *Macrophages and tissue injury: agents of defense or destruction?* Annual review of pharmacology and toxicology, 2011. **51**: p. 267-288.

153. Wiesner, C., V. Le-Cabec, K. El Azzouzi, I. Maridonneau-Parini, and S. Linder, *Podosomes in space: macrophage migration and matrix degradation in 2D and 3D settings.* Cell adhesion & migration, 2014. **8**(3): p. 179-191.

154. Lämmermann, T., B.L. Bader, S.J. Monkley, T. Worbs, R. Wedlich-Söldner, K. Hirsch, M. Keller, R. Förster, D.R. Critchley, and R. Fässler, *Rapid leukocyte migration by integrin-independent flowing and squeezing.* Nature, 2008. **453**(7191): p. 51-55.

155. Rider, P., Y. Carmi, O. Guttman, A. Braiman, I. Cohen, E. Voronov, M.R. White, C.A. Dinarello, and R.N. Apte, *IL-1α and IL-1β recruit different myeloid cells and promote different stages of sterile inflammation.* The Journal of Immunology, 2011. **187**(9): p. 4835-4843.

156. Fahey, E. and S.L. Doyle, *IL-1 family cytokine regulation of vascular permeability and angiogenesis.* Frontiers in Immunology, 2019. **10**.

157. Eandi, C.M., H.C. Messance, S. Augustin, E. Dominguez, S. Lavalette, V. Forster, S.J. Hu, L. Siquieros, C.M. Craft, and J.-A. Sahel, *Subretinal mononuclear phagocytes induce cone segment loss via IL-1β.* Elife, 2016. **5**: p. e16490.

158. Stevenson, F.T., F. Torrano, R.M. Locksley, and D.H. Lovett, *Interleukin 1: the patterns of translation and intracellular distribution support alternative secretory mechanisms.* Journal of cellular physiology, 1992. **152**(2): p. 223-231.

159. Matsushima, K., M. Taguchi, E. Kovacs, H. Young, and J. Oppenheim, *Intracellular localization of human monocyte associated interleukin 1 (IL 1) activity and release of biologically active IL 1 from monocytes by trypsin and plasmin.* The Journal of Immunology, 1986. **136**(8): p. 2883-2891.

160. Ferrari, D., P. Chiozzi, S. Falzoni, M. Dal Susino, L. Melchiorri, O.R. Baricordi, and F. Di Virgilio, *Extracellular ATP triggers IL-1 beta release by activating the purinergic P2Z receptor of human macrophages.* The Journal of Immunology, 1997. **159**(3): p. 1451-1458.

161. Gudipaty, L., J. Munetz, P.A. Verhoef, and G.R. Dubyak, *Essential role for Ca2+ in regulation of IL-1β secretion by P2X7 nucleotide receptor in monocytes, macrophages,*

and HEK-293 cells. American Journal of Physiology-Cell Physiology, 2003. **285**(2): p. C286-C299.

162. Tseng, H.H.L., C.T. Vong, Y.W. Kwan, S.M.-Y. Lee, and M.P.M. Hoi, *Lysosomal Ca2+ signaling regulates high glucose-mediated interleukin-1β secretion via transcription factor EB in human monocytic cells.* Frontiers in immunology, 2017. **8**: p. 1161.

8 Appendix

8.1 List of primers

Supplementary table 1 primers for qRT-PCR

Primer name	Sequence 5’ – 3’
mTPC2_F	TGCTGCAGAATTCCTCCATGAT
mTPC2_R	ATGGTGAAGAGACACAGGTGG
mIL-1β_F	TGCCACCTTTTGACAGTGATGA
mIL-1β_R	ATCAGGACAGCCCAGGTCAA
mHprt_F	TGCCGAGGATTTGGAAAAAGTG
mHprt_R	TGGCCTCCCATCTCCTTCAT
mCD86_F	CATGGGCTTGGCAATCCTTA
mCD86_R	AAATGGGCACGGCAGATATG
miNOS_F	CCGAAGCAAACATCACATTCA
miNOS_R	GGTCTAAAGGCTCCGGGCT
mIL-12 p40_F	TGGTTTGCCATCGTTTTGCTG
mIL-12 p40_R	ACAGGTGAGGTTCACTGTTTCT
mTNF-α_F	GCCACCACGCTCTTCTGTCT
mTNF-α_R	GGTCTGGGCCATAGAACTGATG
mArg-1_F	CTCCAAGCCAAAGTCCTTAGAG
mArg-1_R	AGGAGCTGTCATTAGGGACATC
mCD206_F	CCACAGCATTGAGGAGTTTG
mCD206_R	ACAGCTCATCATTTGGCTCA
mFizz1_F	TCCCAGTGAATACTGATGAGA

mFizz1_R	CCACTCTGGATCTCCCAAGA
mYM-1_F	GGCTACACTGGAGAAAATAGTCCCC
mYM-1_R	CCAACCCACTCATTACCCTGATAG

8.2 Abbreviations

2D	two-dimensional
3D	three-dimensional
AMD	age-related macular degeneration
APS	ammonium persulfate
Arg-1	arginase1
ATP	adenosine triphosphate
BMDMs	bone marrow-derived macrophages
C2	complement component 2
C3	complement component 3
Ca^{2+}	calcium
$CaCl_2$	calcium chloride
$CaCl_2$	calcium chloride
cADPR	cyclic adenosine diphosphate ribose
CD206	cluster of differentiation 206
cDNA	complementary deoxyribonucleic acid
CFH	complement factor H
CFI	complement factor I
CNV	choroidal neovascularization
CO_2	carbon dioxide
DAMPs	damage- associated molecular patterns
DMEM	dulbecco's modified eagle medium
DMSO	dimethylsulfoxid
DNA	deoxyribonucleic acid
DNase I	deoxyribonuclease I
DPBS	Dulbecco’s phosphate-buffered saline
DTT	dithiothreitol
ECM	extracellular matrix
ECs	endothelial cells

EDTA	ethylenediaminetetraacetic acid
EE	early endosome
EGF	epidermal growth factor
EGTA	ethylene glycol tetraacetic acid
ELISA	enzyme-linked immunosorbent assay
ER	endoplasmic reticulum
FBS	fetal bovine serum
FFA	fundus fluorescein angiography
FGF-B	fibroblast growth factor basic
Fizz1	resistin-like-α
g	gram
g	gravity
GA	geographic atrophy
GWAS	genome-wide association studies
h	hour
H_2O	water
HBSS	Hank's Balanced Salt Solution
Hprt	hypoxanthine guanine phosphoribosyl transferase
IB4	isolectin B4
IFN- γ	interferon-γ
IGF-1	insulin-like growth factor 1
IL-1	interleukin-1
INL	inner nuclear layer
iNOS	inducible nitric oxide synthase
IP_3	inositol 1,4,5-trisphosphate
IPL	inner plexiform layer
l	liter
LE	late endosome
LPS	lipopolysaccharides
LY	lysosome
M	molar
MAC	membrane attack complex
MACS	magnetic cell sorting
MBL	mannose-binding lectin
M-CSF	monocyte-colony stimulating factor
MES	2-(N-morpholino) ethanesulfonic acid

mg	milligram
MHC	histocompatibility complex
min	minute
ml	milliliter
mM	millimolar
mm	millimeter
mRNA	messenger RNA
MSA	methanesulfonate
mV	millivoltage
MVB	multivesicular bodies
mW	milliwatt
MyD88	myeloid differentiation primary response protein 88
Na^+	sodium
NAADP	nicotinic acid adenine dinucleotide phosphate
NaCl	sodium chloride
NaOH	sodium hydroxide
NF-κB	nuclear factor-κB
NLRP3	Nod-like receptor protein 3
NLRs	NOD-like receptors
NO	nitric oxide
ONL	outer nuclear layer
OPL	outer plexiform layer
OS	outer segments
pA	picoampere
PAGE	polyacrylamide gel electrophoresis
PAMPs	pathogen-associated molecular patterns
PB	phosphate buffer
PBS	phosphate-buffered saline
PCR	polymerase chain reaction
PDGFβ	platelet-derived growth factor receptor
PFA	paraformaldehyde
pH	power of hydrogen
$PI(3,5)P_2$	phosphatidylinositol 3,5-bisphosphate
PM	peritoneal macrophages
PVDF	polyvinylidene fluoride
qRT-PCR	quantitative real-time PCR

RE	recycling endosome
RPE	retinal pigment epithelium
SDS	sodium dodecyl sulfate
TBST	tris-buffered saline with Tween20
TEMED	tetramethylethylenediamine
TGN	*tans*-Golgi network
Th	helper T cell
TLR	Toll-like receptors
TNF-α	tumor necrosis factor-α
TPCs	two-pore channels
TRP	transient receptor potential channels
VEGF	vascular endothelial growth factor
WT	wild type
Ym1	chitinase-like 3
µg	microgram
µl	microliter
µM	micromolar
Ω	Ohm

8.3 Publications

Yanfen Li, Christian Schön, Cheng-Chang Chen, Zhuo Yang, Raffael Liegl, Elisa Murenu, Norbert Klugbauer, Christian Wahl-Schott, Stylianos Michalakis, and Martin Biel. "TPC2 promotes choroidal angiogenesis and inflammation in a mouse model of neovascular age-related macular degeneration." (Submitted)

Chen, Cheng-Chang, Einar Krogsaeter, Elisabeth S. Butz, **Yanfen Li**, Rosa Puertollano, Christian Wahl-Schott, Martin Biel, and Christian Grimm. "TRPML2 is an osmo/mechanosensitive cation channel in endolysosomal organelles." Science advances 6, no. 46 (2020): eabb5064.

8.4 Acknowledgements

First of all, I would like to express my sincere regards to my supervisors Prof. Dr. Stylianos Michalakis and Prof. Dr. Martin Biel for giving me the golden opportunity to study in Germany. They gave me constructive suggestions during the planning and development of this project. Prof. Biel encouraged me to be professional and brought my work to a higher level. Prof. Michalakis has taught me the methodology to carry out the research and to present the research works as clearly as possible. Particularly, I also want to thank him for his friendship, empathy, and motivation.

I would like to express my immense gratitude to the China Scholarship Council (CSC) for the financial support during my whole PhD study.

My sincere thanks also go to Dr. Christian Schön for his great contribution to this research work. His professional tutorial and guidance are crucial for the completion of my PhD thesis. I would also like to thank Dr. Chen-Cheng Chang, Dr. Yu-Kai Chao, Dr. Raffael Liegl, and Zhuo Yang for their wonderful collaboration. They supported me greatly and were always willing to help me.

I also want to say thank to all the current and past members of Prof. Michalakis's group: Elisa, Vicky, Marina, Constanze, Johanna, Grazia, Lena, Sabrina, and Jacqueline, for the scientific discussions and for all of the fun we have had together.

I would also like to extend my thanks to all the technicians of the laboratory and other lab colleagues not mentioned above. Their generous assistant and support have been very much appreciated.

Many thanks to my Chinese friends, Fanfan Sun, Miao Jin, Hua Liu, Yujia Li, Yu Pei, Wenhua Ding, and other friends for their emotional support during these years.

Last but not least, I would like to especially express my deepest gratitude to family members: my parents, siblings, and lovely nephew for their unconditional company, support, and encouragement throughout my life.